Ultralow Modulus and High Strength Ti-25Nb (at%) Alloy

A Dissertation Presented to

The Faculty of the School of Engineering and Applied Science

University of Virginia

---

in partial fulfillment

of the requirements for the degree

Doctor of Philosophy

by

Wenhao Lin

May

2023

APPROVAL SHEET

This

Dissertation

is submitted in partial fulfillment of the requirements
for the degree of

Doctor of Philosophy

Author: Wenhao Lin

This Dissertation has been read and approved by the examine committee:

Advisor: Ji Ma

Advisor:

Committee Member: Tao Sun

Committee Member: James M. Howe

Committee Member: Sean R. Agnew

Committee Member: Xiaodong Li

Committee Member:

Committee Member:

Accepted for the School of Engineering and Applied Science:

Jennifer L. West, School of Engineering and Applied Science

May 2023

Table of Contents

List of Figures:

List of Tables:

Acknowledgement

I would like to express my deepest gratitude to all those who have supported me throughout my PhD journey. This has been a truly life-changing journey, deeply reshaping and transforming a teenager coming out of college to an engineer/scientist. There are many people to whom I owe thanks. First and foremost, I would like to thank my Ph.D. advisor, Prof. Ji Ma. I have always considered myself extremely fortunate to be his student. From Texas A&M University to University of Virginia, he has consistently been there to provide me with support, both in academy and in life. Then, I would like to thank my dissertation committee members: Prof. Tao Sun, Prof. James Howe, Prof. Sean Agnew, and Prof. Xiaodong Li. I really appreciate the time, the effect as well as the understanding they generously provide. Next, I would like to thank all the professors who taught/guided me, including Prof. Jerrold Floro, Prof. Giovanni Zangari, Prof. James Howe, Prof. Bicheng Zhou, Prof. Sean Agnew, Prof. James Fitz-Gerald, Prof. Tao Sun, Prof. Richard Martukanitz. I would also like to thank all the staff members in MSE department, including Sherri Sullivan, Tonya Reynolds, Bryana Amador, Jerry Weaver, Tanner Fitzgerald and so many more.

My gratitude also gives to all the NMCF staff members, including Richard White, Helge Heinrich, Diane Dickie, Catherine Dukes, and Joe Thompson. Thank you all for training me and helping me for all the essential analytical/characterization skills to complete my Ph.D. research works. I also need to thank Eric Hogloud for helping/teaching me with the S/TEM skills and knowledge. Thanks to his inspiration, I began incorporating Python into my daily research, which fundamentally changed how I work with data. I thank Dr. Yang Ren for helping me with the in-situ Synchrotron experiment at APS 11-ID-C. I thank Dr. Yong Cai for providing me the opportunity to visit Brookhaven National Laboratory IXS 10-ID. I also need to thank all my fellow researchers in the MSE department. I thank Jonathan Skelton for the countless enjoyable

discussions on a wide variety of subjects. I thank Michael Ritzo and Mark Wischhusen for their kind and generous helps on research and laboratory equipment. I thank Lin Gao for helping me conduct critical experiments during the crucial times. And I need to thank all my fellow graduate researchers in Prof. Ji Ma's research group: Prosenjit Biswas, Connor Headley, Fanyue Kong, Minh Tran, and Rachel McNamara, as well as current and former undergraduate researchers, including Avery Walker, Mrinaal Lorengo, and so many more.

I am deeply grateful to my family, especially my parents, my uncle's family, and my aunt. Thank them for the unwavering support and believe throughout my journey. I thank all the friends I met in Charlottesville. Special thanks to Lin Gao and his wife, for their kindness and warm-heartedness during the pandemic.

Finally, I want to thank National Science Foundation (NSF) for the financial support under the Grant#2104839 (NSF DMR-MMN) as well as Army Research Office under the Grant# W911NF-22-1-0121.

Abstract

A critical challenge in the field of orthopedic implants lies in the fact that implant materials typically have a much higher elastic modulus than human bones. This discrepancy can lead to a complication known as "stress shielding," which causes bone weakening over time. Metastable β titanium (Ti) alloys are regarded as the next generation of biomedical structural materials due to their exceptional biocompatibility, superior strength, and impressive wear resistance. Most importantly, they exhibit lower moduli compared to other metallic biomaterials. The elastic moduli of β and metastable β Ti alloys can be adjusted by altering their β phase stability, either through meticulous alloy designs or microstructural fabrication. However, the challenge remains, as the moduli of recently developed metastable β Ti alloys rarely fall below 50 GPa.

The objective of this dissertation is to provide valuable insights into achieving ultralow modulus in metastable β-Ti alloys for biomedical applications. The Ti-25Nb (at%) alloy, which belongs to a unique group known as β-Ti shape memory alloys, is studied in this dissertation. These shape memory alloys can undergo stress-induced martensitic phase transformation (SIMT) from the high-temperature BCC β (austenite) phase to the low-temperature α'' (martensite) phase within the elastic deformation regime. The apparent modulus during SIMT is can be significantly lower than the moduli of both austenite and martensite phases.

This dissertation consists of two primary sections. Part 1 (Chapter 1) employs a conventional metallurgy approach using thermo-mechanical treatments to develop a desirable microstructure in Ti-25Nb, aiming to achieve an elastic modulus of 30 GPa or lower. This microstructure can initiate SIMT at near-zero external stress at room temperature. Part 2 (Chapters 2 and 3) utilizes a modern additive manufacturing (AM) approach, specifically laser powder bed fusion (LPBF). Since the current literature offers limited understanding, Chapter 2 initially

investigates the AM microstructure of Ti-25Nb. A novel, unknown orthorhombic phase, as well as the O' phase, are discovered in the AM Ti-25Nb samples. In Chapter 3, we propose an innovative approach for LPBF that enables the production of Ti-25Nb samples with a low modulus of approximately 30 GPa, while ensuring high strength. Additionally, our findings suggest that AM Ti-25Nb can undergo SIMT, albeit with a distinct microstructure from the one discussed in Chapter 1.

1. Introduction

1.1. Metastable β Titanium (Ti) Alloys as Biomedical Structural Materials

Metastable β titanium (Ti) alloys have gained popularity as excellent biomedical structural materials due to their remarkable biocompatibility, superior strength, remarkable wear resistance, and excellent biomechanical compatibility [1]. When compared to other commercial biomedical structural metals such as stainless steels and Co-Cr-based alloys, metastable β-Ti alloys have several decisive advantages. Firstly, Ti alloys have one of the highest strength-to-density ratios (specific strength) among commercial structural metals [2]. This lightweight characteristic makes them ideal for use as orthopedic implant materials. Secondly, these alloys cause minimal adverse effects due to their low cytotoxicity and insoluble oxides, which prevent cellular inflammatory reactions in the body [1]. Most notably, metastable β-Ti alloys have one of the lowest elastic moduli among implant alloys, as demonstrated in **Figure 1**. The low elastic modulus is believed to be the critical factor for biomechanical compatibility. Implants are often plagued by issues such as loosening or fracture due to the large modulus mismatch between implant metals and human bones. This phenomenon, known as "stress shielding," occurs when the stiff implant reduces the loads carried by the relatively compliant bones, leading to bone resorption over time. To minimize these complications, materials with low moduli while retaining high strength are preferred. The current generation of metastable β-Ti alloys, such as Ti-Mo-Zr-Fe (TMZF) alloys and Ti-Nb-Ta-Zr (TNZT) alloys, can achieve elastic moduli of 50-70 GPa, much lower than those of Co-Cr-Mo and Ti-6Al-4V [1].

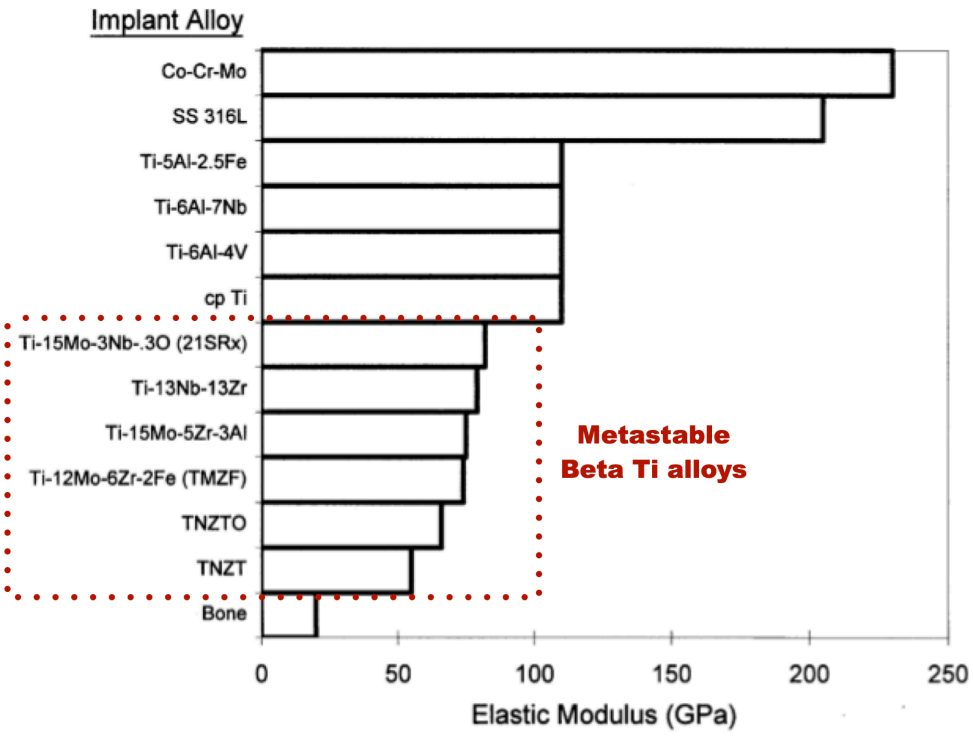

***Figure 1**: Elastic modulus comparison between implant alloys [1].*

Despite recent advancements, the elastic moduli of the current state-of-the-art metastable β-Ti alloys still fall short of matching the value of cortical bones, which is typically below 20 GPa[1]. Additionally, reducing the elastic modulus often results in a simultaneous decrease in the strength [3]. As a result, new techniques are needed to further reduce the modulus without significantly affecting the strength.

1.2. A Brief Introduction of Metastable β-Ti Alloys

Pure titanium has a hexagonal close-packed (HCP) crystal structure, also known as the α phase, at room temperature. However, it transforms to a body-centered cubic (BCC) crystal structure, or the β phase, at 882 ℃ [2]. By adding elements such as niobium (Nb), tantalum (Ta),

molybdenum (Mo), and vanadium (V) to the titanium, the alloys can be maintained as BCC structures at room temperature. These elements are known as β stabilizers. Based on the dominant phase, Ti alloys can be classified as α-Ti, β-Ti, or α/β-Ti alloys [4]. There is a separate class of alloys between the α/β region and the stable β region known as metastable β-Ti alloys, as shown in **Figure 2**.

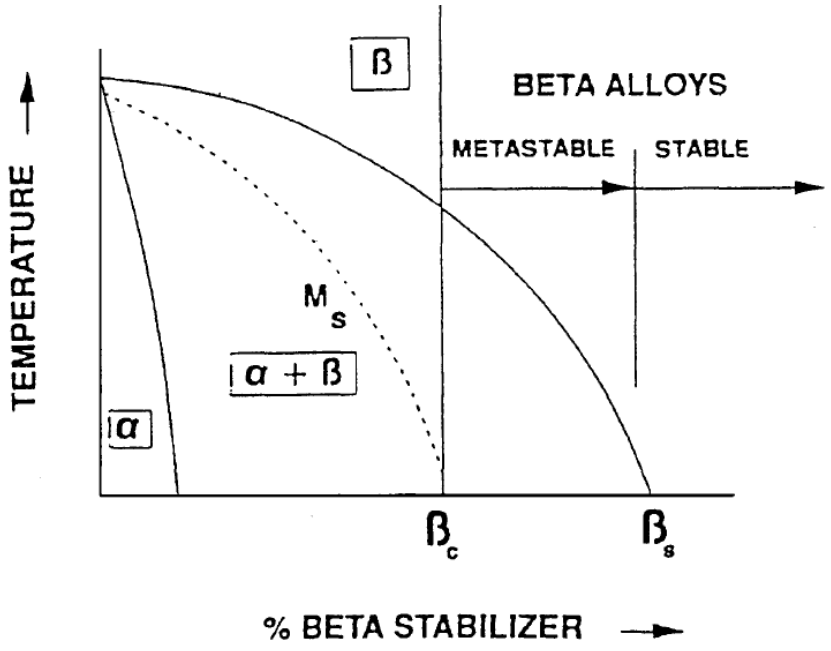

***Figure 2**: A pseudo-binary isomorphous phase diagram of β-Ti alloys[1].*

A β-Ti alloy can have a stable BCC structure at room temperature when it contains an adequate amount of β stabilizers. However, if the content of β stabilizers decreases to a certain level, the theoretical equilibrium temperature T_0 between the α phase and β phase will rise above room temperature [4]. Despite this, due to the sluggish transformation kinetics even at elevated annealing temperatures, these alloys often remain as metastable β structures [5]. This allows several other metastable phases to appear during various thermomechanical treatments. Based on the concentration of β stabilizer elements, the parent BCC structure can transform into either the

HCP α' phase (with less β stabilizers) or the orthorhombic α'' phase (with more β stabilizers) [4,5]. Additionally, a hexagonal phase known as ω can also form from β during quenching or heat treatments below 500°C [6]. The transformation of the β phase to the α' or α'' phase is diffusionless and martensitic. It can be triggered not only by changes in temperature but also by induced stresses [6]. As a result, some metastable β-Ti alloys also show shape memory characteristics. The BCC parent phase is commonly referred to as the austenite phase, while the α' or α'' phase is referred to as the martensite phase. Phases in metastable β-Ti alloys are listed in **Table 1**.

***Table 1**: Phases in metastable β-Ti alloys [4,7].*

Phases	α	β	α'	α''	ω
Crystal Structure	HCP	BCC	HCP	Orthorhombic	Hexagonal
Space Group	P63/mmc	lm$\bar{3}$m	P63/mmc	Cmcm	P6/mmm

1.2.1. Metastable phase – α''

Some β-Ti alloys, such as Ti-Nb, Ti-Mo, Ti-Nb-Zr, and Ti-Nb-Ta, exhibit a shape memory effect similar to that of Ni-Ti SMAs, which are well-known in the aerospace industry[8,9]. The high symmetry cubic parent phase converts to lower symmetry phases, such as monoclinic or orthorhombic, through shearing and lattice shuffling. In the case of β-Ti SMAs, the parent β phase (with a BCC structure) and the α'' orthorhombic martensite phase have a lattice correspondence

as follows, shown in **Figure 3**A). The martensitic transformation from β to α'' can be visualized as the shuffling of $\{0\bar{1}1\}_\beta$ planes along the $< 011 >_\beta$ directions, as indicated in **Figure 3**B).

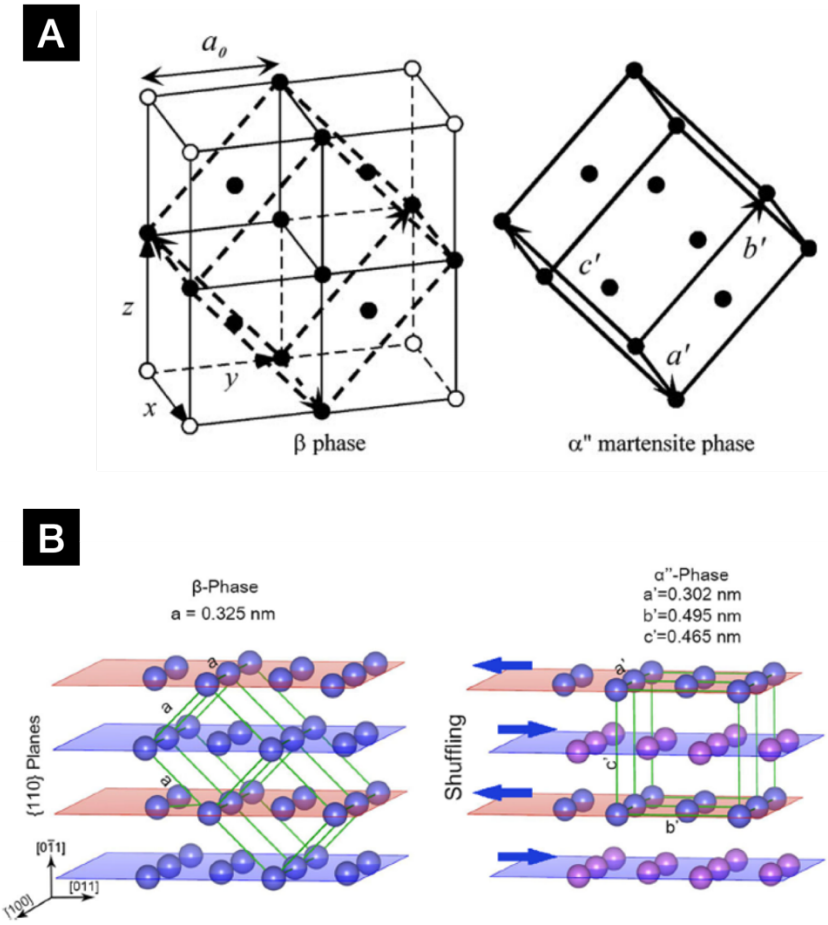

***Figure 3**: A) Lattice correspondence between parent β phase and α'' martensite phase[6]. B) Formation of the orthorhombic martensite phase by shuffling of $\{0\bar{1}1\}_\beta$ planes along $< 011 >_\beta$ [10].*

The lattice correspondence between β and α'' is shown below:

$$[100]_\beta // [100]_{\alpha''}, [010]_\beta // \frac{1}{2}[01\bar{1}]_{\alpha''}, [001]_\beta // \frac{1}{2}[011]_{\alpha''}$$

β stabilizers like Nb not only affect the stability of the β phase at room temperature but also influence the lattice parameters of the resulting martensite phases, as indicated in **Figure 4**.

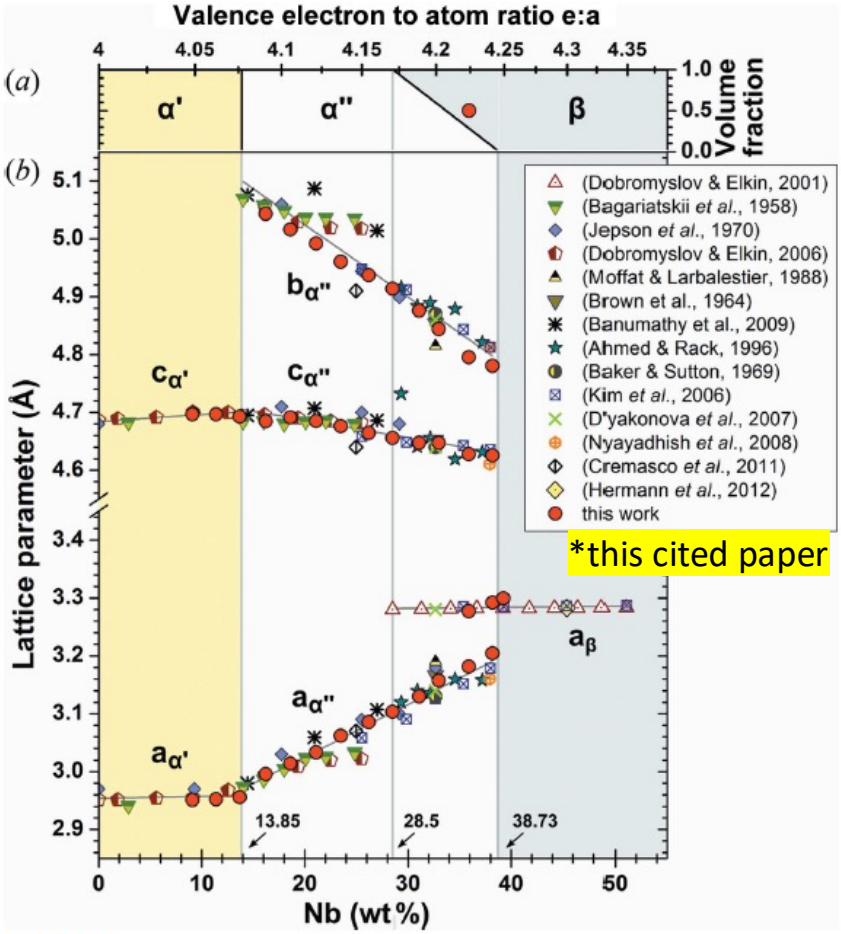

Figure 4*: Summary the lattice parameters of parent β phase as well as martensite phases (α′ and α″) in Ti-Nb alloys[11].*

The formation of the α'' martensite phase is considered self-accommodating, meaning that the overall shape strains required are negligible[12]. This necessitates special coherent interfaces, as well as a transformation path between the parent BCC phase and the orthorhombic martensite phase. According to the continuum theory of crystalline solids, the transformation path from one crystal structure to another needs to meet the requirement of kinematic compatibility [13]. Simply speaking, there must exist an "invariant plane", or a coherent interface, so that the solid remains intact, "not broken", after martensitic phase transformation. This is known as the invariant plane

strain theory, which can be mathematically derived. For martensitic phase transformation from cubic system to orthorhombic system, there exists a total of 6 variants listed in the **Table 2** below:

***Table 2**: Six lattice correspondence variants derived from the invariant plane strain theory[12].*

Variant	$[100]_{\alpha''}$	$[010]_{\alpha''}$	$[001]_{\alpha''}$
V1	$[100]_{\beta}$	$[011]_{\beta}$	$[0\bar{1}1]_{\beta}$
V2	$[100]_{\beta}$	$[0\bar{1}1]_{\beta}$	$[0\bar{1}\bar{1}]_{\beta}$
V3	$[010]_{\beta}$	$[101]_{\beta}$	$[10\bar{1}]_{\beta}$
V4	$[010]_{\beta}$	$[10\bar{1}]_{\beta}$	$[\bar{1}0\bar{1}]_{\beta}$
V5	$[001]_{\beta}$	$[110]_{\beta}$	$[\bar{1}10]_{\beta}$
V6	$[001]_{\beta}$	$[\bar{1}10]_{\beta}$	$[\bar{1}\bar{1}0]_{\beta}$

The martensite phase in β-Ti alloys can be observed on the sample surface by optical microscopy due to its distinctive needle shapes and unique triangular morphology (consisting of

three martensite variants) or V-shaped morphology (consisting of two martensite variants) [12].

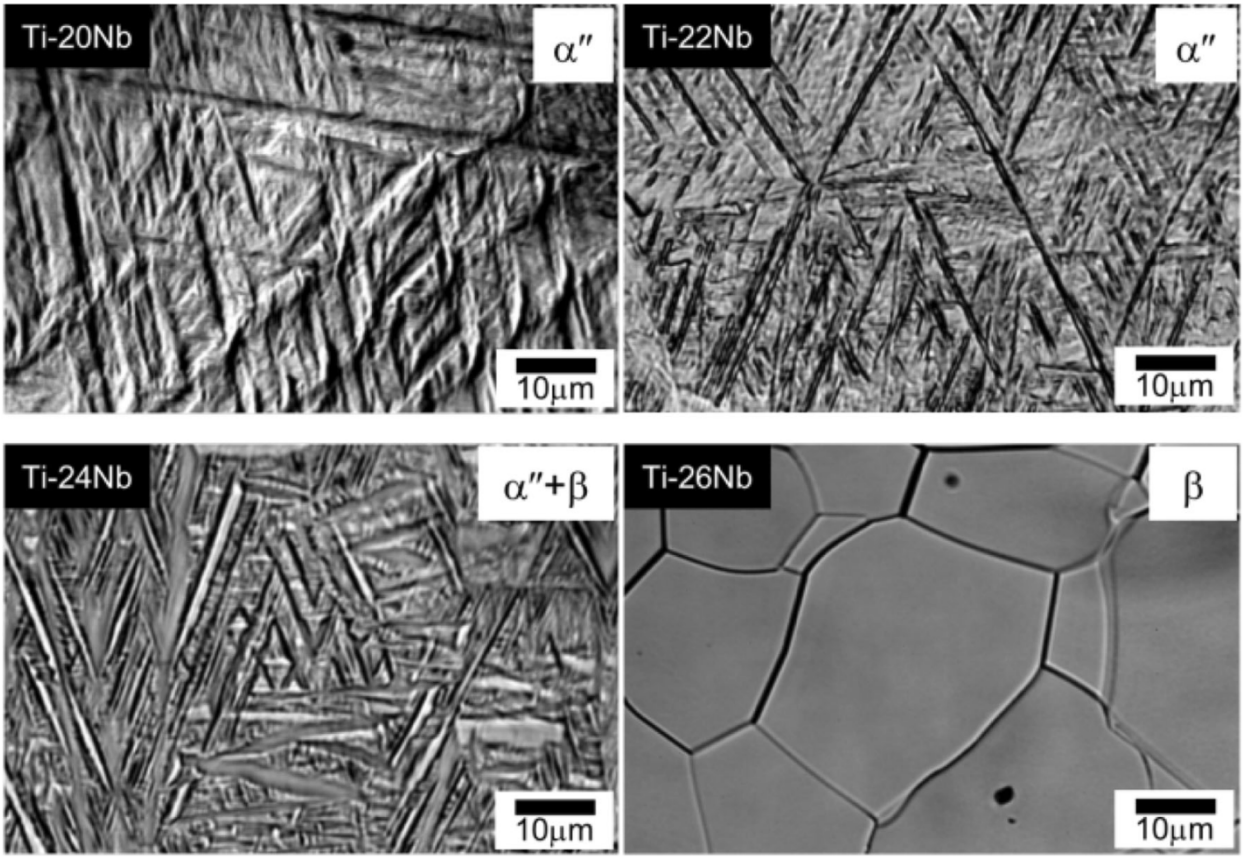

***Figure 5**: The microstructure of martensite in Ti-Nb alloys[9].*

The α'' metastable phase has a significant impact on the mechanical properties of metastable β titanium alloys. For instance, the austenite phase can potentially undergo a stress-induced martensitic phase transformation to the martensite phase when external stress exceeds the transformation stress [8]. This is evident in the stress-strain response, where the curve seems to reach a plateau as the transformation begins, as shown in **Figure 6**. During the stress-induced martensitic phase transformation, the apparent modulus can be considerably lower than the elastic modulus of austenite [8,9]. Theoretically, when the austenite fully converts to martensite and the current stress remains below the yield stress, the stress-strain response will return to normal elastic

deformation, and the apparent modulus will be equal to the elastic modulus of the martensite phase. Since this transformation is somewhat reversible, it extends the elastic deformation range from 0.2% (a typical value) to several percent or even higher. As a result, this behavior is also known as superelasticity [8].

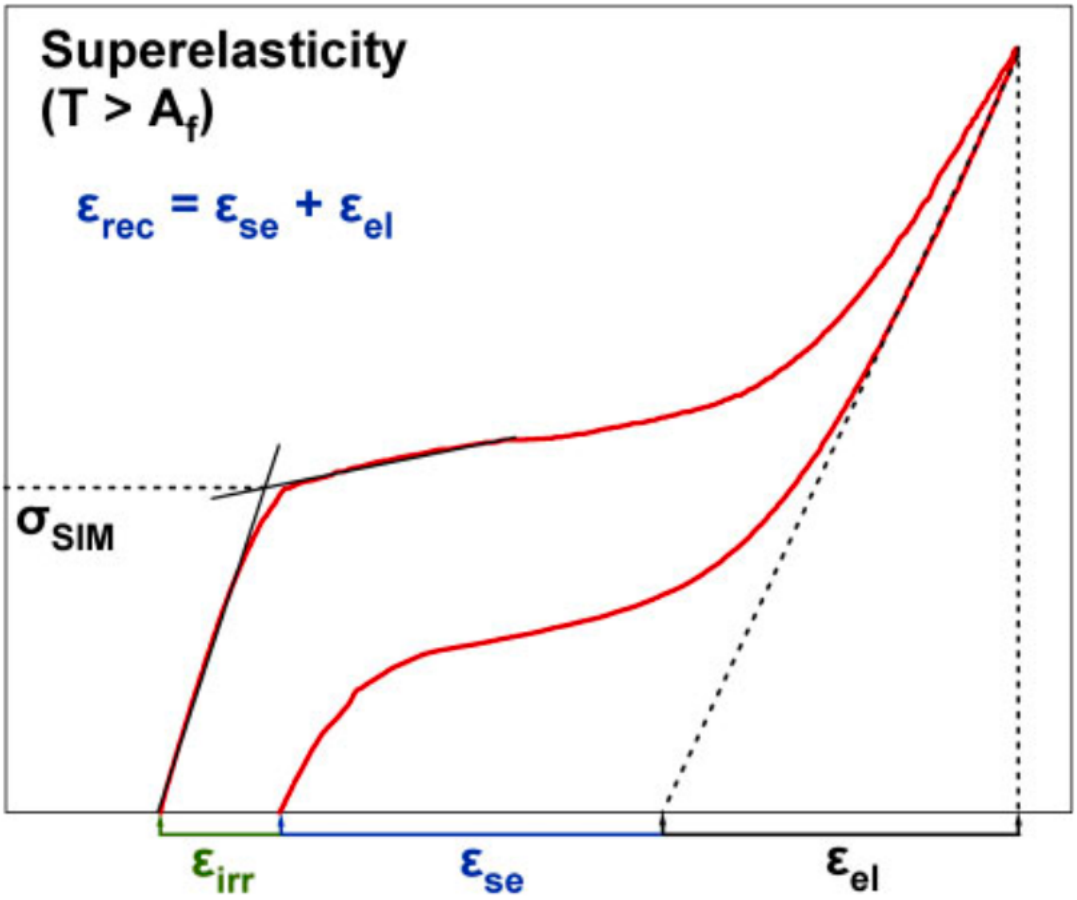

***Figure 6**: A typical stress-induced martensitic phase transformation from high-temperature austenite phase to the low-temperature martensite phase. ε_{rec} = recoverable strain; ε_{se} = superelastic strain; ε_{el} = elastic strain; ε_{irr} = irrecoverable strain; σ_{SIM} = stress-induced martensitic transformation stress [8].*

Several factors can influence the initiation conditions of the stress-induced martensitic transformation. The composition of alloying elements, particularly β stabilizers, is critical in determining the stability of the β phase [4], and in conjunction with temperature, sets the initial

stress required to activate the transformation (known as transformation stress). Increasing the Nb content, for example, raises the required transformation stress [6,14]. In addition, the presence of second phases and defects can significantly impact the transformation stress. For example, ω precipitates can increase the stress level and suppress the martensitic transformation [6], while dislocations can stabilize the transformation while simultaneously suppressing the martensitic transformation [9].

1.2.2. Metastable phase – ω

ω is another metastable phase that appears in β-Ti alloys. There are two types of ω phases: athermal ω and thermal ω. Athermal ω is formed through quenching from elevated temperatures, while thermal ω is formed through low or intermediate temperature aging (below 500°C) [15,16]. The formation of the ω phase can be attributed to the collapse of $\{111\}_\beta$ planes of the parent BCC phase, which is depicted in **Figure 7**.

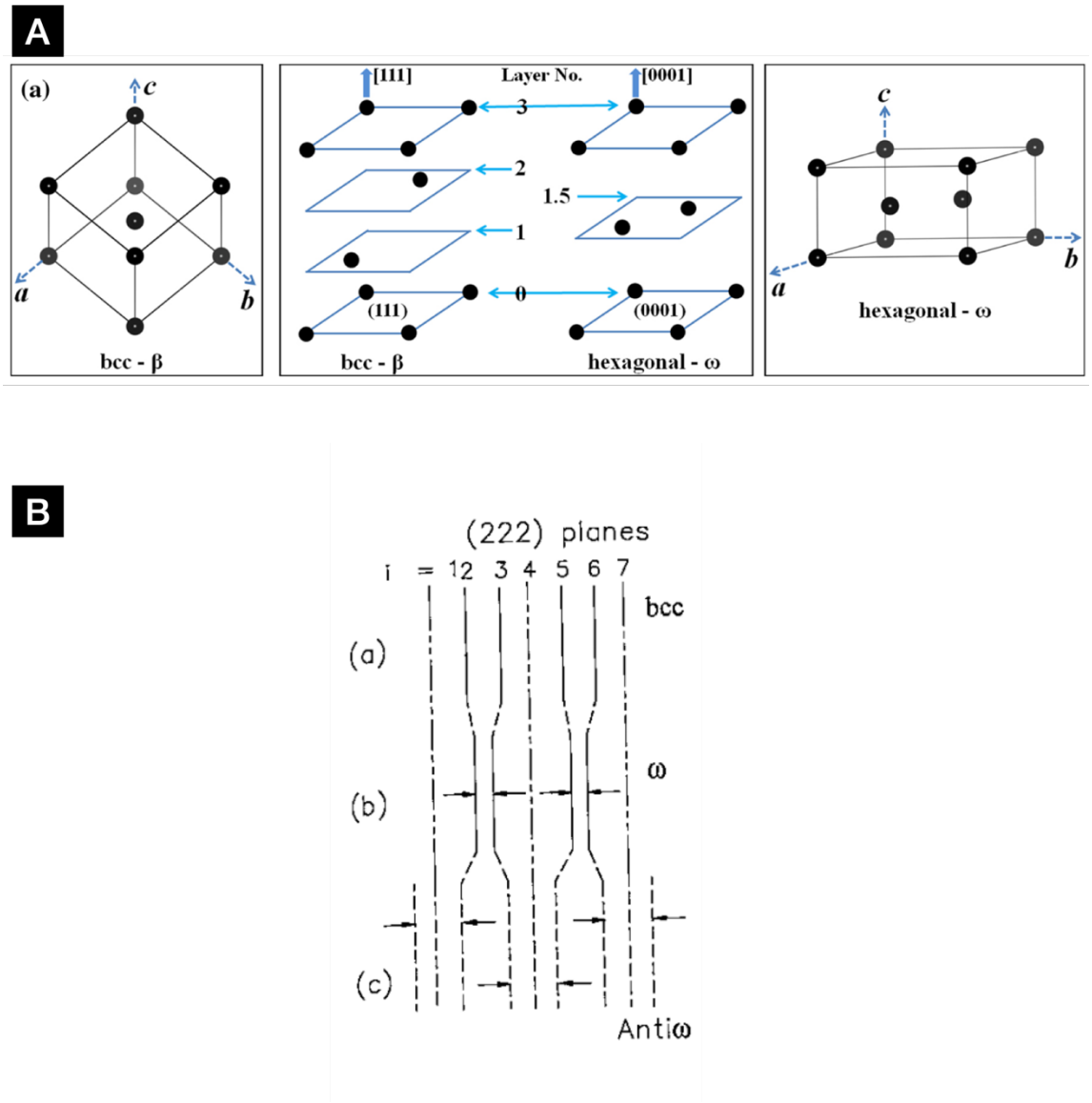

***Figure** 7: Schematics of formation of ω via collapse of* $\{111\}_\beta$ *planes [15,16].*

The presence of ω particles in β-Ti alloys is often associated with deleterious effects on mechanical properties. For instance, despite an increase in strength and hardness, low-temperature aging can lead to a significant loss of ductility [6], because of the nucleation and growth of the thermal ω phase in the β phase. However, the effect of the ω phase on mechanical properties is more complex than this. In β-Ti alloys, the ω phase is highly relevant to the shape memory effect [6]. Kim et al. demonstrated the influence of the ω content on mechanical properties and the shape

memory effect [17]. For instance, the Ti-26Nb (at%) specimen that was as-annealed exhibited complete superelasticity at 1.5% strain, but the superelastic behavior diminished as the strain increased in sequential cycles, as shown in **Figure 8** A). Aging at an elevated temperature like 300℃ led to the precipitation of the thermal ω phase. Interestingly, moderate amounts of ω can stabilize superelasticity, as demonstrated in **Figure 8** B) and C), without severely compromising ductility. However, at higher concentrations of the ω phase, as shown in **Figure 8** D) after 10 hours of aging at 300℃, the material becomes extremely brittle, with no observed superelasticity. Additionally, some researchers suggest that the ω phase plays a significant role in the strain development of β-Ti alloys [18,19]. For example, a thin layer of the ω phase can form during reverse martensitic transformation after mechanical loading and unloading [20].

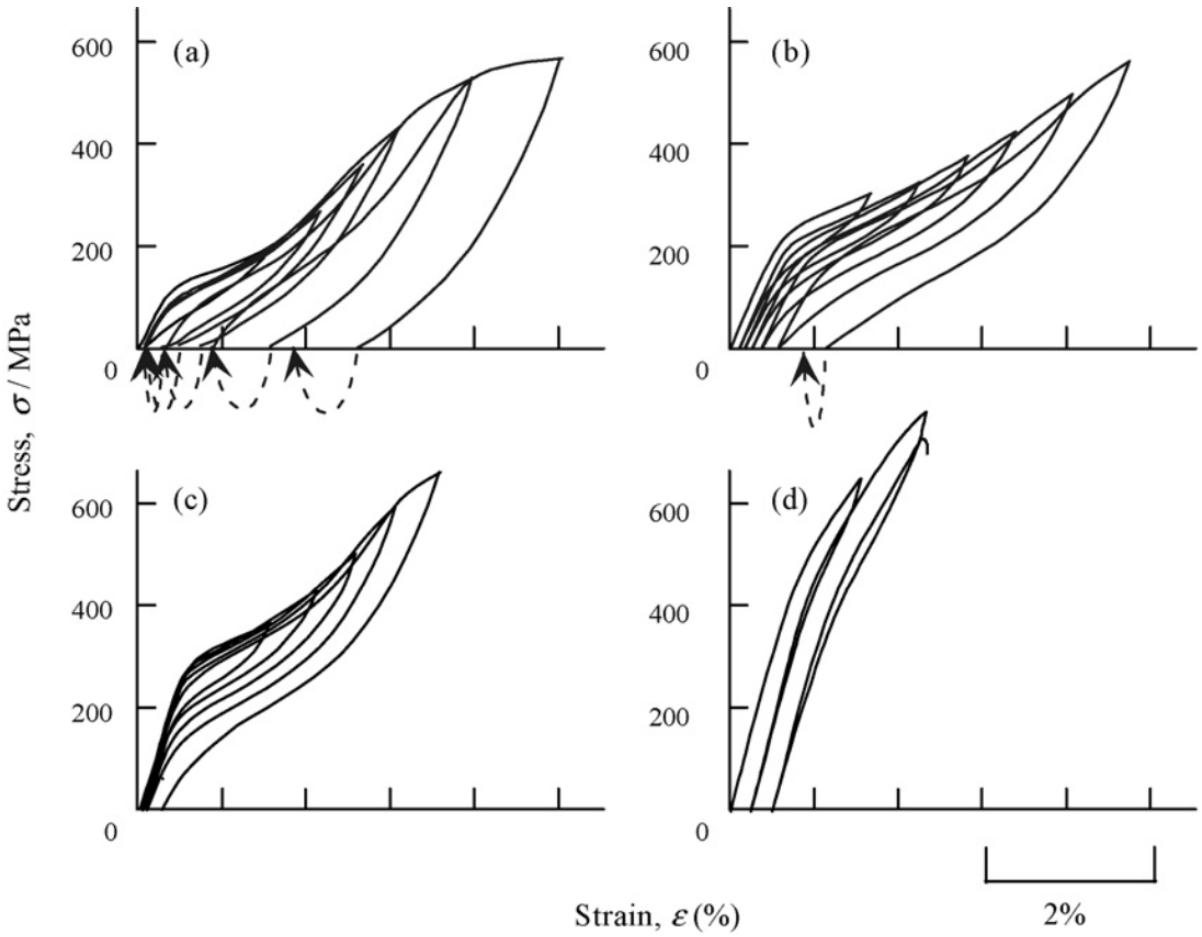

Figure 8*: Examples of ω phase effect on the mechanical performance of Ti-26Nb (at%) β. alloys. (a) the specimens annealed at 600* ℃ *for 10 minutes. Then the specimens were continued aged at 300* ℃ *for (b) 30 minutes, (c) 1 hour and (2) 10 hours [17]. Note: the specimens were received additional heating to around 225*℃ *after each loading-unloading cycle to check shape memory effect recovery.*

The morphology of the thermal ω phase displays ellipsoidal particles embedded in β grains, with their major axes aligned with $< 111 >_{\beta}$ [16], displayed in **Figure 9** A). The athermal ω phase, however, is often hard to detect due to the much smaller particle size, which is typically only a few nanometers. Using selected area electron diffraction (SAED) in transmission electron microscopy (TEM), it is possible to detect diffuse intensity in the diffraction patterns and phonon

softening in the parent β phase [16]. Specifically, these intensities appear at 1/3 and 2/3 of the wave vectors of the BCC lattice, shown in **Figure 9** B). With state-of-art electron microscopy, the ω phase can be imaged at the atomic level, shown in **Figure 10**. Devaraj et al demonstrated the ω-like embryos at distinctly different stages of collapse of the $\{111\}_\beta$ planes using high-angle annular dark-field high-resolution scanning transmission electron microscopy (HAADF-HRSTEM) [21].

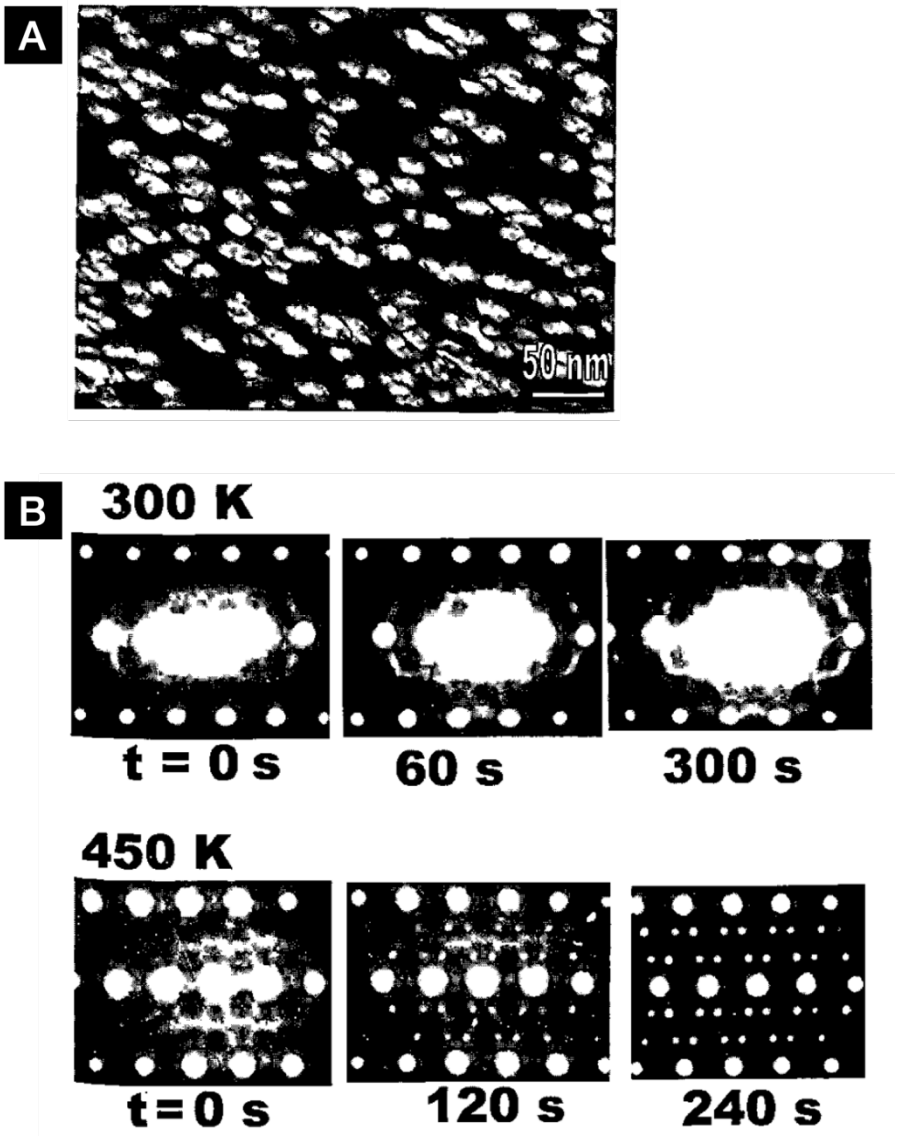

***Figure 9**: A) Dark-field TEM image of ω phase. B) SAED patterns of ω phase at $< 311 >_\beta$ zone axis at various thermal condition [16].*

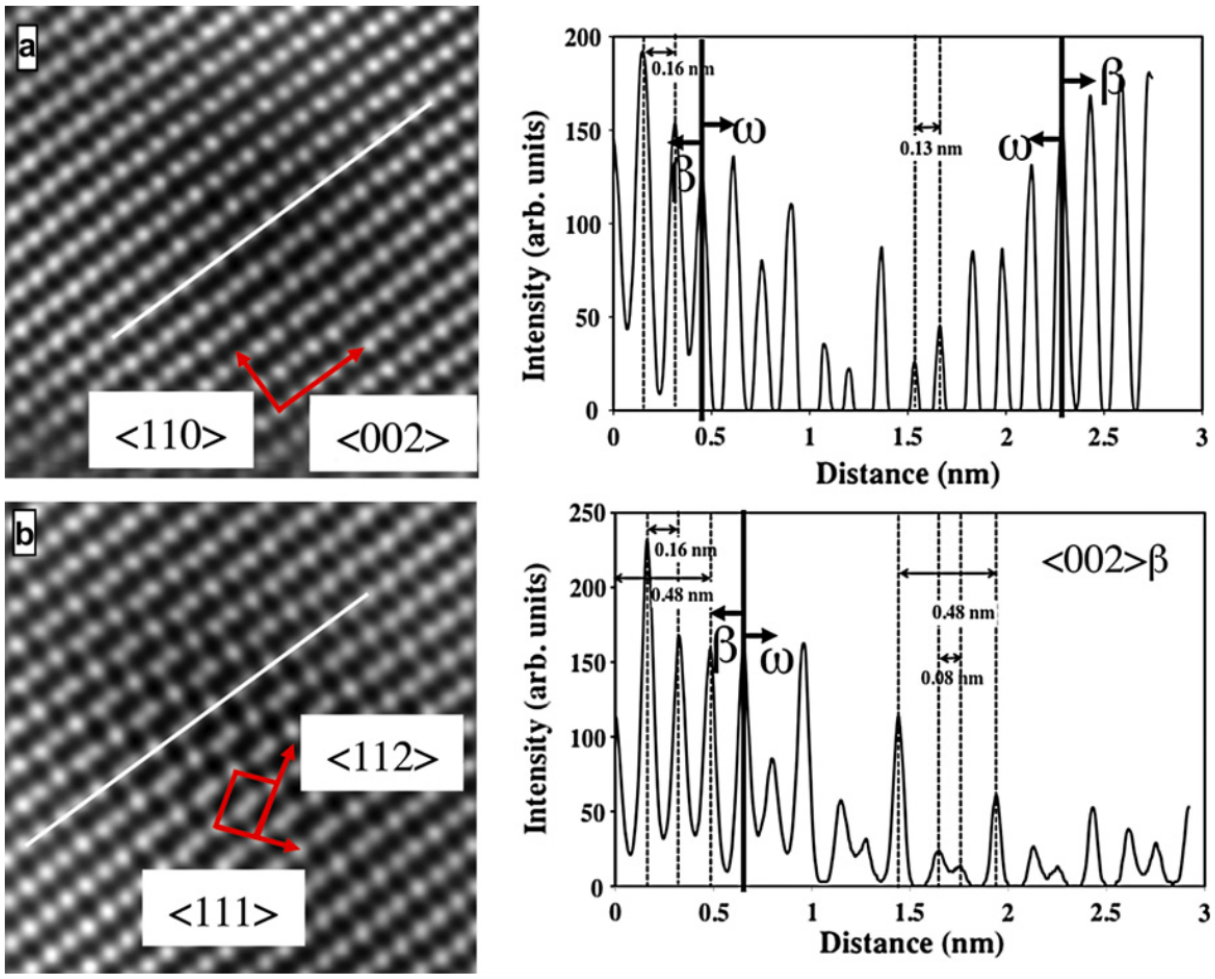

***Figure 10**: Example of HAADF-HRSTEM images of ω-like embryos in β matrix in Ti-9Mo [21].*

1.2.3. Metastable phase – O'

Researchers have recently discovered a new intermediate phase, known as the O' phase, between the β and α'' martensite phases. This phase is often present when a small amount of interstitial atoms such as oxygen is added to β-Ti alloys[9,22,23]. Oxygen atoms can occupy the octahedral sites in the BCC lattice, causing a slight distortion to the parent β phase. These locally distorted regions around the oxygen atoms are called nano-domains or O' phase. Due to the increased strain energy of the lattice, the O' phase can facilitate the lattice shuffling and martensitic transformation to α'' phase, making it a precursor to the latter [9]. In fact, there are a total of 6

variants of the O' phase, similar to the α'' phase[22]. The occupied octahedral position of the surrounding oxygen atoms can affect the formation of the α" phase by either promoting or suppressing it [9]. **Figure 11** illustrates the relationship between the occupied octahedral sites and the lattice shuffling modes.

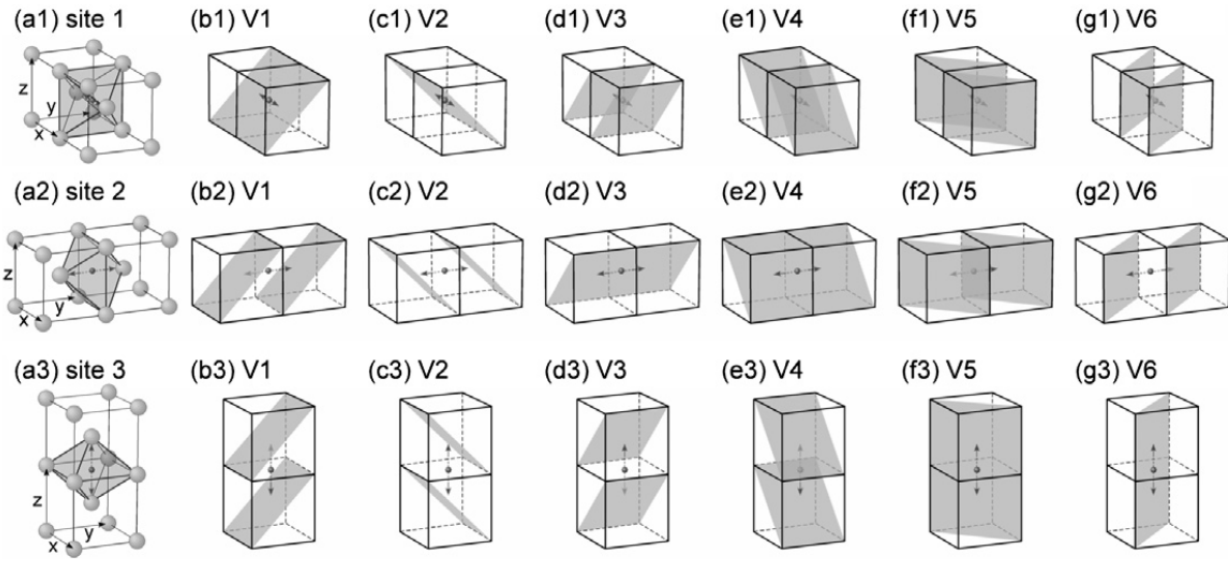

Figure 11*: Schematics of the relationship between occupied octahedral sites and shuffling modes[23].*

In a well-annealed sample with no internal strain, the six variants of the O' phase should be evenly distributed. However, under an external stress field, certain variants can preferentially grow to offset the increased strain energy in the lattice [9]. Kim et al. observed that after cold rolling, the variant that is more aligned with the rolling direction exhibited a higher diffraction intensity in the SAED patterns [22].

Due to the small size of the O' phase, there are only a few methods available for detecting its existence, one of which is SAED using TEM. **Figure 12** displays several expected diffraction patterns of the O' phase. In each of the patterns shown, the primary diffraction spots correspond to the β phase, while the diffuse streaks correspond to the intensity of both the O' and ω phases. The

characteristics of the O' phase include a slightly higher intensity at 1/2 of the vectors between major diffraction spots in the pattern, while the ω phase has intensity at 1/3 and 2/3 positions. Occasionally, as in cold-rolled conditions, the intensity of the O' phase's diffraction spots can be more concentrated and visible in SAED.

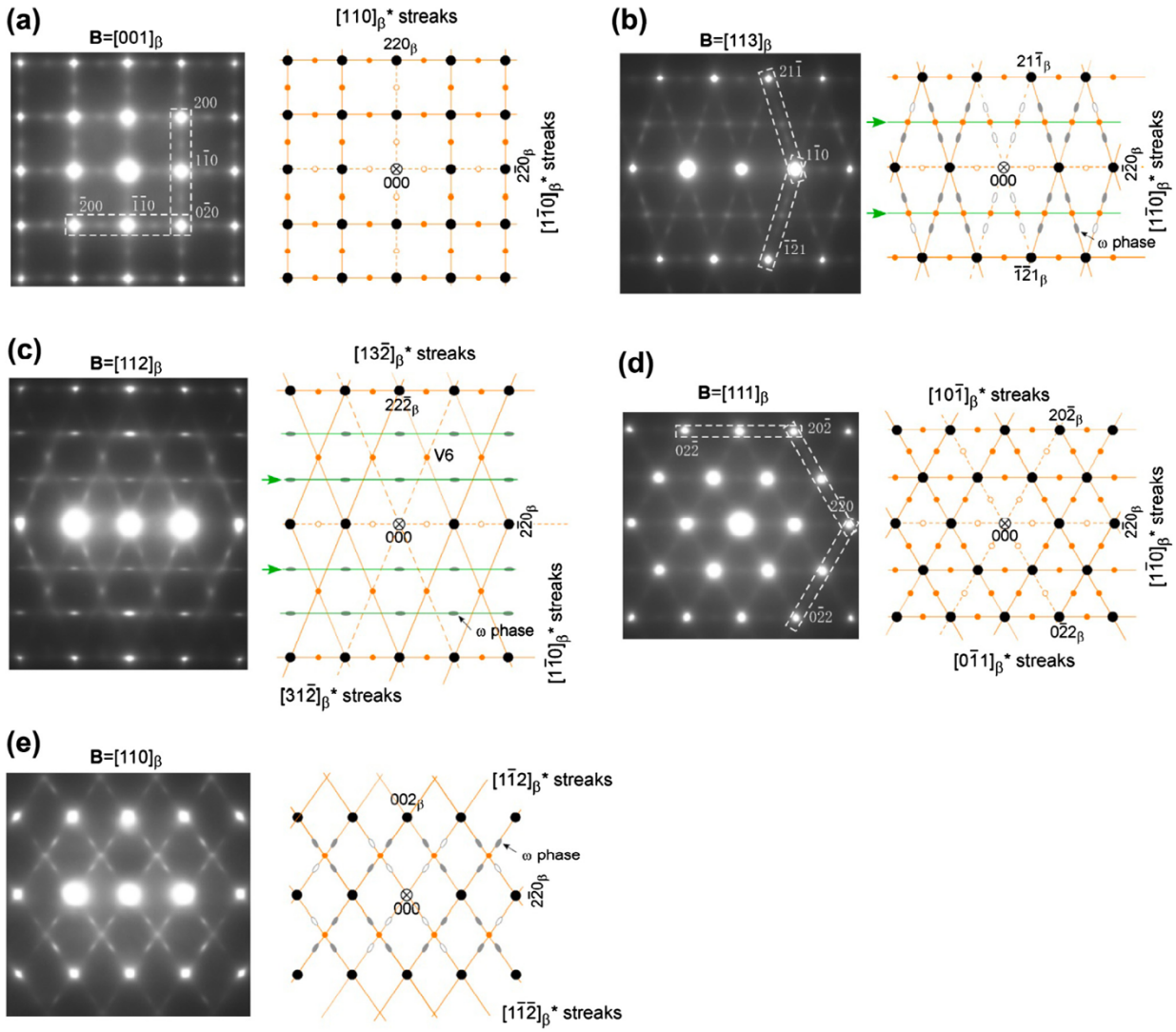

***Figure 12**: Examples of diffraction spots of O' phase at various of zone axes of parent BCC phase[22].*

1.3. Additive Manufacturing (AM) for Orthopedic Implants

Additive Manufacturing (AM) has revolutionized the fabrication of customized and complex parts with a range of alloys [24]. Commercially available techniques such as Laser Direct

Energy Deposition (L-DED) and Laser Powder Bed Fusion (L-PBF) are widely used. AM technologies enable the production of biomedical implants with intricate 3D geometries and provide the ability to tailor specific material properties by controlling microstructure in AM metals. The fabrication methods of AM could allow implants to be tailored to each patient, optimizing geometries and microstructures to maximize healing while minimizing complications [25]. These implants provide structural reinforcement for treating skeletal defects resulting from trauma, infection, or skeletal abnormalities [26,27]. Implants should display optimal biocompatibility, biomechanical compatibility, surface characteristics, and permeability where AM can exhibit greater advantages over traditional manufacturing designs[25,28]. Furthermore, AM unlocks unique possibilities for manipulating material properties. Laser AM methods produce extremely high heating/cooling rates during solidification. By adjusting laser parameters, temperature gradients and cooling rates can be manipulated to alter resultant microstructures [24,29]. What's more, rapid solidification creates hierarchical microstructures that can significantly enhance material performance, as reported with additive manufactured stainless steel 316L, which demonstrated increased strength and ductility simultaneously [24,29–32]. Consequently, AM has the potential to reveal novel properties in metals like metastable β-Ti alloys, given their metastable nature. However, there is a dearth of research on AM β-Ti or metastable β-Ti alloys, especially regarding their microstructures and mechanical performance under AM.

1.3.1. Laser Powder Bed Fusion (LPBF)

Laser powder bed fusion (LPBF), also known as selective laser melting (SLM), utilizes a rapidly scanning laser to selectively melt a two-dimensional pattern in a thin layer of pre-deposited metallic powder[24,29,33,34], demonstrated in **Figure 13**. This process is operated in a processing

chamber, which is a tightly controlled environment, and a selected shielding gas (such as Nitrogen or Argon) is maintained at a high purity. The platform then lowers to distribute a new layer of metallic powder, and the laser melting process is repeated. In this way, the 3D components are constructed layer by layer. LPBF is considered a net shape process because minimal post-processing effort is required for the final geometry. The scan pattern and scan strategy are pre-designed by specialized computer-aided design (CAD) software. Similar to plastic 3D printing, the software arranges the scan path (or scan vectors) and also determines the parameters of the heat source, such as power and scanning speed.

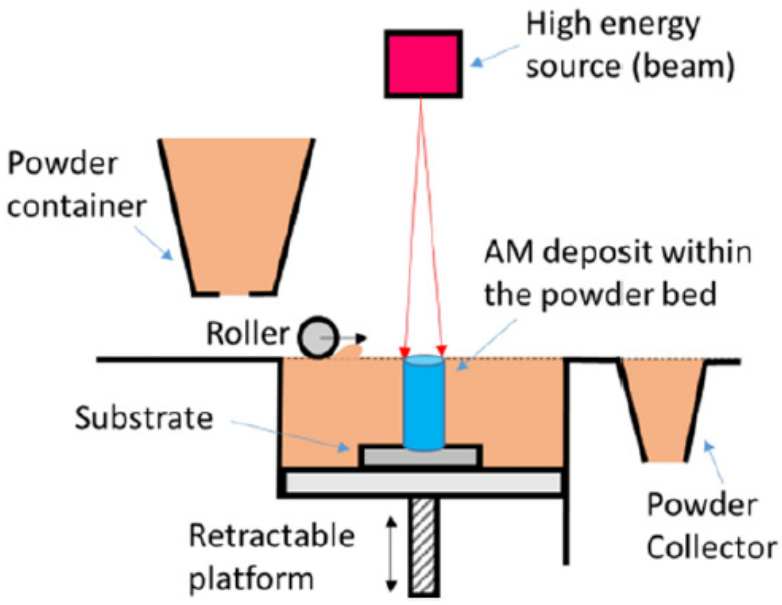

***Figure 13**: Schematics of the main components of a laser powder bed fusion (LPBF) system[35].*

At present, an ytterbium-doped fiber laser system with a wavelength of 1070 nm is the most popular energy source for LPBF. The laser wavelength is a critical factor as it is closely related to the absorption rate of laser energy in various metals, as shown in **Figure 14**. With such ytterbium-doped fiber laser system, elements like silicon, carbon, and iron can absorb a large portion of laser energy (above 50%), making them easier to process, while other elements such as

copper and aluminum are more difficult to process due to their low absorption ratios (below 10%) [36]. However, the reflected laser by metallic powder can be further absorbed by sequential laser absorption due to inner-reflection within the powder bed, demonstrated in **Figure 15**. For that reason, factors such as particle geometry as well as particle size distribution can affect overall laser energy absorption. As a consequence, the printability of certain metals is governed by multiple factors including laser source, material feedstock as well as scanning strategies.

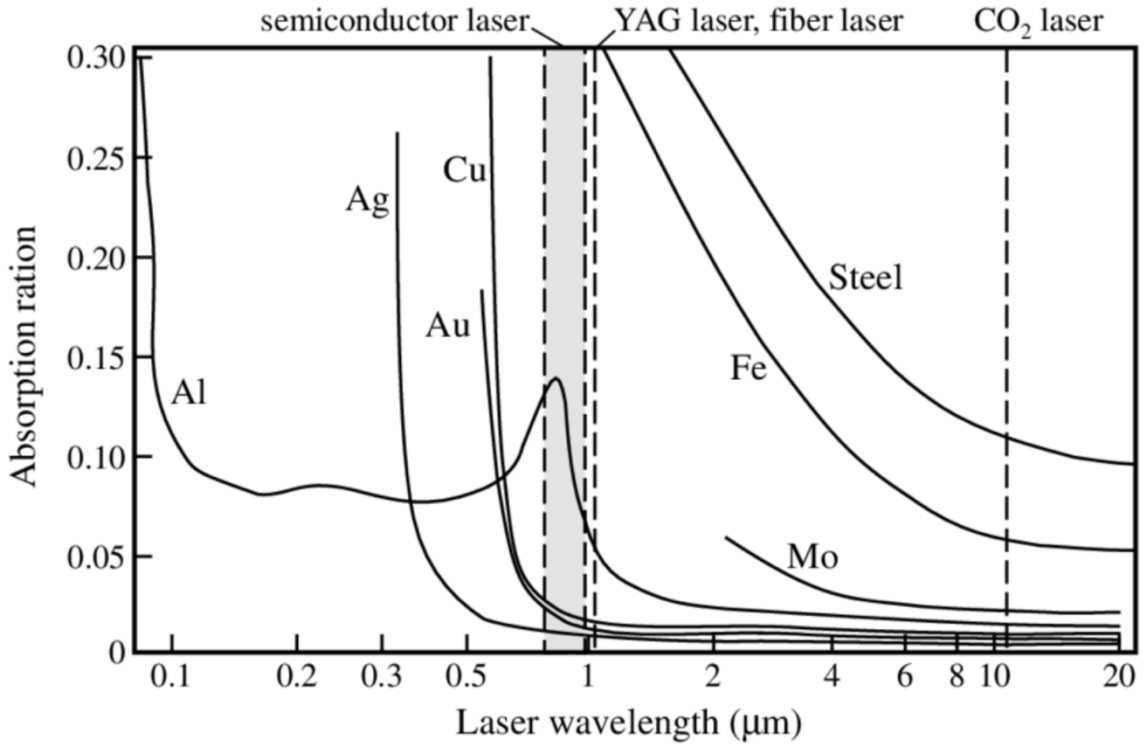

***Figure 14**: Energy absorption of laser in metals is wavelength dependent [36].*

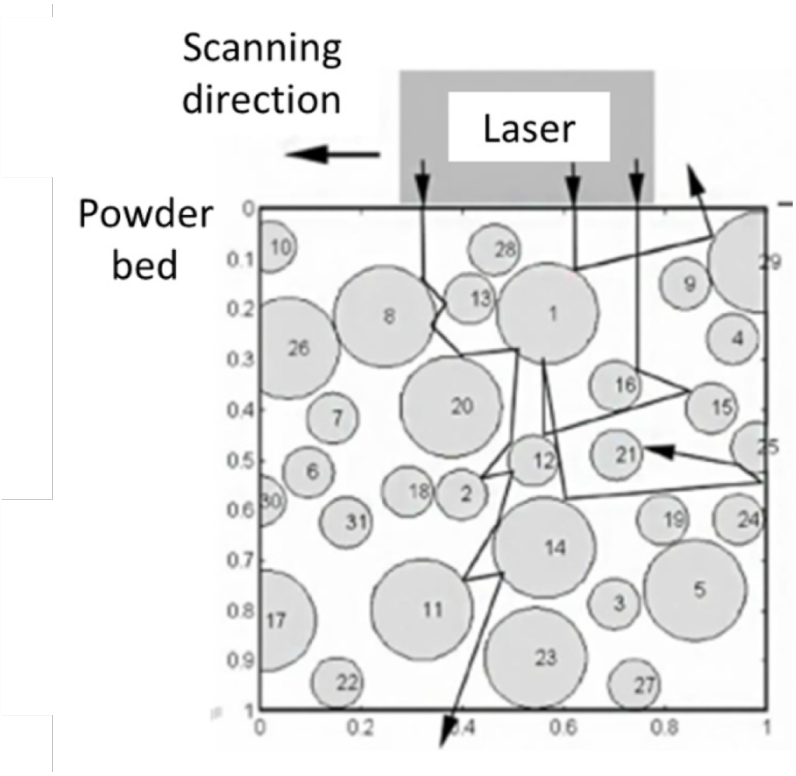

***Figure 15**: Inner-reflection of laser beam within the powder bed [24].*

1.3.2. Rapid solidification

Several mechanisms are involved in the energy transport during additive manufacturing [24]: 1) absorption of energy by the powder and the substrate from the laser; 2) conduction of heat from the liquid pool to the substrate; 3) surface heat losses due to conduction, convection, and radiation; and 4) material evaporation.

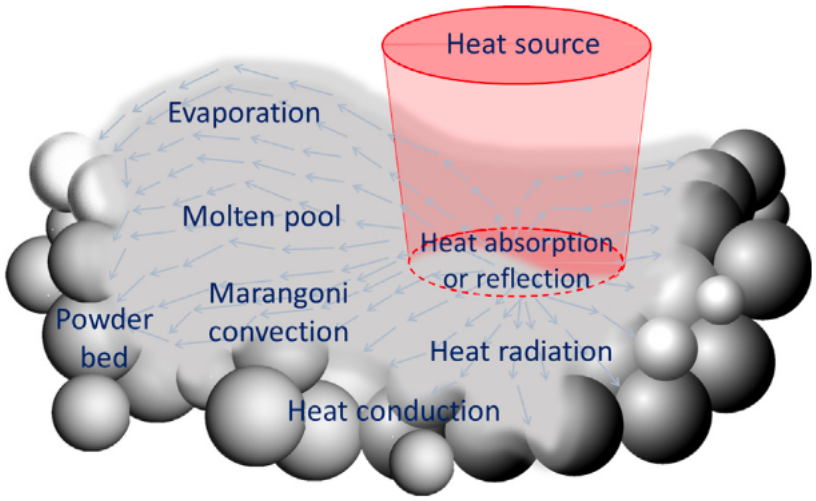

***Figure 16**: Energy transfer in additive manufacturing [24].*

Due to the application of an extremely high-density energy source to a small region, both DED and LPBF can melt solid metals within a fraction of a second. Additionally, the heat generated can be rapidly dissipated. According to published sources [24,33–35], the estimated cooling rate is several $10^3\ Ks^{-1}$ for DED and 10^3 - $10^4\ Ks^{-1}$ for LPBF. These extreme heating and cooling capabilities exceed those of any conventional metallurgical processing methods.

The extreme rapid solidification in AM results in a unique solidification phenomenon [29]. The powder/substrate materials are initially melted by laser heating, creating a region of molten material known as the melt pool. Solidification begins with heterogeneous nucleation at the liquid-solid interface of the melt pool boundary. Initially, the growth direction of the grains is strongly influenced by the epitaxy of the crystallographic orientation of the underlying grains at the boundary of the melt pool. For cubic systems, the <100> directions are typically favored for growth. However, the further growth of the grains is determined by both the maximum thermal gradient and the competitive growth of adjacent grains. Generally, grains that align their favored orientation for growth with the maximum thermal gradient will outgrow their neighboring grains.

Furthermore, based on thermodynamics and the lever rule, the equilibrium concentration of solute at the liquid-solid interface is bounded by two composition values derived from the liquidus line and solidus line at a given temperature, as displayed in **Figure 17**. As can be seen, the redistribution of a solute element occurs as the solidification front advances. The partition coefficient k is used to describe how a particular solute is redistributed [37]. When $k > 1$, the solid absorbs solute from the liquid, whereas when $k < 1$, the solid rejects solute into the liquid.

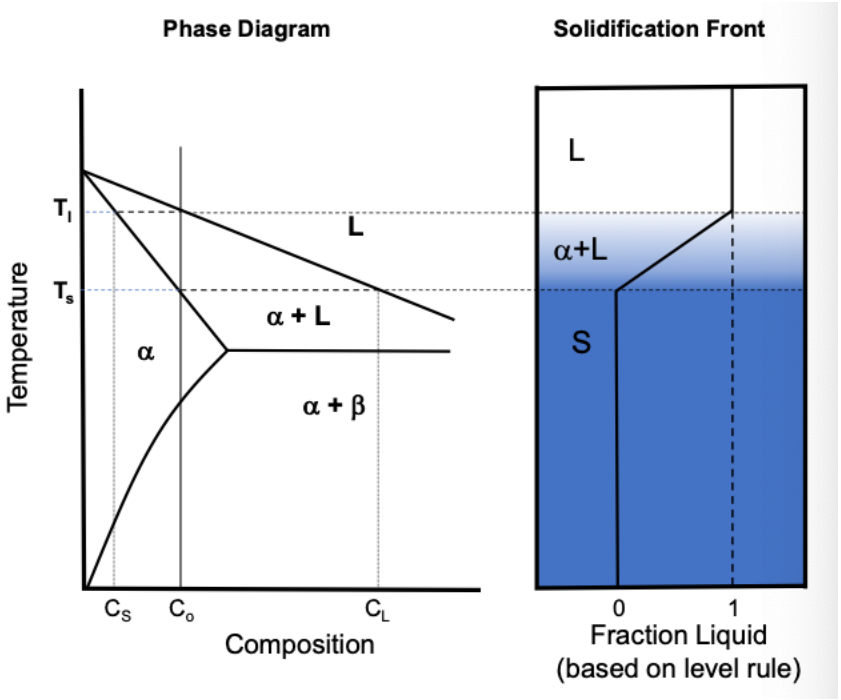

***Figure 17**: Equilibrium composition at the liquid-solid interface [37].*

However, as the cooling rate reaches such an extreme degree in AM, the growth of the liquid-solid front during rapid solidification is far from equilibrium. The redistribution of solutes and their enrichment at the interface may influence the stability of the liquid-solid interface. This phenomenon is known as constitutional undercooling, where the liquidus temperature of the partial solid-liquid interface is higher than the temperature of the melt pool [37]. This further promotes the protrusions on the liquid-solidification interface, and increased instability can enable faster

growth of these protrusions. Such instability can lead to different solidification morphologies in rapid solidification, as shown in **Figure 18** below.

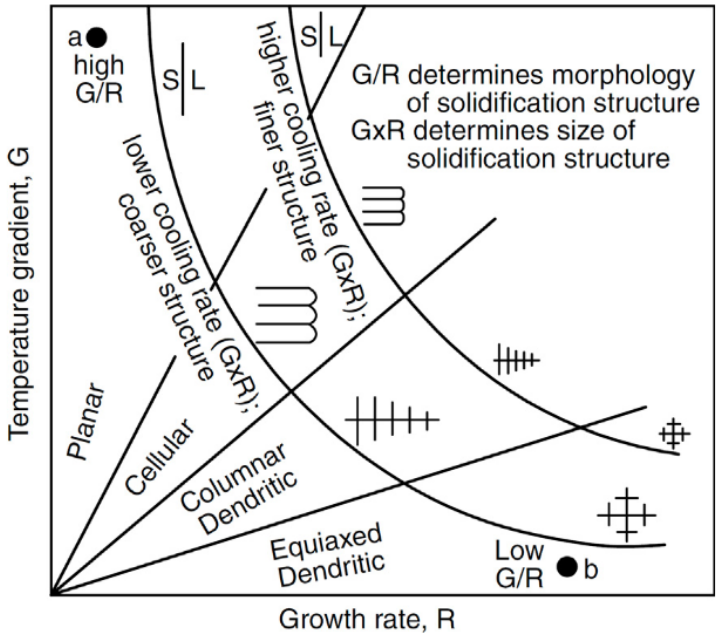

***Figure 18**: Effect of thermal gradient G and growth rate R on the solidification morphology.*

1.3.3. Melt pools and AM solidification features

Simply put, the local temperature gradient (G) and the growth rate (R) of the liquid-solid interface determine the solidification structures that form, as shown in **Figure 18**. A high G/R ratio can result in planar structures, while a low G/R ratio can lead to equiaxed dendritic structures. Both G and R are influenced by various factors related to energy transfer, thermodynamics, and kinetics. In practice, adjusting the laser powder, scanning speed, and scanning path can significantly affect G and R. For instance, the laser scanning speed can modify the degree of constitutional undercooling, which is correlated with the growth rate of the liquid-solid interface. A faster scanning speed leads to a higher degree of constitutional undercooling and consequently, a higher growth rate R. Similarly, the spacing between two laser paths can affect the temperature

field of the melt pool. A closer hatch distance reduces the thermal gradient G. These solidification features are visible in either optical microscopy or secondary electron microscopy after proper chemical etching due to the differences in etching rates resulting from elemental partitioning during solidification. An example of this is shown in **Figure 19**.

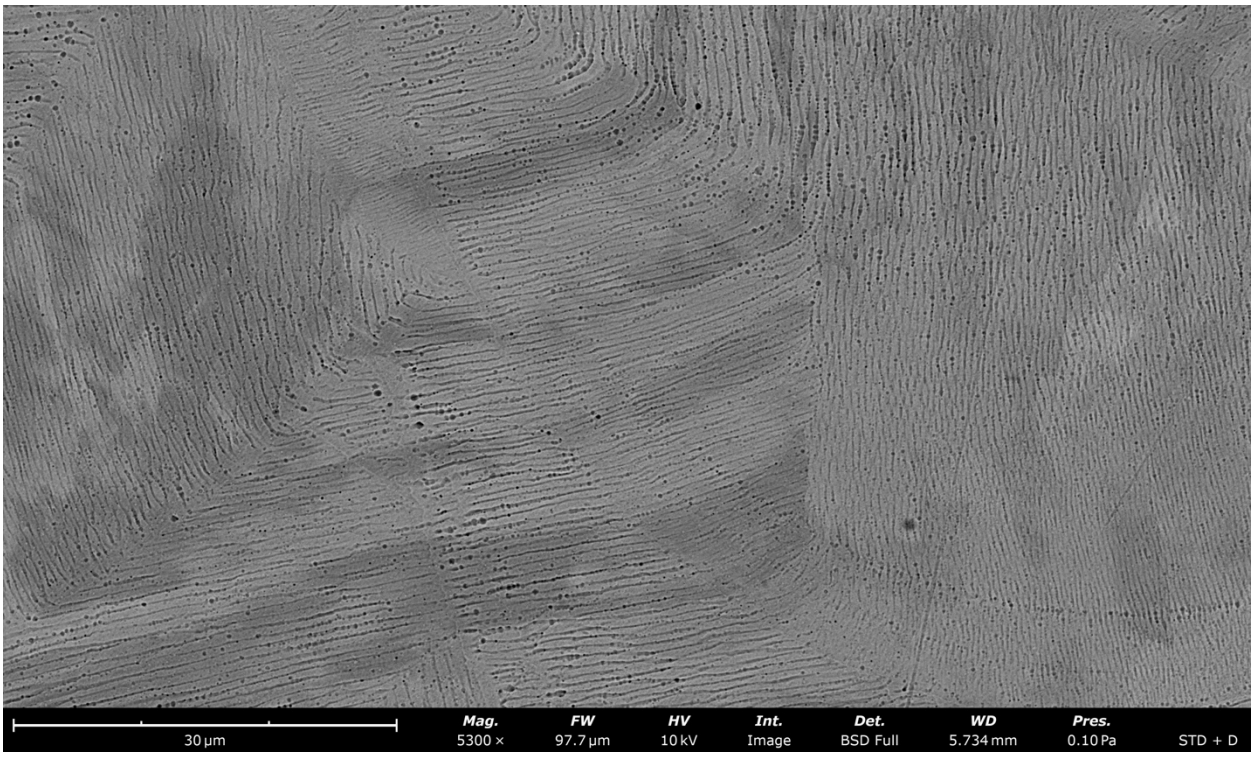

Figure 19*: Example of backscattered electron (BSE) image of solidification features in AM 316L stainless steel.*

Figure 20 shows an array of melt pools on a Ti-25Nb (at%) substrate after multiple laser scans with a hatch distance of 120 μm. As can be seen, the melt pool in the cross-sectional view has an ellipsoid shape. The size of the melt pool mostly depends on the laser parameters, such as laser power and scanning speed. After the first wave of energy absorption by the incoming laser, the partially reflected laser can continue to penetrate deeper, resulting in deeper "laser drilling".

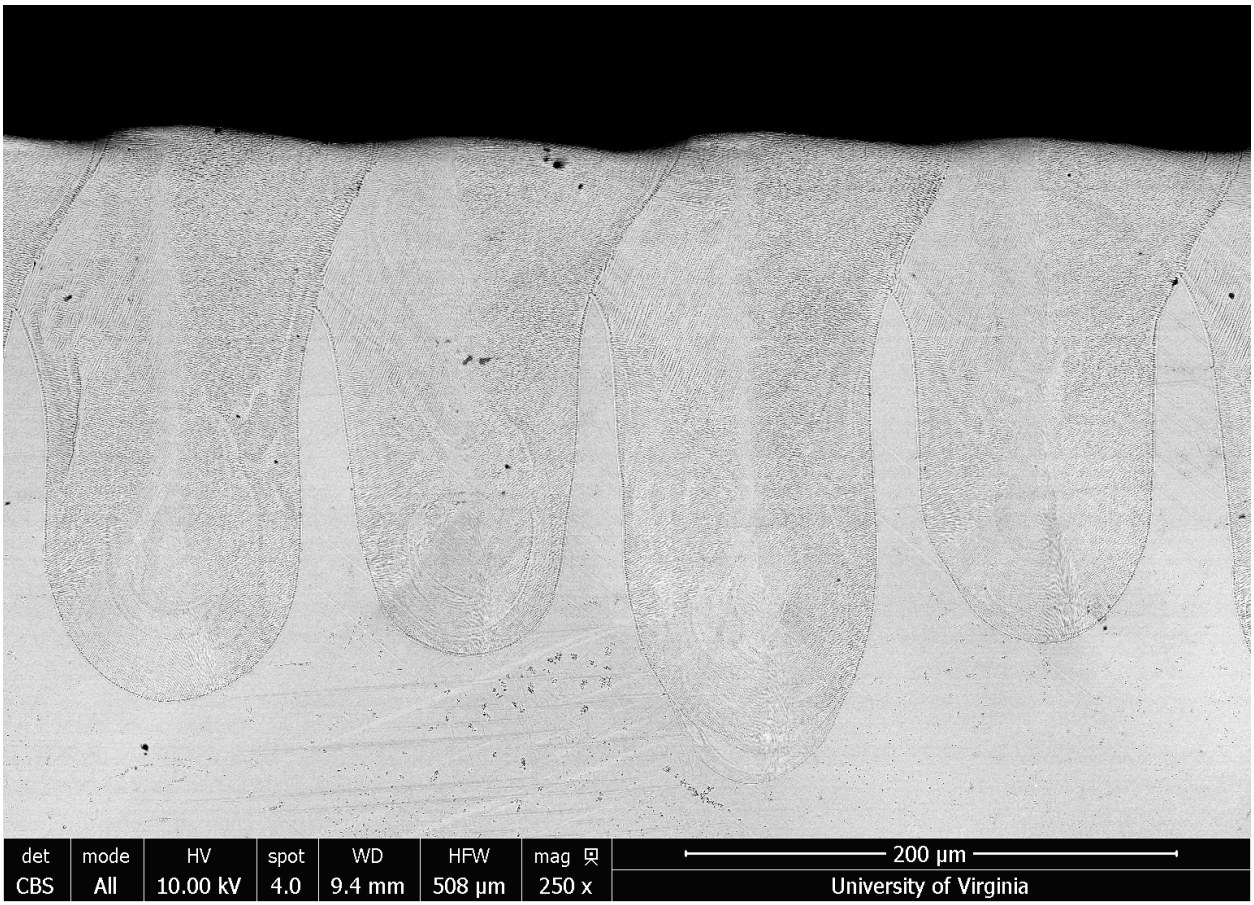

Figure 20*: BSE image of the cross-sectioned view of melt pools in the Ti-25Nb (at%) substrate after laser scanning. Contrast and brightness are adjusted for revealing melt pools and solidification features.*

A melt pool can be considered a single melting event caused by the laser and is thus considered a "building block" for constructing actual parts. Therefore, studying melt pools is a fundamental yet essential step in additive manufacturing. Melt pool studies provide several critical pieces of information. Firstly, the actual size of the melt pool, particularly the width and depth, is a crucial factor. The width of the melt pool determines the maximum hatch distance needed to achieve fully dense parts, while the depth of the melt pool determines the maximum layer thickness for the same reason. Secondly, the microstructure inside the melt pool reflects the actual AM microstructure in the final parts, such as solidification features, elemental partitioning, and phase

composition/distribution. This information is essential for assessing material performance. Lastly, the formation of the melt pool can become unstable/unpredictable when the "laser drilling" effect becomes too severe. This is often known as keyholing, which can result in porosity/cracks inside the AM parts.

1.3.4. Direction-dependency in AM

After additive fabrication using a layer-by-layer approach, an AM part is composed of layers of melt pools, as shown in **Figure 21**. As can be seen, the melt pools overlap to create a fully dense part and most regions undergo multiple remelting and reheating during the AM process. This mechanism governs the growth of grains during AM. Grains tend to grow along the direction of the maximum thermal gradient, which is typically from the boundaries of the melt pool toward its centerline. Therefore, it is common to observe elongated grains' growing direction follows the same trend, as shown in **Figure 21**. Additionally, as the laser spot moves across the powder bed, the maximum thermal gradient can dynamically shift along with the laser spot. Thus, grains tend to grow at an angle tilted upwards along the laser scanning direction. Because of such a phenomenon, the performance of AM parts often has a strong direction-dependency.

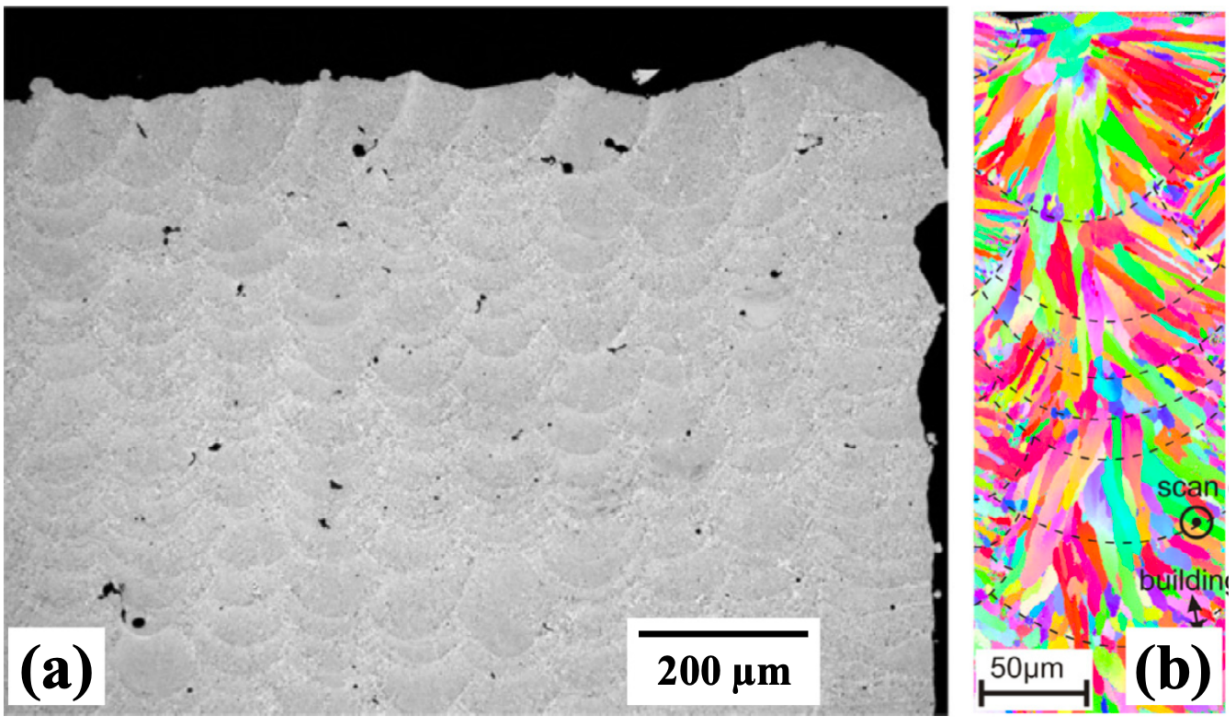

***Figure 21**: Example of melt pool arrays as well as grain growth of a AlSi10Mg sample using LPBF [38].*

The dependency on grain orientation can be regulated by adjusting the G/R ratio. This can be achieved by varying the parameters of the energy source, such as power, scanning speed, beam profile, and scanning path. For instance, Dehoff et al. demonstrated that the grain orientation of an FCC nickel-based superalloy IN718 could be controlled using PBF (electron beam) [39] . As illustrated in **Figure 22**, the grains formed the letters "DOE" with a random texture, while the remaining grains displayed a strong <100> orientation. The approach involved using two distinct printing strategies to induce equiaxed solidification mode for the majority of grains in the "DOE" region and a columnar solidification mode to achieve the desired <100> orientation. Plotkowski et al. advanced this further by using a novel scan pattern algorithm to precisely manipulate solidification modes, forming the shape of the Mona Lisa on IN 718[40], shown in **Figure 23**.

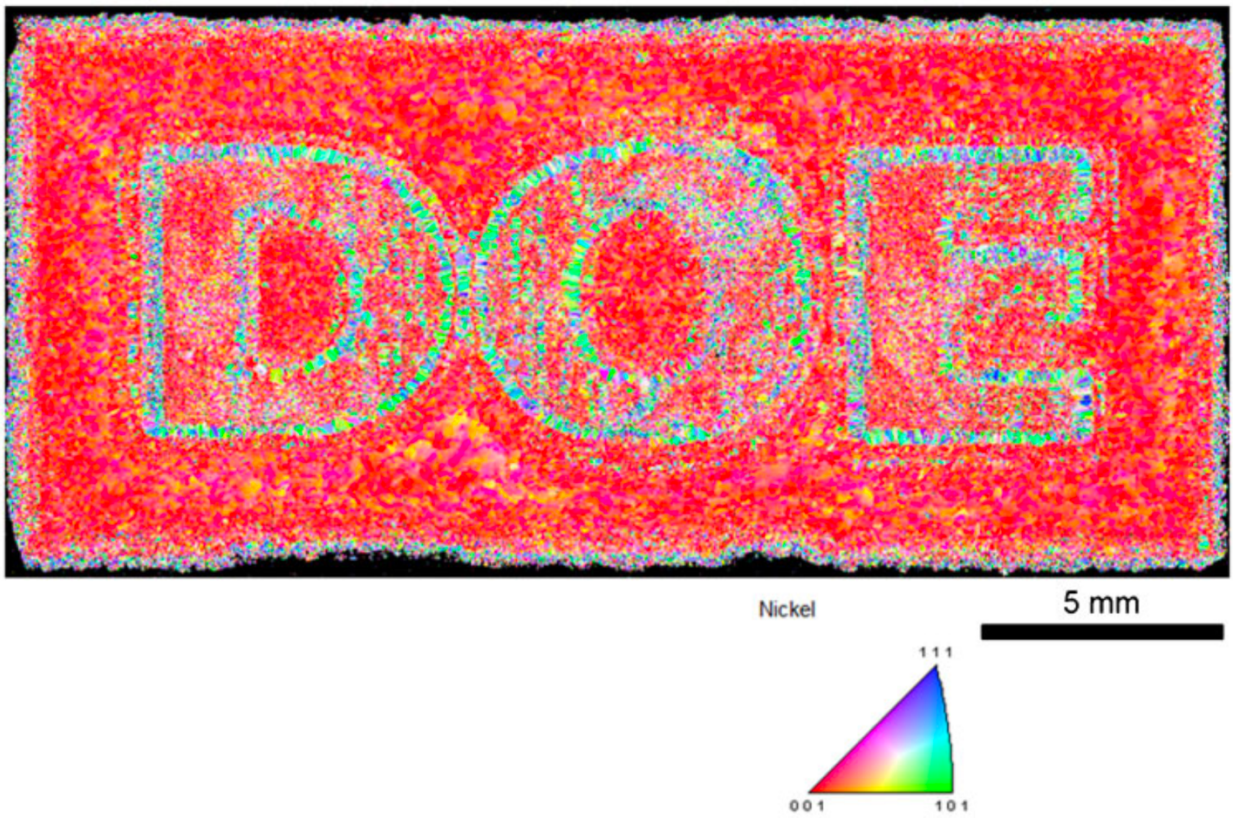

***Figure 22**: Electron backscatter diffraction (EBSD) orientation mapping of an AM sample of IN718 built by applying distinct printing strategies [39].*

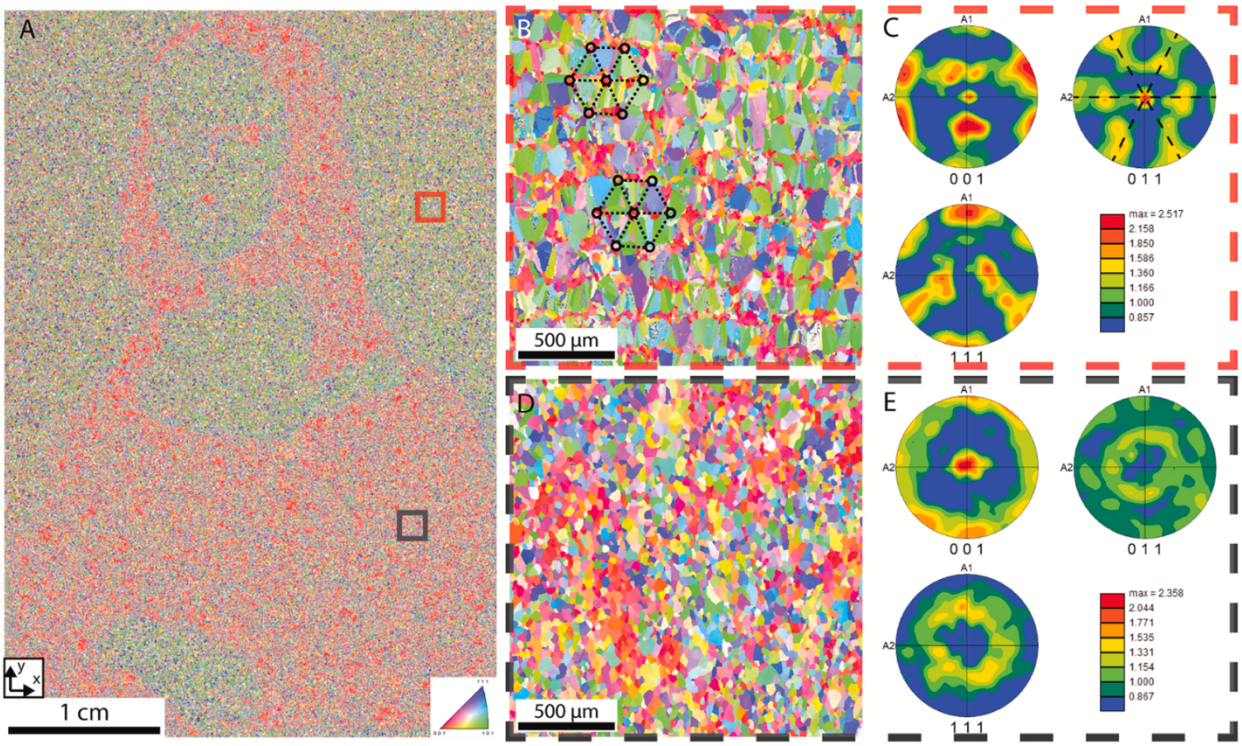

***Figure 23**: EBSD orientation mapping of AM IN718 superalloy, showing the Mona Lisa [40].*

1.3.5. AM metastable β-Ti alloys

The study of metastable β-Ti alloys in additive manufacturing is a relatively new field. At the time of writing, there were less than 10 published studies available that comprehensively investigated the microstructure and printability of these materials. Due to their novel metastability, several factors in AM can substantially influence the resultant microstructures. Elemental micro-segregation, for example, can occur during the rapid solidification that takes place during the AM process. In a β-Ti alloys, like Ti-Nb samples, processed with a laser, Roehling et al. observed a difference in β stabilizers, such as Nb content, of more than 5 at.% near the melt pool boundaries and cellular boundaries [41]. Such compositional heterogeneity can lead to unexpected outcomes due to the undulation of the stability of the β phase through solidification features. Regions of stable β, metastable β (α' martensite), and metastable β (α'' martensite) can form within the

sample material after AM processing, depending on the degree of micro-segregation of β stabilizers. Additionally, the composition and temperature field during rapid solidification can significantly alter the behavior of secondary phase nucleation. Precipitates such as α, α', α'', and ω phases may appear or disappear near the melt pool boundaries (high cooling rate) or near the surface of the melt pool (low cooling rate) [29]. As laser parameters are changed, the perceived nucleation behaviors may also change accordingly, making the interpretation of the resulting microstructures challenging. Finally, existing phases, together with unique defects and thermal strain developed during rapid solidification, can also modify the deformation behaviors [35]. Mechanisms such as stress-induced martensitic transformation and stress-induced twinning have been reported in the literature [42–45].

What's more, comparing results between studies is challenging due to the various scanning strategies, deposit methods, and feedstock options employed. For instance, PBF (or SLM) is a popular deposit method that generates smaller melt pools but more extreme thermal gradients than DED, leading to differences in the size and type of solidification features produced by the two methods [24]. Additionally, using pre-alloyed powder can yield different results than an elemental powder mixture fused in-situ. For example, Schulze et al. found that the SLM-printed Ti-42Nb (wt%) alloy, containing roughly 26% Nb (by atomic percent), had a modulus of 61 GPa [46]. In contrast, Wang et al. claimed that the SLM-printed Ti-25Nb (at%) alloy, made using an elemental powder mixture, had a modulus of less than 20 GPa [44]. However, no detailed microstructures were revealed in that study and the similar results have not been replicated in other studies. Overall, systematic understanding of microstructure of AM metastable β-Ti alloys as well as the potential strategies of attaining low modulus in these materials is significantly lacking.

1.4. Knowledge Gaps - Achieving Ultralow Modulus in Metastable β-Ti Alloys

The elastic response of a metal is determined by its crystal structure and the bonding between its atoms [47]. Achieving a low elastic modulus in metals generally involves alloying with other elements or increasing crystalline anisotropy. The former approach effectively reduces the bonding force of the lattice, while the latter approach reduces the macroscopic elastic constants along the loading direction by reorienting grains along a more compliant direction [2].

In β-Ti alloys, the bonding force tends to be inversely correlated with the metal d-orbital level, which is affected by the composition and the choice of β stabilizers [48], shown in **Figure 24**. To minimize the elastic modulus, Morinaga et al. proposed a d-electron-based approach for the compositional design of β-Ti alloys, aiming for higher bond order (Bo) and higher d-orbital energy level (Md) [48]. However, achieving an elastic modulus below 50 GPa has proven difficult with this approach [48,49].

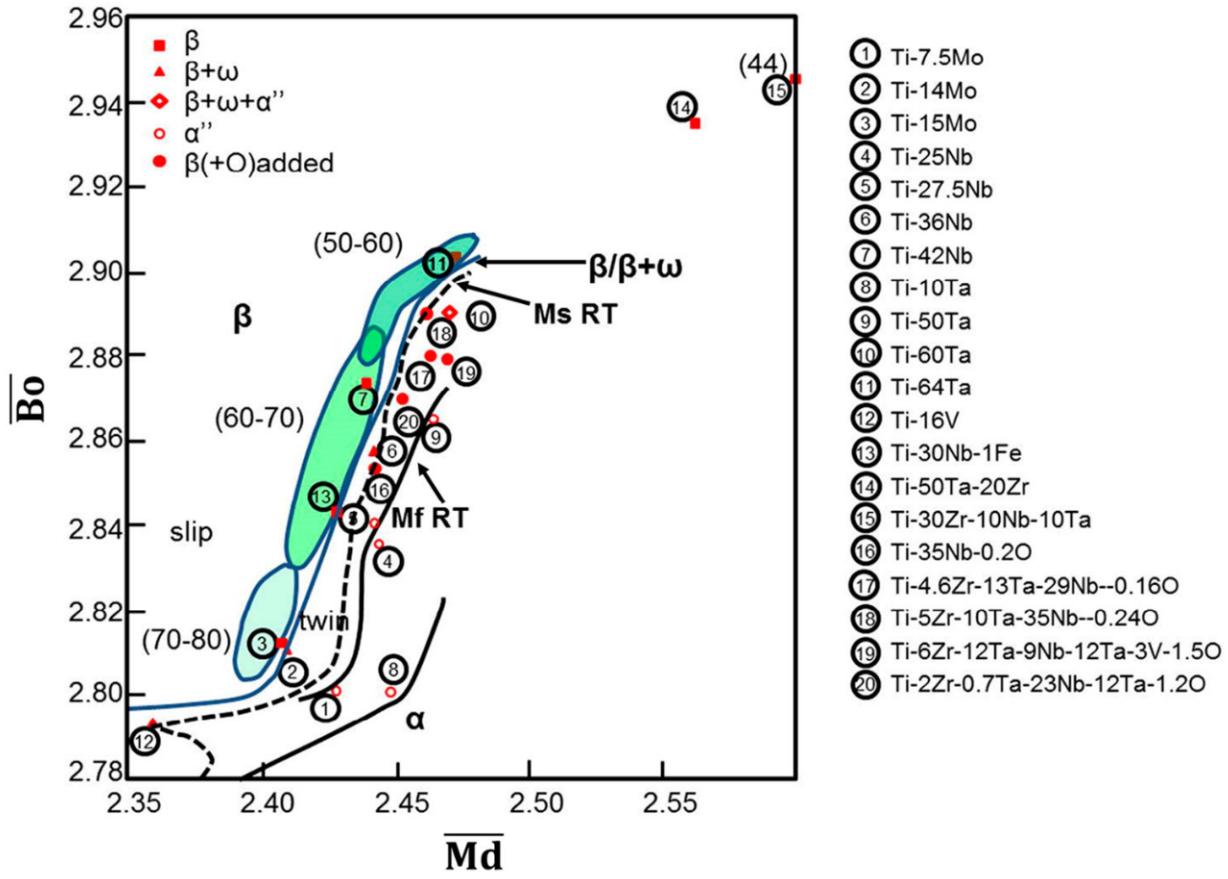

***Figure 24**: $\overline{Bo} - \overline{Md}$ diagram for selected β-Ti alloys. Bo stands for bond order, a measure of population of overlapped electrons shared by two atoms. Md stands for metal d-orbital energy level [48].*

Additionally, enhancing the material's texture and aligning the less rigid crystallographic direction with the loading direction can effectively decrease the elastic modulus. For instance, Tane et al. illustrated that a Ti-Nb-Ta-Zr single crystal could display an elastic modulus of approximately 35 GPa along the <100> direction, whereas its isotropic polycrystal counterpart may possess an elastic modulus ex**ce**eding 50 GPa [50]. However, it is impractical to grow single crystal that can be used for implants. Plus, the modulus reduction from texture has a visible theoretical limitation, like 35 GPa in this example.

Alternatively, it may be possible to take advantages of the instability β phase in metastable β-Ti alloys. The hypothesis is that if the alloys can initiate stress-induced martensitic transformation (SIMT) at a low applied stress, then this can be equivalent to the material possesses lower modulus. Yet, there are currently no studies in the literature that can conclusively demonstrate the feasibility of this approach. Furthermore, there are no established studies that explain the actual microstructural requirements needed to achieve ultralow modulus in metastable β-Ti alloys.

1.5.Dissertation Overview

The aim of this dissertation is to offer insights into achieving ultralow modulus in metastable β-Ti alloys for biomedical applications. Both conventional metallurgy and additive manufacturing approaches will be proposed and discussed. Ti-Nb shape memory alloy was used across the entire dissertation and the composition of 25Nb at% was selected due to its martensitic transformation temperature being around room temperature. The dissertation is divided into two parts: the first part provides actual metallurgical approaches (Chapter 2) using thermo-mechanical processing to assist low stress SIMT, while the second part focuses on additive manufacturing methods. The second part will be further divided into two chapters, which will demonstrate the microstructure (Chapter 3) and mechanical properties of AM Ti-25Nb (Chapter 4).

Finally, this dissertation concludes with key learnings and provides insights and recommendations for future studies of metastable β-Ti alloys, as well as tailoring material properties in additive manufacturing.

1.6.References

[1] M. Long, H.J. Rack, Titanium alloys in total joint replacement--A materials science perspective., Biomaterials. 19 (1998) 1621–39. https://doi.org/10.1016/S0142-9612(97)00146-4.

[2] G. Lutjering, J.C. Williams, G Lütjering; J C Williams, Titanium, Springer, Berlin; New York, 2007. https://doi.org/10.1007/978-3-540-73036-1.

[3] M.F. Ashby, Materials selection in mechanical design, 5th ed., Butterworth-Heinemann, 2016.

[4] R. Kolli, A. Devaraj, A Review of Metastable Beta Titanium Alloys, Metals (Basel). 8 (2018) 506. https://doi.org/10.3390/met8070506.

[5] David L. Moffat, Phase transformations in the titanium-niobium binary alloy system, University of Wisconsin - Madison, 1985. https://www.worldcat.org/title/phase-transformations-in-the-titanium-niobium-binary-alloy-system/oclc/4435683086&referer=brief_results (accessed May 15, 2021).

[6] H.Y.Y. Kim, Y. Ikehara, J.I.I. Kim, H. Hosoda, S. Miyazaki, Martensitic transformation, shape memory effect and superelasticity of Ti–Nb binary alloys, Acta Mater. 54 (2006) 2419–2429. https://doi.org/10.1016/j.actamat.2006.01.019.

[7] J.J. Gutiérrez Moreno, M. Bönisch, N.T. Panagiotopoulos, M. Calin, D.G. Papageorgiou, A. Gebert, J. Eckert, G.A. Evangelakis, C.E. Lekka, Ab-initio and experimental study of phase stability of Ti-Nb alloys, J. Alloys Compd. 696 (2017) 481–489. https://doi.org/10.1016/j.jallcom.2016.11.231.

[8] J. Ma, I. Karaman, R.D. Noebe, High temperature shape memory alloys, Int. Mater. Rev. 55 (2010) 257–315. https://doi.org/10.1179/095066010X12646898728363.

[9] S. Miyazaki, My Experience with Ti–Ni-Based and Ti-Based Shape Memory Alloys, Shape Mem. Superelasticity. 3 (2017) 279–314. https://doi.org/10.1007/s40830-017-0122-3.

[10] R. Salloom, D. Reith, R. Banerjee, S.G. Srinivasan, First principles calculations on the effect of interstitial oxygen on phase stability and β–α″ martensitic transformation in Ti–Nb alloys, J. Mater. Sci. 53 (2018) 11473–11487. https://doi.org/10.1007/s10853-018-2381-6.

[11] M. Bönisch, M. Calin, L. Giebeler, A. Helth, A. Gebert, W. Skrotzki, J. Eckert, Composition-dependent magnitude of atomic shuffles in Ti–Nb martensites, J. Appl. Crystallogr. 47 (2014) 1374–1379. https://doi.org/10.1107/S1600576714012576.

[12] Y.W. Chai, H.Y. Kim, H. Hosoda, S. Miyazaki, Self-accommodation in Ti-Nb shape memory alloys, Acta Mater. 57 (2009) 4054–4064. https://doi.org/10.1016/j.actamat.2009.04.051.

[13] K. Bhattacharya, Microstructure of martensite : why it forms and how it gives rise to the shape-memory effect / Kaushik Bhattacharya, Oxford University Press, Oxford, 2003.

[14] H. Tobe, H.Y. Kim, T. Inamura, H. Hosoda, T.H. Nam, S. Miyazaki, Effect of Nb content on deformation behavior and shape memory properties of Ti-Nb alloys, J. Alloys Compd. 577 (2013) S435–S438. https://doi.org/10.1016/j.jallcom.2012.02.023.

[15] D. Ping, Review on ω Phase in Body-Centered Cubic Metals and Alloys, Acta Metall. Sin. (English Lett. 2014 271. 27 (2014) 1–11. https://doi.org/10.1007/S40195-013-0014-2.

[16] S. Banerjee, R. Tewari, G.K. Dey, Omega phase transformation - Morphologies and mechanisms, Int. J. Mater. Res. 97 (2006) 963–977. https://doi.org/10.3139/146.101327.

[17] H.Y. Kim, J.I. Kim, T. Inamura, H. Hosoda, S. Miyazaki, Effect of thermo-mechanical

treatment on mechanical properties and shape memory behavior of Ti–(26–28)at.% Nb alloys, Mater. Sci. Eng. A. 438–440 (2006) 839–843. https://doi.org/https://doi.org/10.1016/j.msea.2006.02.136.

[18] J.F. Xiao, Z. Nie, Z. Ma, G. Liu, F. Hao, C. Tan, $ω$ precipitation: Deformation regulator in metastable titanium alloys, Mater. Sci. Eng. A-Structural Mater. Prop. Microstruct. Process. 772 (2020) 138687.

[19] S. Cai, J.E. Schaffer, Y. Ren, Deformation of a Ti-Nb alloy containing α"-martensite and omega phases, Appl. Phys. Lett. 106 (2015) 131907. https://doi.org/10.1063/1.4916960.

[20] P. Castany, Y. Yang, E. Bertrand, T. Gloriant, Reversion of a Parent 310 α″ Martensitic Twinning System at the Origin of {332 } 113 ©β Twins Observed in Metastable β Titanium Alloys, Phys. Rev. Lett. 117 (2016). https://doi.org/10.1103/PhysRevLett.117.245501.

[21] A. Devaraj, S. Nag, R. Srinivasan, R.E.A. Williams, S. Banerjee, R. Banerjee, H.L. Fraser, Experimental evidence of concurrent compositional and structural instabilities leading to ω precipitation in titanium–molybdenum alloys, Acta Mater. 60 (2012) 596–609. https://doi.org/https://doi.org/10.1016/j.actamat.2011.10.008.

[22] H.Y. Kim, L. Wei, S. Kobayashi, M. Tahara, S. Miyazaki, Nanodomain structure and its effect on abnormal thermal expansion behavior of a Ti-23Nb-2Zr-0.7Ta-1.2O alloy, Acta Mater. 61 (2013) 4874–4886. https://doi.org/10.1016/j.actamat.2013.04.060.

[23] M. Tahara, H.Y. Kim, T. Inamura, H. Hosoda, S. Miyazaki, Lattice modulation and superelasticity in oxygen-added β-Ti alloys, Acta Mater. 59 (2011) 6208–6218. https://doi.org/10.1016/j.actamat.2011.06.015.

[24] T. DebRoy, H.L. Wei, J.S. Zuback, T. Mukherjee, J.W. Elmer, J.O. Milewski, A.M.

Beese, A. Wilson-Heid, A. De, W. Zhang, Additive manufacturing of metallic components – Process, structure and properties, Prog. Mater. Sci. 92 (2018) 112–224. https://doi.org/10.1016/j.pmatsci.2017.10.001.

[25] X. Wang, S. Xu, S. Zhou, W. Xu, M. Leary, P. Choong, M. Qian, M. Brandt, Y.M. Xie, Topological design and additive manufacturing of porous metals for bone scaffolds and orthopaedic implants: A review, Elsevier Ltd, 2016. https://doi.org/10.1016/j.biomaterials.2016.01.012.

[26] D. Zhao, F. Witte, F. Lu, J. Wang, J. Li, L. Qin, Current status on clinical applications of magnesium-based orthopaedic implants: A review from clinical translational perspective, Biomaterials. 112 (2017) 287–302. https://doi.org/10.1016/j.biomaterials.2016.10.017.

[27] R. Dimitriou, E. Jones, D. McGonagle, P. V Giannoudis, Bone regeneration: current concepts and future directions, BMC Med. 9 (2011) 66. https://doi.org/10.1186/1741-7015-9-66.

[28] R. Florencio-Silva, G.R. da S. Sasso, E. Sasso-Cerri, M.J. Simões, P.S. Cerri, Biology of Bone Tissue: Structure, Function, and Factors That Influence Bone Cells., Biomed Res. Int. 2015 (2015) 421746. https://doi.org/10.1155/2015/421746.

[29] J.P. Oliveira, T.G. Santos, R.M. Miranda, Revisiting fundamental welding concepts to improve additive manufacturing: From theory to practice, Prog. Mater. Sci. 107 (2020) 100590. https://doi.org/10.1016/j.pmatsci.2019.100590.

[30] Z. Zhu, W. Li, Q.B. Nguyen, X. An, W. Lu, Z. Li, F.L. Ng, S.M. Ling Nai, J. Wei, Enhanced strength–ductility synergy and transformation-induced plasticity of the selective laser melting fabricated 304L stainless steel, Addit. Manuf. 35 (2020) 101300. https://doi.org/10.1016/j.addma.2020.101300.

[31] Y. Li, K. Chen, R.L. Narayan, U. Ramamurty, Y. Wang, J. Long, N. Tamura, X. Zhou, Multi-scale microstructural investigation of a laser 3D printed Ni-based superalloy, Addit. Manuf. 34 (2020) 101220. https://doi.org/10.1016/j.addma.2020.101220.

[32] P. Deng, H. Yin, M. Song, D. Li, Y. Zheng, B.C. Prorok, X. Lou, On the Thermal Stability of Dislocation Cellular Structures in Additively Manufactured Austenitic Stainless Steels: Roles of Heavy Element Segregation and Stacking Fault Energy, JOM. 72 (2020) 4232–4243. https://doi.org/10.1007/s11837-020-04427-7.

[33] N. Li, S. Huang, G. Zhang, R. Qin, W. Liu, H. Xiong, G. Shi, J. Blackburn, Progress in additive manufacturing on new materials: A review, J. Mater. Sci. Technol. 35 (2019) 242–269. https://doi.org/10.1016/j.jmst.2018.09.002.

[34] S. Liu, Y.C. Shin, Additive manufacturing of Ti6Al4V alloy: A review, Mater. Des. 164 (2019). https://doi.org/10.1016/j.matdes.2018.107552.

[35] Y. Kok, X.P. Tan, P. Wang, M.L.S. Nai, N.H. Loh, E. Liu, S.B. Tor, Anisotropy and heterogeneity of microstructure and mechanical properties in metal additive manufacturing: A critical review, Mater. Des. 139 (2018) 565–586. https://doi.org/10.1016/j.matdes.2017.11.021.

[36] T. Nakano, Selective Laser Melting BT - Multi-dimensional Additive Manufacturing, in: S. Kirihara, K. Nakata (Eds.), Springer Singapore, Singapore, 2021: pp. 3–26. https://doi.org/10.1007/978-981-15-7910-3_1.

[37] D.A. Porter, K.E. Easterling, M.Y. Sherif, Phase Transformations in Metals and Alloys, Fourth Edition, Phase Transform. Met. Alloy. Fourth Ed. (2021) 1–556. https://doi.org/10.1201/9781003011804/PHASE-TRANSFORMATIONS-METALS-ALLOYS-DAVID-PORTER-KENNETH-EASTERLING-MOHAMED-SHERIF.

[38] L. Thijs, K. Kempen, J.P. Kruth, J. Van Humbeeck, Fine-structured aluminium products with controllable texture by selective laser melting of pre-alloyed AlSi10Mg powder, Acta Mater. 61 (2013) 1809–1819. https://doi.org/10.1016/J.ACTAMAT.2012.11.052.

[39] R.R. Dehoff, M. Kirka, W.J. Sames, H. Bilheux, A.S. Tremsin, L.E. Lowe, S.S. Babu, Site specific control of crystallographic grain orientation through electron beam additive manufacturing, Mater. Sci. Technol. (United Kingdom). 31 (2015) 931–938. https://doi.org/10.1179/1743284714Y.0000000734.

[40] A. Plotkowski, J. Ferguson, B. Stump, W. Halsey, V. Paquit, C. Joslin, S.S. Babu, A. Marquez Rossy, M.M. Kirka, R.R. Dehoff, A stochastic scan strategy for grain structure control in complex geometries using electron beam powder bed fusion, Addit. Manuf. 46 (2021). https://doi.org/10.1016/j.addma.2021.102092.

[41] J.D. Roehling, A. Perron, J.L. Fattebert, T. Haxhimali, G. Guss, T.T. Li, D. Bober, A.W. Stokes, A.J. Clarke, P.E.A. Turchi, M.J. Matthews, J.T. McKeown, Rapid Solidification in Bulk Ti-Nb Alloys by Single-Track Laser Melting, JOM. 70 (2018) 1589–1597. https://doi.org/10.1007/s11837-018-2920-2.

[42] D. Kalita, Ł. Rogal, P. Bobrowski, T. Durejko, T. Czujko, A. Antolak-Dudka, E. Cesari, J. Dutkiewicz, Superelastic behavior of ti-nb alloys obtained by the laser engineered net shaping (Lens) technique, Materials (Basel). 13 (2020) 1–14. https://doi.org/10.3390/ma13122827.

[43] W. Chen, C. Chen, X. Zi, X. Cheng, X. Zhang, Y.C. Lin, K. Zhou, Controlling the microstructure and mechanical properties of a metastable β titanium alloy by selective laser melting, Mater. Sci. Eng. A. 726 (2018) 240–250. https://doi.org/10.1016/j.msea.2018.04.087.

[44] Q. Wang, C. Han, T. Choma, Q. Wei, C. Yan, B. Song, Y. Shi, Effect of Nb content on microstructure, property and in vitro apatite-forming capability of Ti-Nb alloys fabricated via selective laser melting, Mater. Des. 126 (2017) 268–277. https://doi.org/10.1016/j.matdes.2017.04.026.

[45] N. Hafeez, S. Liu, E. Lu, L. Wang, R. Liu, W. lu, L.C. Zhang, Mechanical behavior and phase transformation of β-type Ti-35Nb-2Ta-3Zr alloy fabricated by 3D-Printing, J. Alloys Compd. 790 (2019) 117–126. https://doi.org/10.1016/j.jallcom.2019.03.138.

[46] C. Schulze, M. Weinmann, C. Schweigel, O. Keßler, R. Bader, Mechanical properties of a newly additive manufactured implant material based on Ti-42Nb, Materials (Basel). 11 (2018). https://doi.org/10.3390/ma11010124.

[47] G.S. Rohrer, Structure and Bonding in Crystalline Materials, Struct. Bond. Cryst. Mater. (2001). https://doi.org/10.1017/CBO9780511816116.

[48] S. Bahl, S. Suwas, K. Chatterjee, Comprehensive review on alloy design, processing, and performance of β Titanium alloys as biomedical materials, Https://Doi.Org/10.1080/09506608.2020.1735829. 66 (2020) 114–139. https://doi.org/10.1080/09506608.2020.1735829.

[49] L.-C. Zhang, L.-Y. Chen, A Review on Biomedical Titanium Alloys: Recent Progress and Prospect, Adv. Eng. Mater. 21 (2019) 1801215. https://doi.org/10.1002/ADEM.201801215.

[50] M. Tane, S. Akita, T. Nakano, K. Hagihara, Y. Umakoshi, M. Niinomi, H. Nakajima, Peculiar elastic behavior of Ti–Nb–Ta–Zr single crystals, Acta Mater. 56 (2008) 2856–2863. https://doi.org/https://doi.org/10.1016/j.actamat.2008.02.017.

[51] R. Merickse-Stern, D. Aerni, A.H. Geering, D. Buser, Long-term evaluation of non-

submerged hollow cylinder implants. Clinical and radiographic results., Clin. Oral Implants Res. 12 (2001) 252–9.

[52] M.I.Z. Ridzwan, S. Shuib, A.Y. Hassan, A.A. Shokri, M.N. Mohamad Ibrahim, Problem of Stress Shielding and Improvement to the Hip Implant Designs: A Review, J. Med. Sci. 7 (2007) 460–467. https://doi.org/10.3923/jms.2007.460.467.

[53] A. Bandyopadhyay, F. Espana, V.K. Balla, S. Bose, Y. Ohgami, N.M. Davies, Influence of porosity on mechanical properties and in vivo response of Ti6Al4V implants, Acta Biomater. 6 (2010) 1640–1648. https://doi.org/10.1016/J.ACTBIO.2009.11.011.

[54] L.-C. Zhang, Y. Liu, S. Li, Y. Hao, Additive Manufacturing of Titanium Alloys by Electron Beam Melting: A Review, Adv. Eng. Mater. 20 (2018) 1700842. https://doi.org/10.1002/adem.201700842.

[55] L.J. Gibson, Mechanical Behavior of Metallic Foams, Annu. Rev. Mater. Sci. 30 (2000) 191–227. https://doi.org/10.1146/annurev.matsci.30.1.191.

[56] J. Banhart, Manufacture, characterisation and application of cellular metals and metal foams, Pergamon, 2001. https://doi.org/10.1016/S0079-6425(00)00002-5.

[57] X. Wang, Y. Li, J. Xiong, P.D. Hodgson, C. Wen, Porous TiNbZr alloy scaffolds for biomedical applications, Acta Biomater. 5 (2009) 3616–3624. https://doi.org/10.1016/J.ACTBIO.2009.06.002.

[58] G.H. Loh, E. Pei, D. Harrison, M.D. Monzón, An overview of functionally graded additive manufacturing, Addit. Manuf. 23 (2018) 34–44. https://doi.org/10.1016/j.addma.2018.06.023.

[59] W. Xu, M. Brandt, S. Sun, J. Elambasseril, Q. Liu, K. Latham, K. Xia, M. Qian, Additive manufacturing of strong and ductile Ti-6Al-4V by selective laser melting via in situ

martensite decomposition, Acta Mater. 85 (2015) 74–84.

https://doi.org/10.1016/j.actamat.2014.11.028.

2. Low Modulus High Strength Metastable Beta Ti-Nb Alloys

2.1. Introduction

β and metastable β Ti-alloys are regarded as a new generation of biomedical structural materials, particularly for orthopedic applications. In addition to superior biocompatibility, high strength, and high wear resistance, the primary advantage of β Ti-alloys over other alternatives, such as stainless steels and Co-Cr based alloys, is their exceptional biomechanical compatibility [1]. A critical challenge in the field of orthopedic implants is that implant materials typically exhibit an elastic response that is significantly greater than that of human bones in terms of elastic modulus. This discrepancy leads to a complication known as "stress shielding," which results in bone resorption over time [2,3]. β and metastable β Ti alloys, which possess lower moduli compared to other Ti-based alloys, have also been found to be capable of adjusting their elastic modulus by altering the β phase stability through meticulous alloy design. One approach involves identifying alloy compositions that achieve higher bond order (Bo) and d-orbital energy levels (Md) [4]. For instance, Ti-Mo-Zr-Fe alloys and Ti-Nb-Ta-Zr alloys can attain lower moduli of 50-70 GPa, which is significantly lower than the α CP-Ti's modulus of 110 GPa [1]. However, this empirical approach has been found to have practical limitations in discovering new alloys with even lower moduli.

Another approach involves fabricating highly textured β and metastable β alloys along the loading direction to further reduce the elastic modulus. For example, Tane et al. demonstrated that a Ti-Nb-Ta-Zr single crystal sample exhibits an elastic modulus of around 35 GPa along the <100> direction [5]. However, growing single crystals for implants is challenging and expensive. A more practical method is to use thermo-mechanical processes such as cold-rolling or swaging to produce highly textured components. Nevertheless, the typical rolling texture of β Ti alloys is <110> along

the rolling direction [6]. Due to the orientation dependence of elastic modulus of β Ti alloys, the <110> direction appears to be much stiffer than the <100> direction [5].

Among metastable β Ti alloys, there is a specific group of Ti-alloys known as β-Ti-based shape memory alloys. Similar to NiTi-based shape memory alloys used in aerospace applications, these alloys can undergo martensitic phase transformation from the high-temperature β (austenite) phase to the low-temperature orthorhombic α'' (martensite) phase [7]. One of the unique features of shape memory alloys is superelasticity, a phenomenon of reversible stress-induced martensitic phase transformation (SIMT) from the austenite phase to the martensite phase in the elastic deformation regime [7]. Notably, the apparent modulus during SIMT can be significantly lower than the moduli of both the austenite and martensite phases [8]. One hypothesis suggests that if the transformation stress initiating SIMT can be brought close to "0," it could effectively achieve an ultra-low modulus that matches the value of human bone.

The microstructural requirements for ensuring SIMT initiation when low external load is applied remain unclear. The chemical composition of β Ti alloys can significantly influence phase transformation temperature and stress [9,10]. However, the actual transformation stress is governed by the microstructure. Firstly, the initial phase should predominantly consist of the β phase, which is a prerequisite for macroscopic significance of modulus reduction under SIMT. Nevertheless, both the presence of a secondary phase, such as the ω phase, and the existence of dislocations within the microstructure can impede martensitic phase transformation [9]. At the same time, these features can also stabilize SIMT [9]. As a result, it remains uncertain whether any thermo-mechanical processes can achieve the desired microstructure for triggering SIMT at low external stress levels.

This study proposes thermo-mechanical procedures to achieve a low elastic modulus in Ti-25Nb (at%) alloys. The tensile performance of Ti-25Nb (at%) under various thermo-mechanical conditions was investigated. Furthermore, the key microstructural components necessary for achieving such a low modulus were demonstrated.

2.2. Methods

Ti-25Nb (at%) rectangular billets with a 3 mm thickness, produced by vacuum arc melting, were solution heated at 900°C for 2 hours in an argon atmosphere and water quenched. These billets were then cold-rolled to achieve a 67% thickness reduction to 1 mm, using multiple passes. Flat tensile dog-bone samples were cut from the cold-rolled sheets with a wire electrical discharge machine (w-EDM). These samples were then furnace heat-treated under various conditions at 300°C, 400°C, 500°C, and 600°C for 10 minutes, 20 minutes, 1 hour, and 24 hours, all followed by water quenching.

Tensile tests were conducted on an MTS hydraulic loading frame, with an external extensometer directly attached to the front surface within the gauge section of the sample to measure deformation. Additionally, tensile experiments with in-situ synchrotron 2θ x-ray diffraction (XRD) were conducted at Argonne National Laboratory's Advanced Photon Source (APS) beamline 11-ID-C. Two samples with two thermo-mechanical treatments were selected: one as a cold-rolled sample and one with additional heat treatment at 300°C for 10 minutes. The load frame was set to move at a strain rate of 0.001 s^{-1} up to a total of 0.5 mm displacement. During loading, the sample was exposed to a high-energy X-ray with 105.7 keV of beam energy, and the corresponding 2D XRD patterns were recorded. The XRD data was then analyzed by "FIT2D" software [11] and 1D XRD patterns were converted as well.

2.3. Results & Discussion

Thermo-mechanical treatments have a significant effect on the β phase stability of Ti-25Nb (at%). Even a short aging at low temperatures can significantly reduce the elastic modulus of Ti-25Nb (at%), as shown in **Figure 25**. For example, the as-rolled sample (at 67% cold rolling) has an elastic modulus of 46 GPa, while samples with additional heat treatment at 300°C or 400°C for 10 minutes (CR + 300°C 10m and CR + 400°C 10m) have elastic moduli of 31.7 and 30.1 GPa, respectively. These low moduli suggest microstructural changes during low-temperature aging. Both heat-treated samples exhibit a double-yielding phenomenon (S-shaped curves) with the first "yielding" occurring around 200 MPa and another above 600 MPa, as observed in their stress-strain curves. The as cold-rolled sample has a yield strength of around 625 MPa, indicating that the first "yielding" occurring around 200 MPa for both samples (CR + 300°C 10m and CR + 400°C 10m) should stem from SIMT. However, this explanation still cannot account for why the modulus was low before that point. Other published studies [8,12] have also observed a similar double-yielding phenomenon. After low-temperature aging for 10 minutes, the actual yield strength of CR + 300°C 10m and CR + 400°C 10m increased by 75 MPa and 150 MPa, respectively, with no significant loss of elongation-to-failure values.

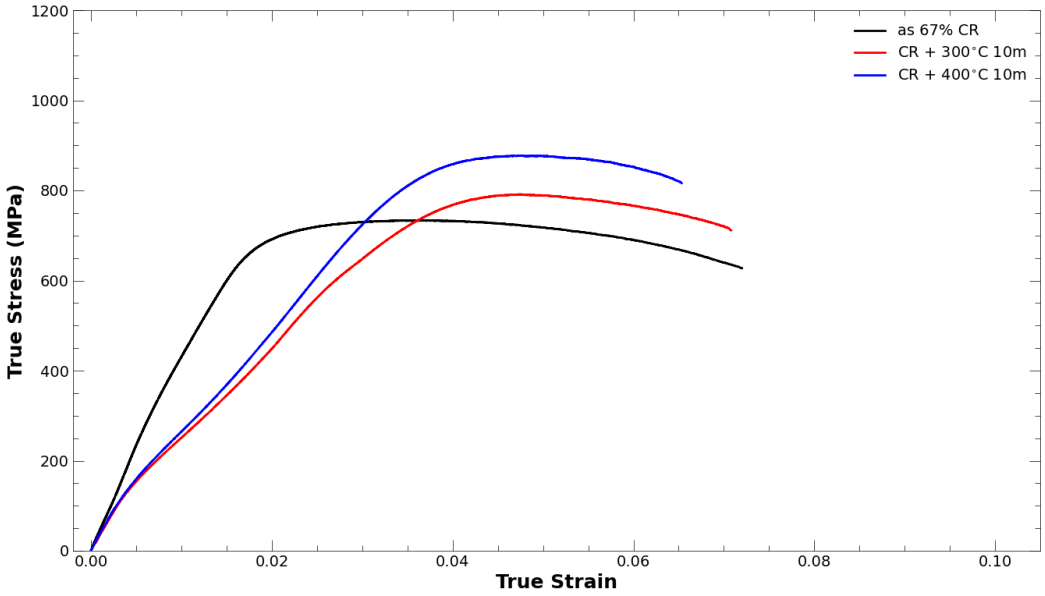

Figure 25*: Tensile performance of Ti-25Nb (at%) at three thermo-mechanical treatment conditions: as 67% cold rolled; with additional heat treatment at 300°C or 400°C for 10 minutes followed by water quench.*

However, low-temperature aging is not the only factor that affects the reduction of elastic modulus. **Figure 26** shows that aging for a slightly longer time at 300°C (CR + 300°C 20m) leads to an even lower elastic modulus of 27.3 GPa, with an even higher yield strength and similar elongation-to-failure compared to CR + 300°C 10m. However, the degree of the S-shaped curvature is less pronounced in CR + 300°C 20m. Conversely, prolonging the heat treatment time has the opposite effect, with CR + 300°C 1hr displaying a modulus of 50.2 GPa. The process window for modulus reduction is even narrower in the case of 400°C aging, as shown in **Figure 27**. A 20-minute heat treatment at 400°C slightly increases the modulus of the sample (CR + 400°C 20m) by 7 GPa compared to a 10-minute heat treatment, with a slight strength increase and a significant reduction in elongation-to-failure by 20%. Further aging at 400°C only makes the

material stiffer, stronger, and much more brittle. Aging for 24 hours at both 300°C and 400°C has a detrimental effect on samples, resulting in almost no plastic deformation capability.

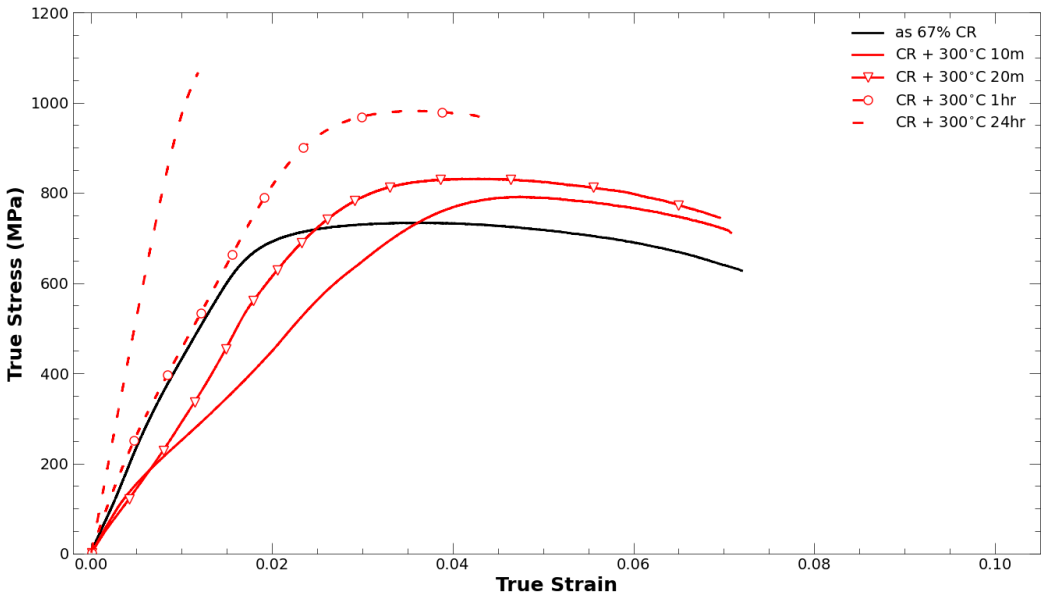

***Figure 26**: Tensile performance comparison of Ti-25Nb (at%) with various heat treatment time at 300°C.*

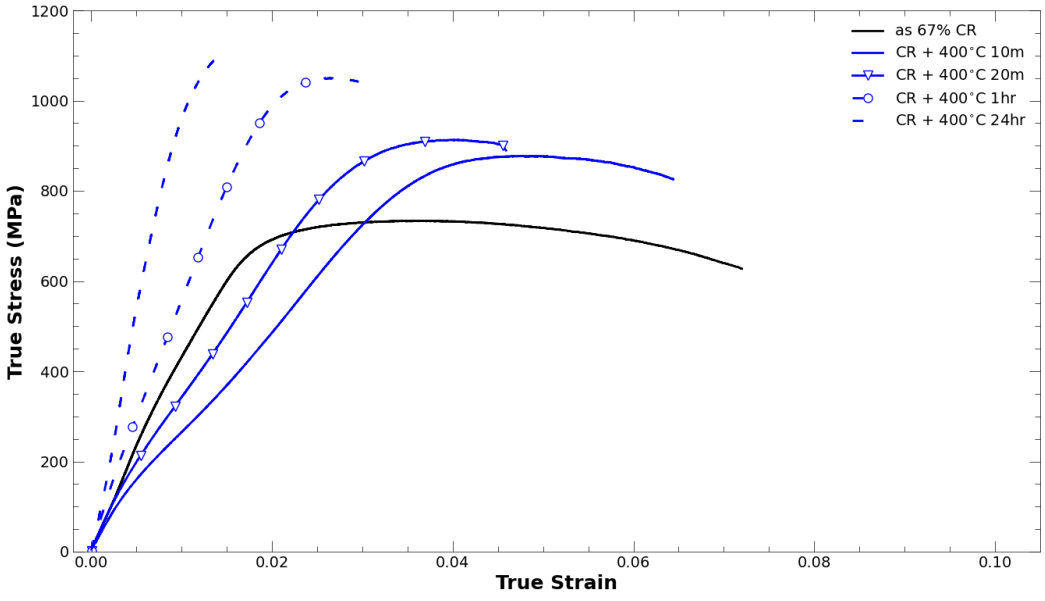

***Figure 27**: Tensile performance comparison of Ti-25Nb (at%) with various heat treatment time at 400°C.*

According to Kim et al. [9], the thermal ω phase can precipitate within the β matrix during low-temperature aging. These ω precipitates can significantly strengthen the material, but they have the severe side-effect of reducing ductility. The ω phase transformation temperature is typically considered to be 550°C in β Ti alloys [13]. Based on Kim et al.'s studies, the kinetics of ω phase formation is suppressed when it is above 500°C, and the ω phase reverts back to the β phase at 600°C. **Figure 28** confirms this observation. Both CR + 500°C 10m and CR + 600°C 10m samples exhibit lower strengths compared to as 67% CR, indicating less ω content within these samples. The elongation-to-failure values of these two samples also improved due to additional strain recovery and recrystallization at elevated temperature. Interestingly, the elastic moduli of CR + 500°C 10m and CR + 600°C 10m are close to as 67% CR, with values of 41 GPa and 47 GPa, respectively. A 500°C heat treatment for 10 minutes appears to have a slight modulus reduction effect as well. Noted that ω can still be formed in the β phase at this temperature. Combining the observations from the results so far, it can be concluded that the modulus reduction phenomenon in Ti-25Nb (at%) is closely related to the ω phase content.

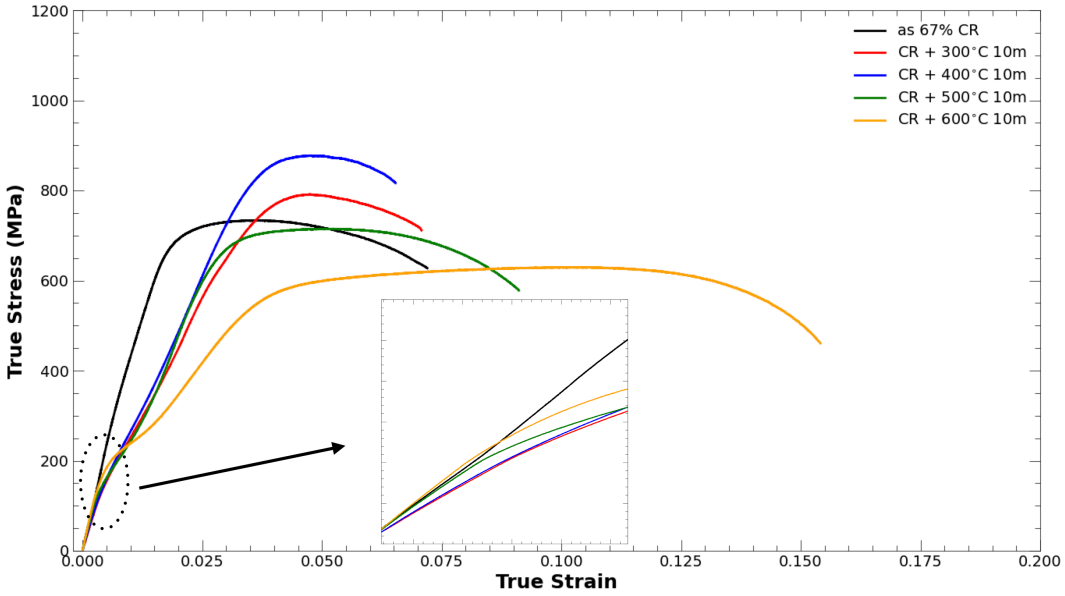

***Figure 28**: Tensile performance comparison of Ti-25Nb (at%) with 10 minutes of heat treatment time at various of temperature from 300°C to 600°C. The zoom-in view showing a close look of the initial elastic responses.*

To better demonstrate the influence of the ω phase and heat treatment conditions on the elastic modulus, a summary of the elastic modulus in relation to heat treatment conditions is presented in **Figure 29**. As observed, the elastic modulus is dependent on heat treatment duration and temperature. It should be noted that there is a temperature threshold related to the ω phase transformation, which occurs at approximately 550°C. Above this temperature, the ω phase is eliminated, and the elastic modulus remains relatively constant.

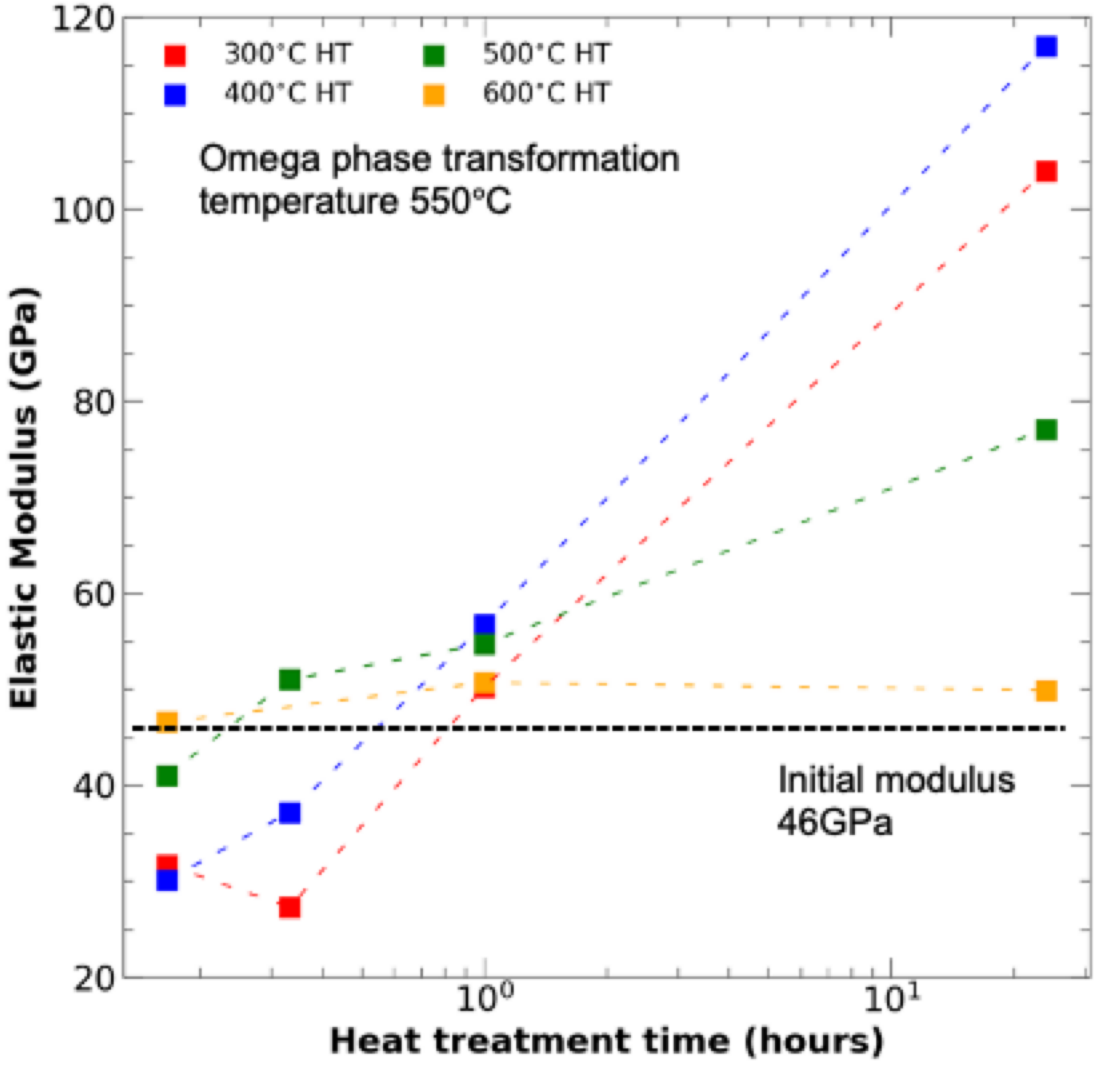

***Figure 29**: Summary of elastic modulus versus heat treatment conditions based on the tensile experiments. Tensile responses that are not shown previously are provided in the appendix.*

Below the ω phase transformation temperature of 550°C, the effects of heat treatment become more complex. While it is reasonable to assume that a higher ω content corresponds to a higher elastic modulus above a certain threshold, introducing a small amount of ω content below that threshold can actually contribute to a reduction in the elastic modulus, which is counter to

published studies. Based on the current data, there may be an optimal heat treatment condition for achieving minimum elastic modulus, similar to peak aging, which refers to the maximum improvement in strength or hardness. However, the specific threshold or required microstructure remains unclear. For instance, at 500°C, the ω phase formation rate should be the lowest, given that the CR + 500°C 24hr sample has a much lower modulus than the CR + 300°C 24hr or CR + 400°C 24hr samples. Consequently, the CR + 500°C 10m sample should have a lower ω phase content than the 300°C 10m or CR + 400°C 10m samples. However, the CR + 500°C 10m sample does not exhibit a lower modulus, suggesting that the relationship between ω content and elastic modulus is more complex than previously thought.

To further understand the mechanism of modulus reduction, tensile experiments with in-situ synchrotron 2θ XRD were performed. **Figure 30** summarizes the 1D XRD spectra of 67% CR and CR + 300°C 10m samples at various engineering strains up to 1%. Based on the XRD spectra, the 67% CR sample contained a significant amount of α''phase, as the intensity of the $(020)_{\alpha''}$ crystal plane was nearly the same as the $(110)_{\beta}$ plane. It should be noted that both the β and α''phases of the 67% CR sample were under a considerable amount of internal strain due to cold-rolled state, with d-spacing values of 0.2302 nm for the $(110)_{\beta}$ plane and 0.2385 nm for the $(020)_{\alpha''}$ plane. For comparison, the theoretical d-spacing values for the $(110)_{\beta}$ and $(020)_{\alpha''}$planes are 0.232 nm and 0.237 nm, respectively [9]. At 1% strain, the d-spacing values for the $(110)_{\beta}$ and $(020)_{\alpha''}$planes further shifted to 0.2298 nm and 0.2400 nm, respectively. Aside from peak shifting, no major structural changes were observed in the 67% CR sample.

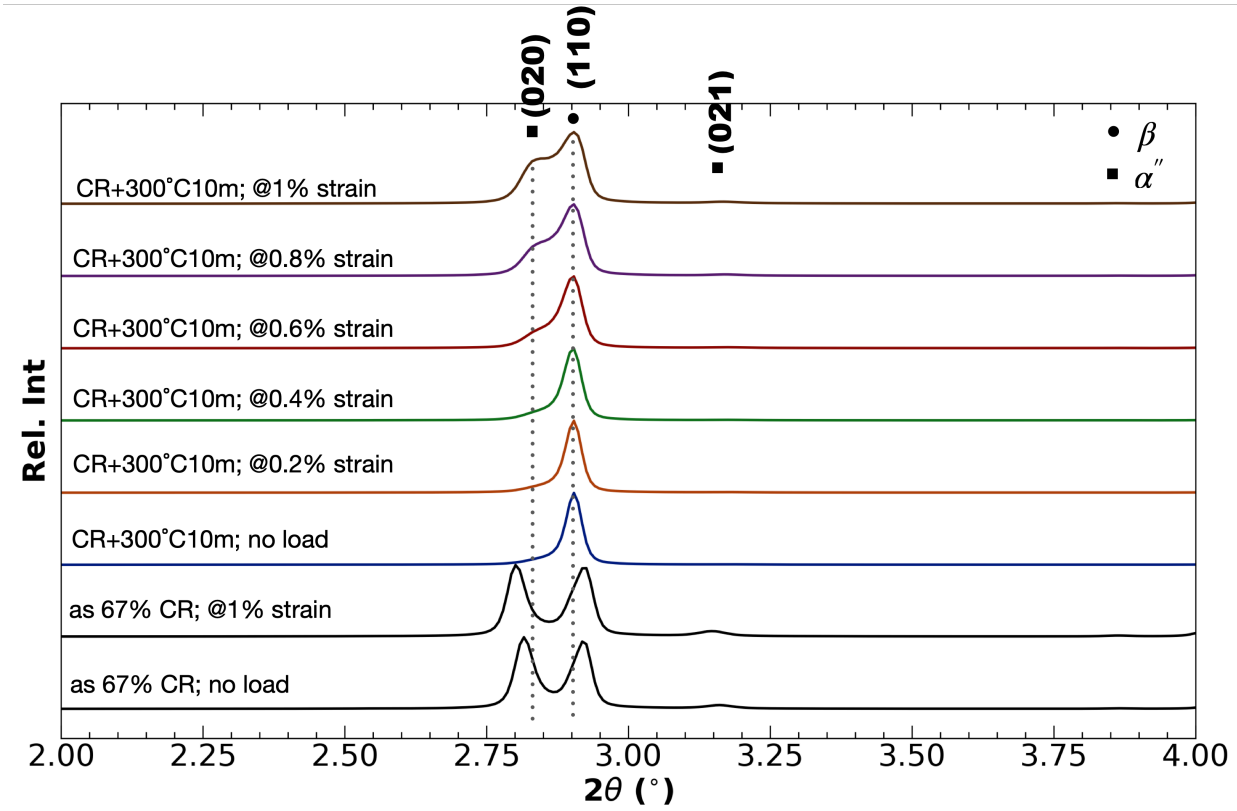

***Figure 30**: 1D XRD spectra generated by in-situ synchrotron 2 θ XRD during tensile experiments of as 67% CR and CR + 300°C 10m. The samples were loaded up to 1% of engineering strain and 2D XRD patterns were captured simultaneously. The 2D XRD patterns were then converted to 1D spectra for better illustration.*

In contrast, the heat treatment eliminated the α'' phase, as the CR + 300°C 10m sample exhibited no α'' peaks in its spectrum. Furthermore, the d-spacing of the $(110)_\beta$ plane was 0.2314 nm, much closer to the theoretical value, indicating that strain relief occurred. As strain increased, an additional peak appeared to the left of the $(110)_\beta$ plane, identified as the $(020)_{\alpha''}$ plane with a d-spacing of 0.2371 nm, suggesting the emergence of SIMT. Intriguingly, the d-spacing values of both the $(110)_\beta$ and $(020)_{\alpha''}$planes remained unchanged as strain increased, implying that internal strain was entirely compensated for by the formation of the α''' phase via SIMT. Regrettably, due to experimental setup limitations, the ω phase could not be detected. Therefore,

current data is still insufficient to support that ω phase played an active role in the initial modulus reduction.

2.4. Conclusions

In this study, a series of tensile experiments were conducted on Ti-25Nb (at%) samples subjected to various thermo-mechanical treatments. Several critical findings emerged:

- Ti-25Nb (at%) can obtain ultralow modulus, below 30GPa, through severe cold rolling followed by short-duration, low-temperature aging.
- The in-situ synchrotron loading experiments suggest that the ultralow modulus arises from SIMT.
- The ω phase is found to play a critical role in achieving the ultralow modulus. This challenges the typical impression about the impact of the ω phase on mechanical performance in β Ti alloys found in the literature.
- However, the optimal microstructure for achieving the lowest stress for initiating SIMT and obtaining the lowest apparent elastic modulus at near zero external stress remains unclear.

2.5.References

[1] L.-C. Zhang, L.-Y. Chen, A Review on Biomedical Titanium Alloys: Recent Progress and Prospect, Adv. Eng. Mater. 21 (2019) 1801215. https://doi.org/10.1002/ADEM.201801215.

[2] M. Long, H.J. Rack, Titanium alloys in total joint replacement--A materials science perspective., Biomaterials. 19 (1998) 1621–39. https://doi.org/10.1016/S0142-9612(97)00146-4.

[3] M.I.Z. Ridzwan, S. Shuib, A.Y. Hassan, A.A. Shokri, M.N. Mohamad Ibrahim, Problem of Stress Shielding and Improvement to the Hip Implant Designs: A Review, J. Med. Sci. 7 (2007) 460–467. https://doi.org/10.3923/jms.2007.460.467.

[4] S. Bahl, S. Suwas, K. Chatterjee, Comprehensive review on alloy design, processing, and performance of β Titanium alloys as biomedical materials, Https://Doi.Org/10.1080/09506608.2020.1735829. 66 (2020) 114–139. https://doi.org/10.1080/09506608.2020.1735829.

[5] M. Tane, S. Akita, T. Nakano, K. Hagihara, Y. Umakoshi, M. Niinomi, H. Nakajima, Peculiar elastic behavior of Ti–Nb–Ta–Zr single crystals, Acta Mater. 56 (2008) 2856–2863. https://doi.org/https://doi.org/10.1016/j.actamat.2008.02.017.

[6] H.Y. Kim, L. Wei, S. Kobayashi, M. Tahara, S. Miyazaki, Nanodomain structure and its effect on abnormal thermal expansion behavior of a Ti-23Nb-2Zr-0.7Ta-1.2O alloy, Acta Mater. 61 (2013) 4874–4886. https://doi.org/10.1016/j.actamat.2013.04.060.

[7] J. Ma, I. Karaman, R.D. Noebe, High temperature shape memory alloys, Int. Mater. Rev. 55 (2010) 257–315. https://doi.org/10.1179/095066010X12646898728363.

[8] S. Miyazaki, My Experience with Ti–Ni-Based and Ti-Based Shape Memory Alloys, Shape Mem. Superelasticity. 3 (2017) 279–314. https://doi.org/10.1007/s40830-017-0122-3.

[9] H.Y.Y. Kim, Y. Ikehara, J.I.I. Kim, H. Hosoda, S. Miyazaki, Martensitic transformation, shape memory effect and superelasticity of Ti–Nb binary alloys, Acta Mater. 54 (2006) 2419–2429. https://doi.org/10.1016/j.actamat.2006.01.019.

[10] T. Inamura, J.I. Kim, H.Y. Kim, H. Hosoda, K. Wakashima, S. Miyazaki, Composition dependent crystallography of α″-martensite in Ti-Nb-based β-titanium alloy, Philos. Mag. 87 (2007). https://doi.org/10.1080/14786430601003874.

[11] A.P. Hammersley, {\it FIT2D}: a multi-purpose data reduction, analysis and visualization program, J. Appl. Crystallogr. 49 (2016) 646–652. https://doi.org/10.1107/S1600576716000455.

[12] Y.W. Chai, H.Y. Kim, H. Hosoda, S. Miyazaki, Self-accommodation in Ti-Nb shape memory alloys, Acta Mater. 57 (2009) 4054–4064. https://doi.org/10.1016/j.actamat.2009.04.051.

[13] S. Banerjee, R. Tewari, G.K. Dey, Omega phase transformation - Morphologies and mechanisms, Int. J. Mater. Res. 97 (2006) 963–977. https://doi.org/10.3139/146.101327.

2.6. Appendix

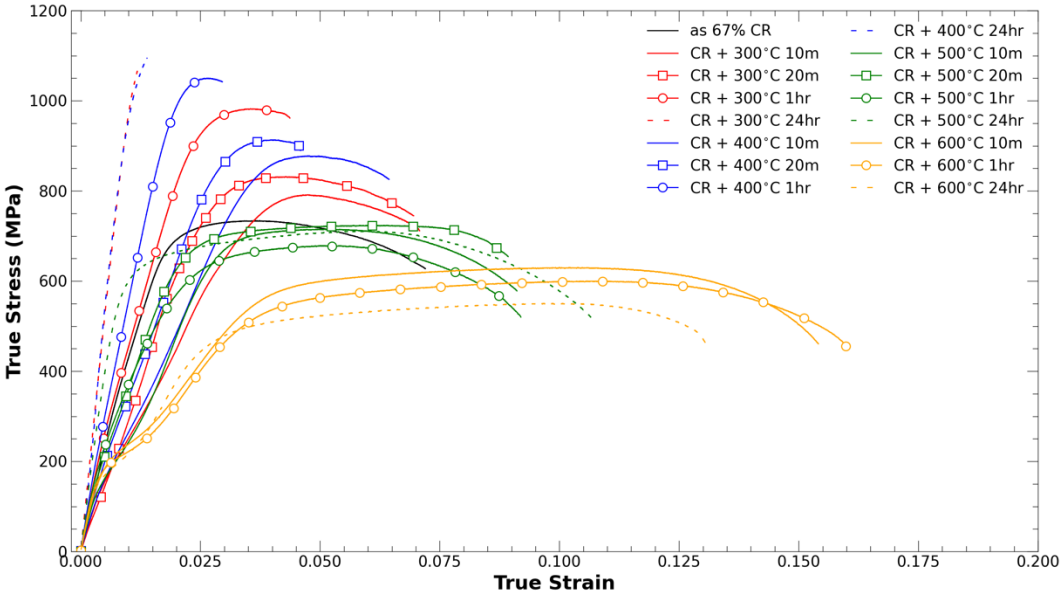

***Figure 31**: Tensile performance of Ti-25Nb (at%) samples after various of thermo-mechanical treatments.*

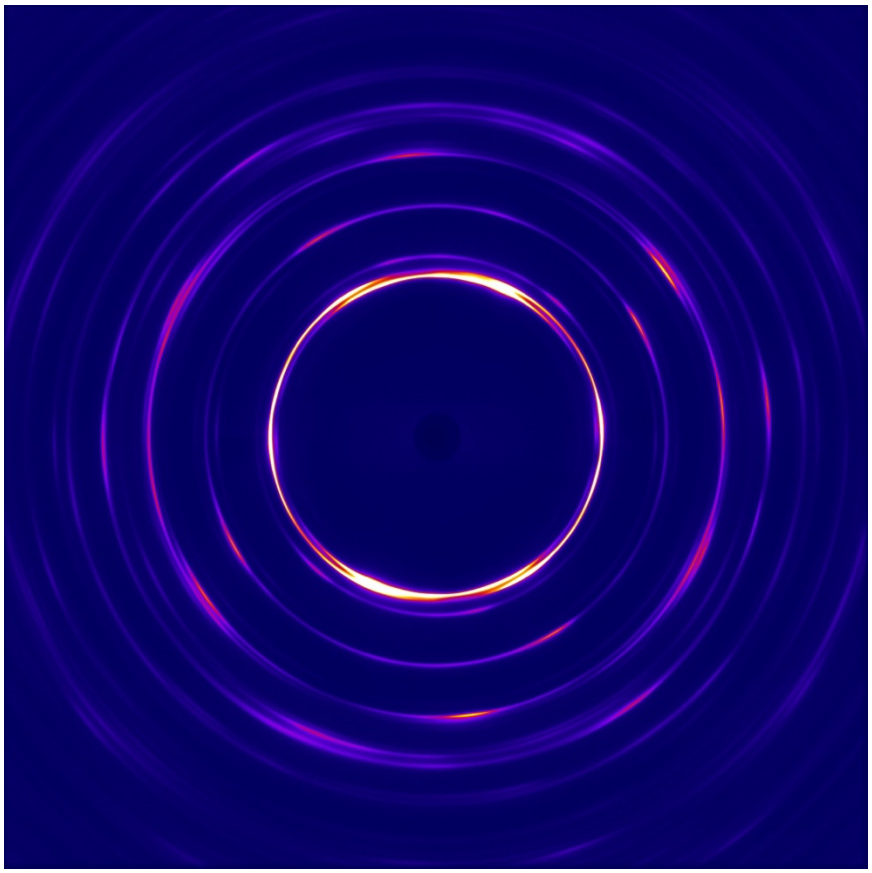

***Figure 32**: 2D Synchrotron X-ray diffraction pattern of as 67% CR at no load condition.*

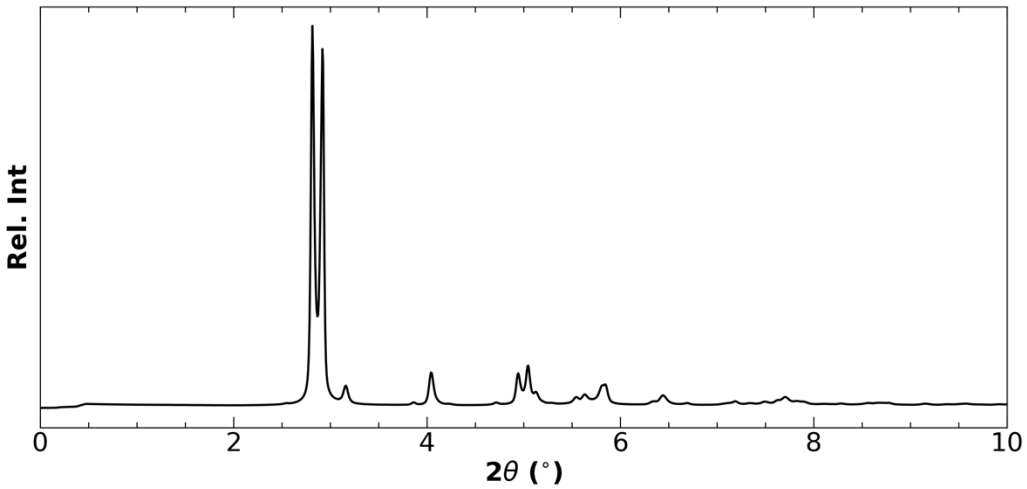

***Figure 33**: 1D Synchrotron X-ray diffraction spectrum of as 67% CR at no load condition.*

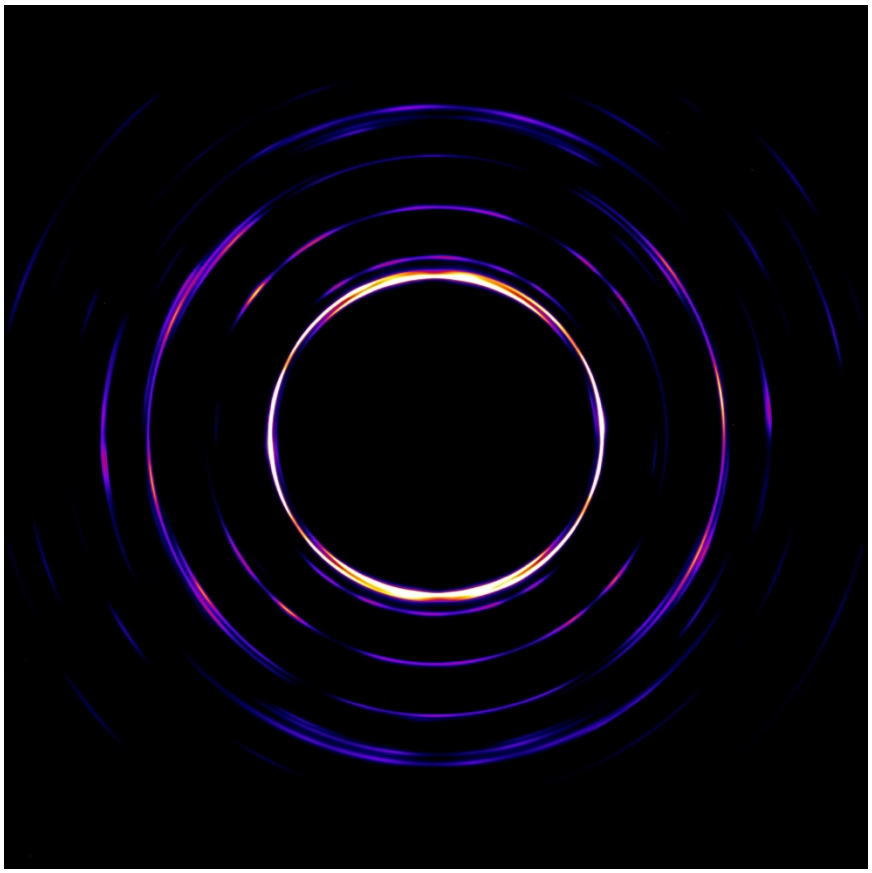

***Figure 34**: 2D Synchrotron X-ray diffraction pattern of as 67% CR at 1% strain.*

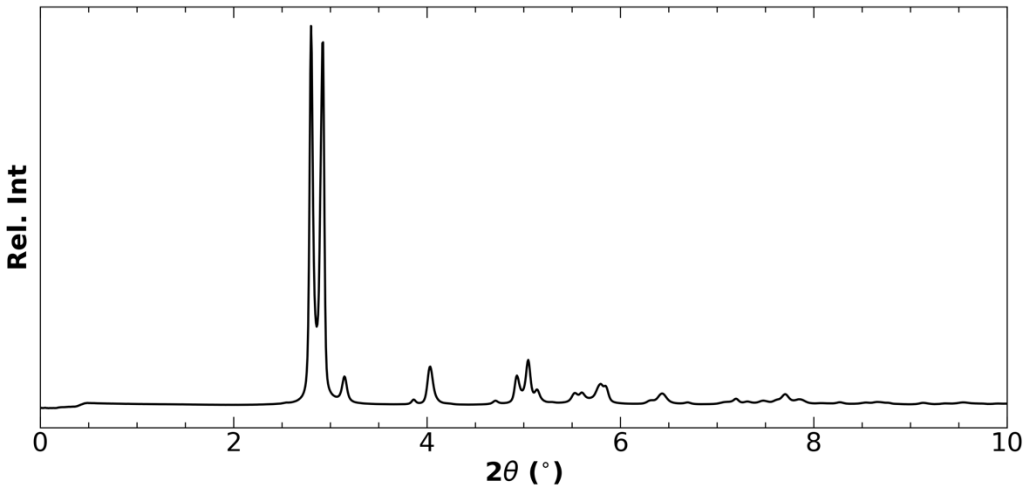

***Figure 35**: 1D Synchrotron X-ray diffraction spectrum of as 67% CR at 1% strain.*

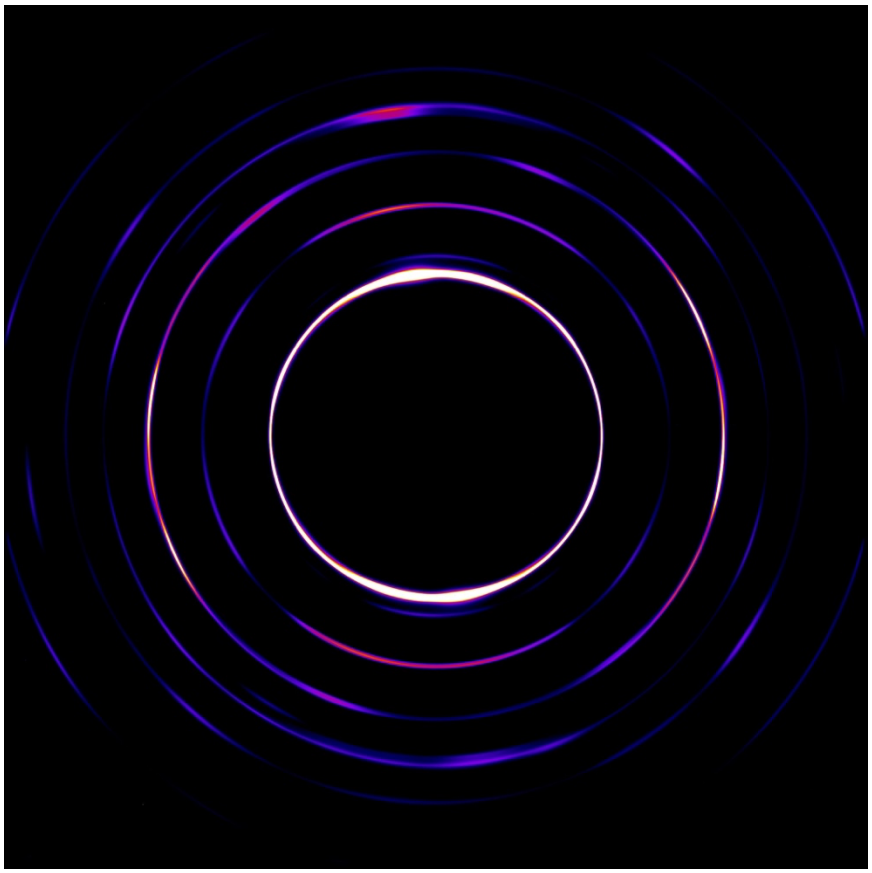

***Figure 36**: 2D Synchrotron X-ray diffraction pattern of CR + 300°C 10m at no load condition.*

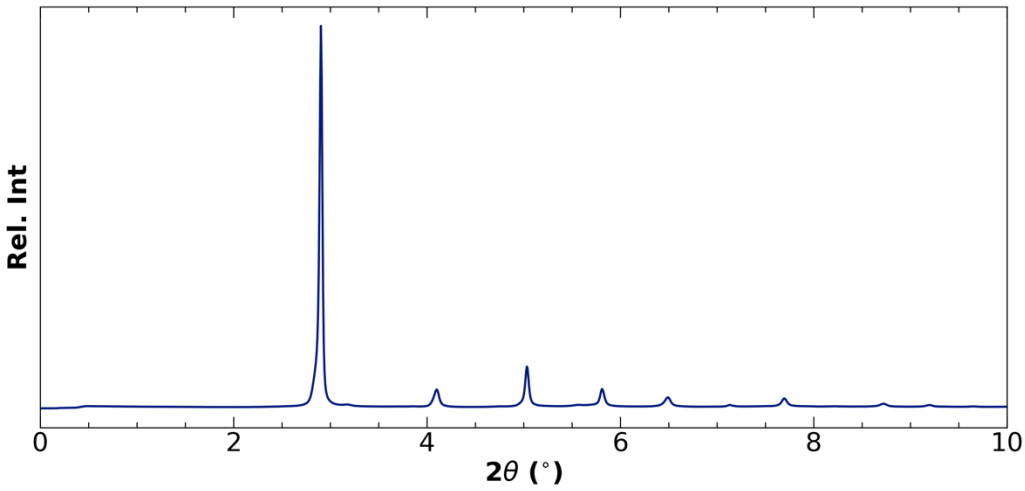

***Figure 37**: 1D Synchrotron X-ray diffraction spectrum of CR + 300°C 10m at no load condition.*

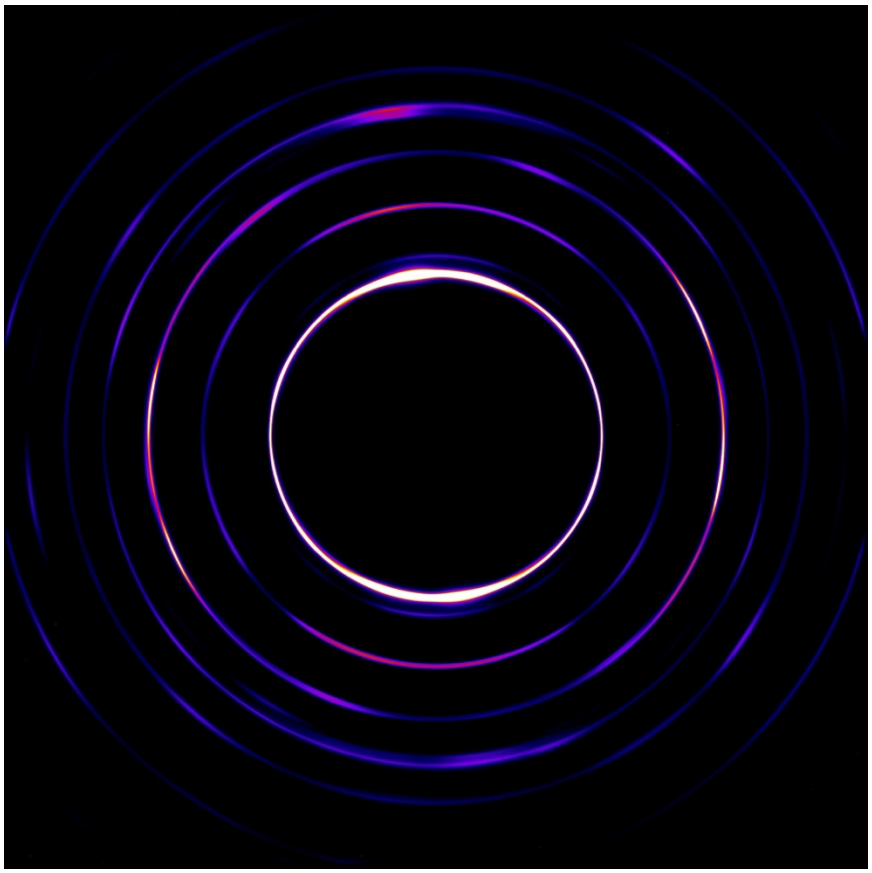

***Figure 38**: 2D Synchrotron X-ray diffraction pattern of CR + 300°C 10m at 1% strain.*

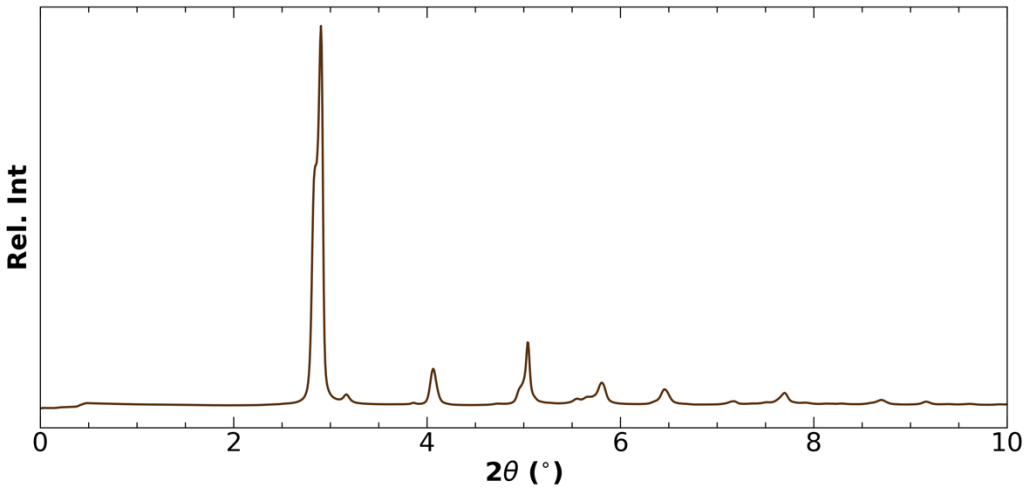

***Figure 39**: 1D Synchrotron X-ray diffraction spectrum of CR + 300°C 10m at 1% strain.*

3. Novel Metastable Microstructure in Laser Processed Ti-Nb Alloys

3.1. Introduction

Laser metal additive manufacturing (AM) methods such as laser powder bed fusion (L-PBF) and laser direct energy deposition (L-DED) have received significant attention from industry as well as academic researchers. These methods not only simplify the fabrication of intricate geometries but also potentially can enhance material properties due to the unique thermomechanical history [1–3]. During the AM process, materials can experience high heating/cooling rates during multiple melting/remelting and solidification cycles as well as continuous residual heating during the entire build [1,4]. As a result, novel and hierarchical microstructures can be introduced. For example, chemical microsegregation at inter-cellular/dendritic boundaries can be controlled to create precipitation of second phases, further improving material strength [5,6]. However, unregulated precipitate formation may produce inferior properties due to embrittlement [7]. Unique dislocation networks rooted along the cellular boundaries can be found in various additive manufactured metals such as 316L stainless steel [8]. These continuous entangled dislocation networks that can slow down instead of blocking dislocation motion which facilities methods for simultaneous improvement in strength and ductility [8–10].

Metastable β titanium (Ti) alloys have been recognized as excellent biomaterials, especially for orthopedic implants. Compared to conventional bio-structural metals such as stainless steel, Ti-6Al-4V, or cobalt-chrome, metastable β-Ti alloys possess elastic moduli that are much closer to ones of human bones, while maintaining high strength, high corrosion resistance, and good biocompatibility [11]. As device manufacturers adopt AM as a production technique, it is important to examine the effect of AM processing on the performance these bio-structural metals,

including metastable beta-Ti alloys. More importantly, a more extensive understanding of the as-printed microstructure is needed in order to minimize the effects in post-processing to reduce cost as well as retain the unique material properties in as-AM conditions.

Metastable β-Ti alloys are primarily body-centered cubic (BCC) phase but may contain other phases such as hexagonal α' or orthorhombic α'' phase as well as hexagonal ω phase [12]. However, according to our previous study, the laser processed metastable β-Ti alloys can have unexpected microstructural changes [13], for example an orthorhombic lattice distortion inside of cellular regions after rapid solidification. As a result, the lattice structure within these regions is neither BCC nor a well-known metastable phase like α'' phase. Additionally, lattice distortion strains up to 8% along one of the $< 001 >_\beta$ directions were observed. Surprisingly, based on the bright field (BF) as well as the dark field (DF) of transmission electron microscopy (TEM) images, no sign of dense dislocation networks often found in other alloys fabricated through LPBF is observed. It is known that the parent β phase can initiate phase transformations to other metastable phases in response to internal stresses. For example, alloys with a certain range of β stabilizer composition can undergo the martensitic transformation from β to α'' during the mechanical loading [14]. This phase transformation can be achieved via a partial $\{211\} < \bar{1}\bar{1}1 >_\beta$ shear and $\{011\} < 0\bar{1}1 >_\beta$ shuffle [15]. It is also reported that another metastable phase, ω, can also form to accommodate internal strains induced during the reversed martensitic transformation [16]. We hypothesize that the metastable Ti-Nb alloys may prefer transforming to metastable phases during the rapid solidification instead of forming dislocations in response to the significant thermal strains generated during rapid solidification. Currently, few studies have been published to understand the phase structure of rapidly solidified metastable β-Ti alloys.

Second, the distorted regions reported in our previous study have extra superlattice reflections in their diffraction patterns at some zone axes. In theory, these reflections are forbidden in the parent β phase as well as in α'' phase. However, there was insufficient evidence at the time to exclude the cases that reflections might come from dynamic diffraction inside of α'' phase. In other words, the distorted regions can potentially still share the same Cmcm space group as the α'' phase even though the lattice parameters of this structure are different from the ones of α'' phase reported in the literature. On the other hand, another possibility is that such superlattice reflections might belong to a different metastable phase. In recent years, β-Ti gum metals are revealed to have an additional plastic deformation mechanism known as lattice modulation [17]. This lattice modulation results in the growth of nanoscale martensite-like nanodomains which are believed to be associated with excellent cold-workability and the invar-like behavior in these metals [15,17]. These nanodomains, also known as O' phase, are formed by the lattice modulation along $\{011\} < 0\bar{1}1 >_\beta$ due to the introduction of small interstitial atoms like oxygen atoms into the BCC octahedral interstitial sites [18,19]. Kim et al. reported that such domain structures can suppress long-range martensitic transformation [17]. Consider O' phase is usually reported in heavily deformed materials, it is expected to find O' inside the additive manufactured metastable β-Ti alloys because of the significant internal stress generated during the rapid solidification.

In this study, we investigate the microstructure of laser-processed metastable β titanium-niobium (Ti-25at%Nb) shape memory alloys (SMAs) in detail through electron microscopy with the primary goals: 1) Understand the origin of lattice distortion inside the cellular region; 2) Fully characterize the microstructure (including all metastable phases) in laser-processed TiNb.

3.2. Methods

Ti-25Nb (at%) billet produced by vacuum arc melting was solution heated at 900℃ for 2 hrs in an Argon atmosphere and water quenched. This alloy after solution heated displays a mixture of β and α'' phases according to the x-ray diffraction results in the previous study[13], shown in **Figure 40** D). A 10 mm x 10 mm x 2 mm square sample was cut from the billet and mechanically polished. An SLM 125 (SLM Solutions NA, Inc.) laser powder bed fusion system was used to perform a single layer scan with 225 W laser power, 800 mm/s scanning speed, and 120 μm of hatch distance. Such scan is almost covered entire 10 mm x 10 mm area with roughly around 250-300 μm penetration. The process chamber was held below 1000 ppm oxygen using ultrahigh purity Argon gas during the process.

The laser-processed substrate was perpendicularly cross-sectioned to the scanning direction for focus ion beam (FIB) lift-out. The sample was mounted in the epoxy and mechanically polished up to 0.05 nm collide silica. In order to improve imaging, it was etched with 2%vol hydrofluoric acid and 6%vol nitric acid mix (balanced distilled water). Two TEM samples were fabricated by FIB processing using a Helios UC G4 dual beam system (Thermo Fisher Scientific): 1) Ti25Nb-A was sliced from the end of the melt pool (MP) array while 2) Ti25Nb-B was sliced from the beginning of the MP array, shown in ***Figure 40*** B). The difference between Ti25Nb-A and Ti25Nb-B is that the latter one received additional remelting/reheating. The TEM and scanning TEM (STEM) experiments were performed on a Themis Z 60-300 kV TEM/STEM system (Thermo Fisher Scientific). The 4D STEM is conducted using the Gatan 4D STEM module. When the probe dwells at a pixel position, the corresponding CBED pattern of the pixel is recorded. The data set is processed using a custom Python code with the implementation of the HyperSpy toolbox [20].

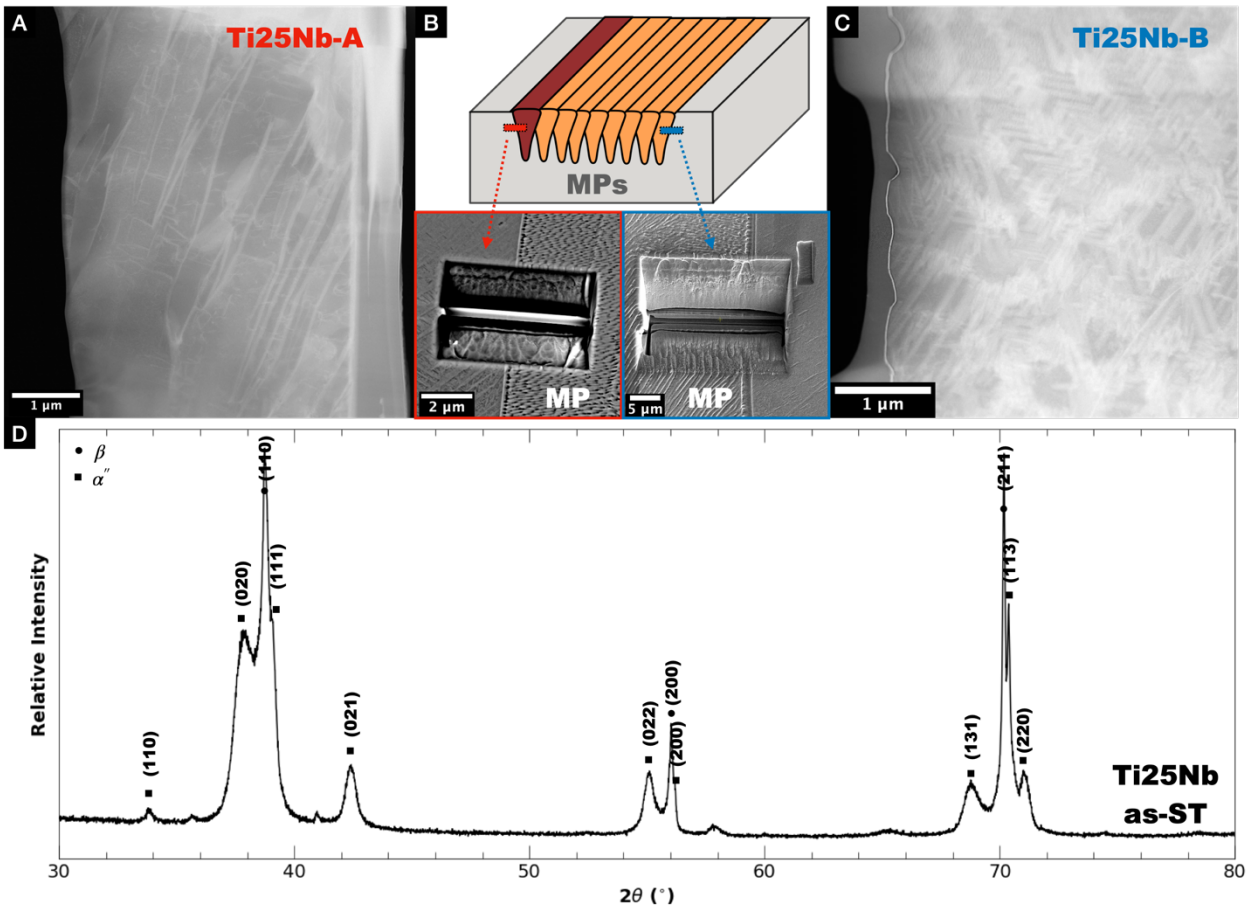

***Figure 40**: A) & C) STEM DF images of Ti25Nb-A and Ti25Nb-B. B) A schematics of the MP array. The red and blue boxes indicate the locations where Ti25Nb-A and Ti25Nb-B were fabricated from FIB. Two corresponding post-FIB SEM images are also shown above. Notice that Ti25Nb-A received neither remelting or reheating since the far-left melt pool is the last one formed in the process. D) X-ray diffraction (XRD) pattern of Ti25Nb at as solution treated condition [13].*

3.3. Results

The STEM dark field (DF) images of Ti25Nb-A and Ti25Nb-B are shown in **Figure 40** A) & C). The morphology of Ti25Nb-A consists of numerous darker elongated cellular structures, separated by bright boundaries. These elongated structures are roughly parallel, but the shape and size of these structures are quite inconsistent. Some of them are much narrower (less than 100 nm) and some of them are wavier than others. Another observation is that the dislocations in Ti25Nb-

A can be observed but there is no evidence of a high-density network occurring in the intercellular regions as in other AM materials such as 316L stainless steel. A zoom-in view can be found in **Figure 41** A). Interestingly, the morphology of Ti25Nb-B is quite different from that of Ti25Nb-A, as it is shown in **Figure 40** C). Instead of long cellular structures, there are shorter elongated plates in bright intensity that are arranged in several different orientations. In addition, on contrast to highly visible cellular boundaries in Ti25Nb-A, ones in Ti25Nb-B are relatively faint in STEM image despite the post-FIB SEM image clearly displaying those boundaries.

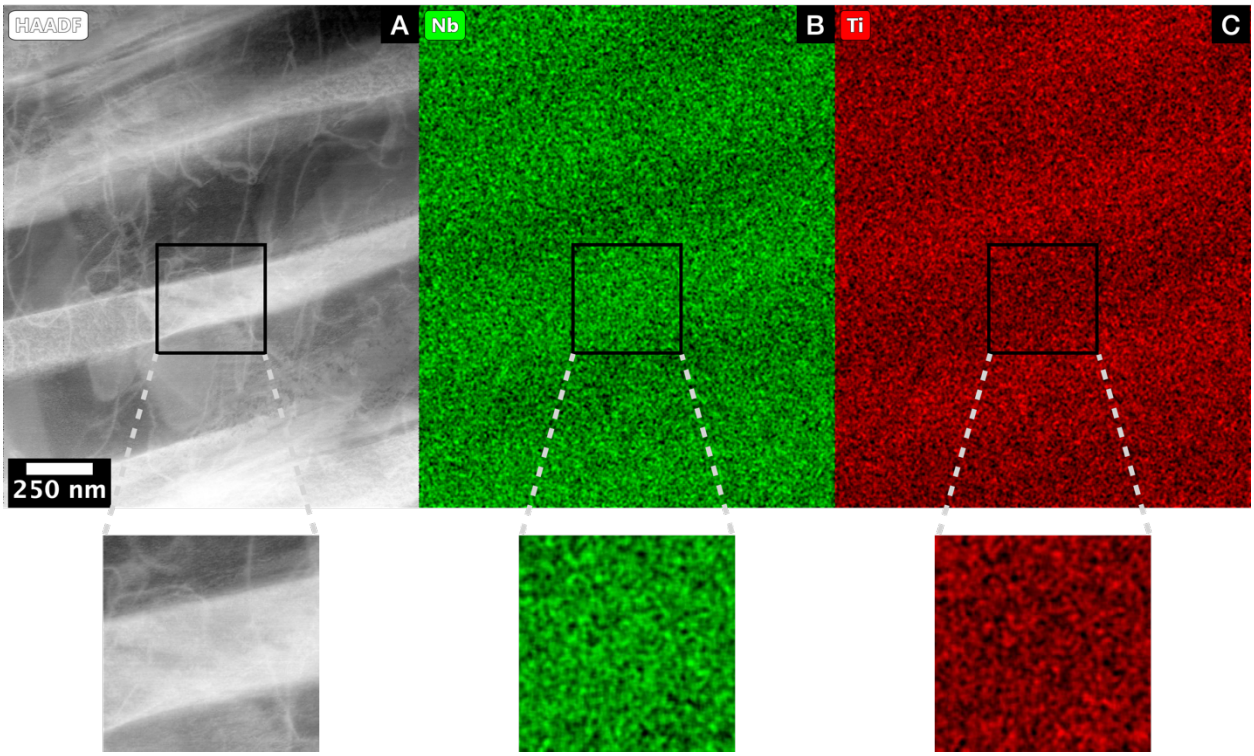

***Figure 41**: STEM EDS mapping on an area of interest in the Ti25Nb-A sample. A), B) & C) HAADF image, Nb, and Ti elemental mapping. An Nb-rich region is marked by a square box with corresponding zoom-in views provided below.*

3.3.1. The microstructure of metastable Ti25Nb after rapid solidification

The elemental mapping of Ti25Nb-A was conducted using energy-dispersive X-ray spectroscopy (EDS) in STEM mode, shown in **Figure 41**. The contrast observed through high-angle annular dark-field (HAADF) image in **Figure 41** A), indicates the chemistry difference between neighboring features. Based on the Nb and Ti elemental mapping in **Figure 41** B) & C), the brighter features are Nb-rich while the darker features are Ti-rich. Interestingly, based on the contrast from the HAADF image it might imply there can be a quite significant elemental microsegregation occurring. However, the actual Nb segregation between cells and cellular boundaries is mild, fluctuating within a few at%.

Then the selected area electron diffraction (SAED) was carried out on the same region in Ti25Nb-A shown in **Figure 42**. The sample was tilted to one of the $< 311 >_{\beta}$ zone axis. To be consistent with our previous study [13], the zone axis is indexed as $[31\bar{1}]_{\beta}$ and the selected planes are also indexed accordingly. The diffraction pattern in the Nb-rich regions (marked as 1) is shown in **Figure 42** A). The Nb-lean region (marked as 2) has a different diffraction pattern, appearing as additional superlattice reflections, as seen in **Figure 42** B). Based on the conclusion from the previous study, the diffraction pattern in the Nb-lean region can be neither indexed as β phase nor α'' phase. To better visualize the difference, the 1D intensity profile (in log scale) vs. g is also plotted, shown in **Figure 42** D). The intensity values are calculated by integrating the brightness value of image pixels that have equal distances to the 000 spots in each diffraction pattern. Then to properly display the brightness of the peaks, the intensity values near the 000 spot are set to 0 and the rest of the intensity values are normalized. Within the same profile plot, the lines that represent the theoretical g values of selected β planes of Ti-25Nb(at%) are presented in blue color for reference. As it can be seen, the Nb-lean region exhibits more peaks as well as a more severe peak broadening effect. The d-spacing of the marked superlattice reflection from **Figure 42** C) is

measured as 0.283 nm which is larger than any of the theoretical d-spacing values in β phase and α'' phase, which are 0.232 nm and 0.266 nm, in Ti-25Nb (at.%)[14].

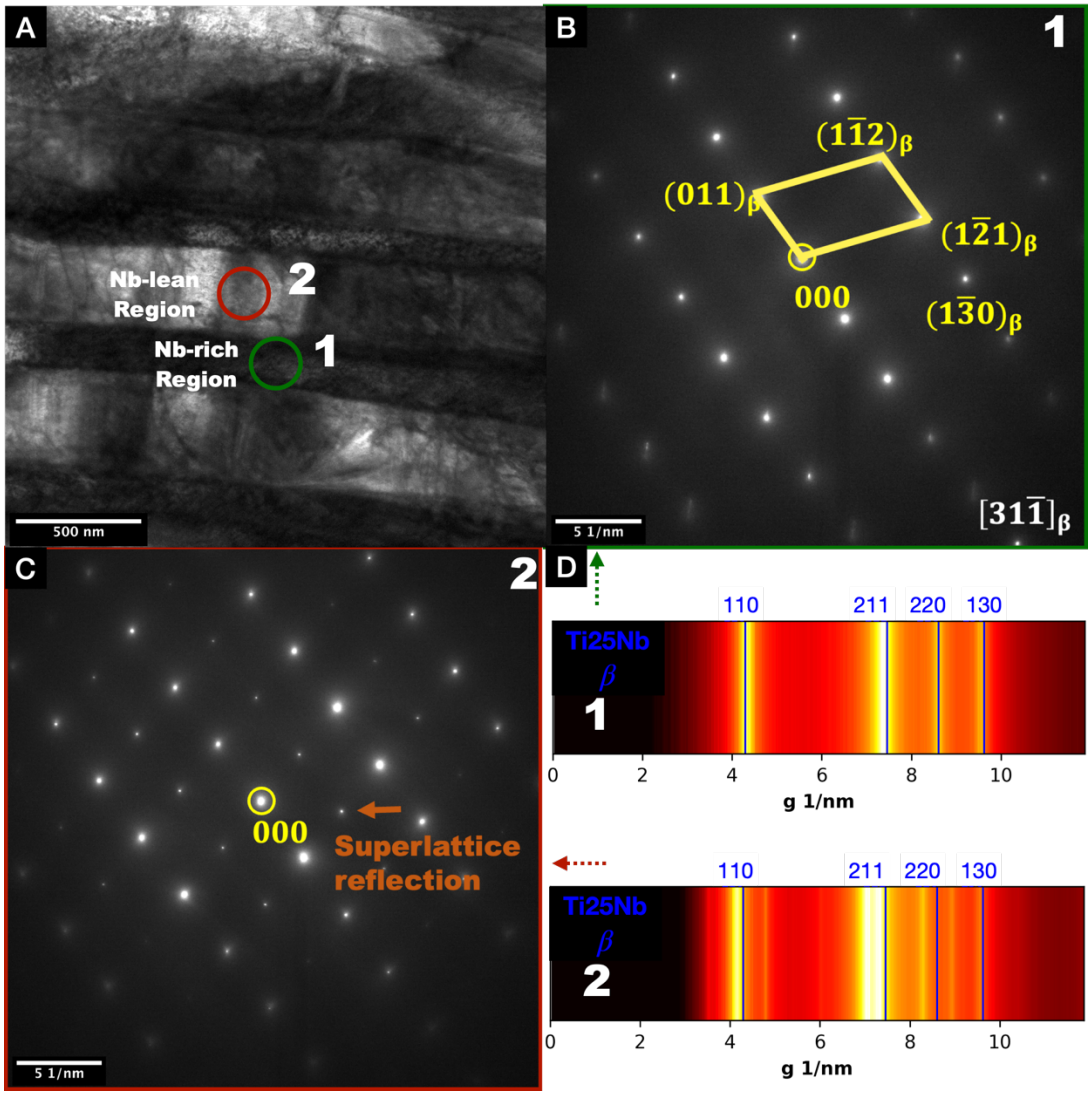

***Figure 42**: SAED patterns of selected regions on Ti25Nb-A sample. A) TEM bright field image with color coded boxes indicating the locations where SAED patterns were performed. The indexing number next to each box corresponds to the SAED pattern displayed in B) to C). The 000 spot is marked in each SAED pattern. D) 1D intensity profiles of diffraction pattern B) and C) (in log scale) vs. g are plotted by integrating the intensity of pixels that have the same distance to the 000 spots. In order to properly display the profile plot, the intensity values near the 000 spot are set to 0 and the rest of the intensity values are normalized. Within the same profile plot, the lines that represent the theoretical g values of selected β*

planes of Ti-25Nb(at%) are presented in blue color. B) The pattern is indexed as the diffraction pattern of β at $[31\bar{1}]_\beta$ zone axis. Selected lattice planes are indexed accordingly. C) The superlattice reflections are present, which is indicated by an arrow.

To better understand the structure inside the Nb-lean regions, high-res TEM (HRTEM) and STEM HAADF imaging were performed along the $[31\bar{1}]_\beta$ zone axis at the interface of Nb-rich/Nb-lean regions, shown in **Figure 43**. From **Figure 43** A)**,** numerous wavy sub-features are observed throughout the Nb-lean regions. These sub-features are few angstroms in width and tenths of nanometers in length. Such sub-features do not exist on the Nb-rich side. In addition, from the STEM HAADF image in **Figure 43** D), they are in dark contrast which indicate Ti enrichment. Furthermore, fast Fourier transformation (FFT) was performed on both the Nb-lean region and the Nb-lean region, indicated by red and green boxes in **Figure 43** A). The FFT pattern of the Nb-lean region is shown in **Figure 43** B) while the one from the Nb-rich region is shown in **Figure 43** C). Clearly, the superlattice reflections are present in the FFT pattern of the Nb-lean region (**Figure 42** B) but not in the Nb-rich region (**Figure 42** A). Since no dynamic diffraction effect can exist in the FFT patterns calculated from HRTEM images, the superlattice reflections should indeed originate from ordering or lattice distortion. This further strengthens that the Nb-lean region is not β phase nor α'' phase. Instead, it is an orthorhombic phase that has not been previously reported.

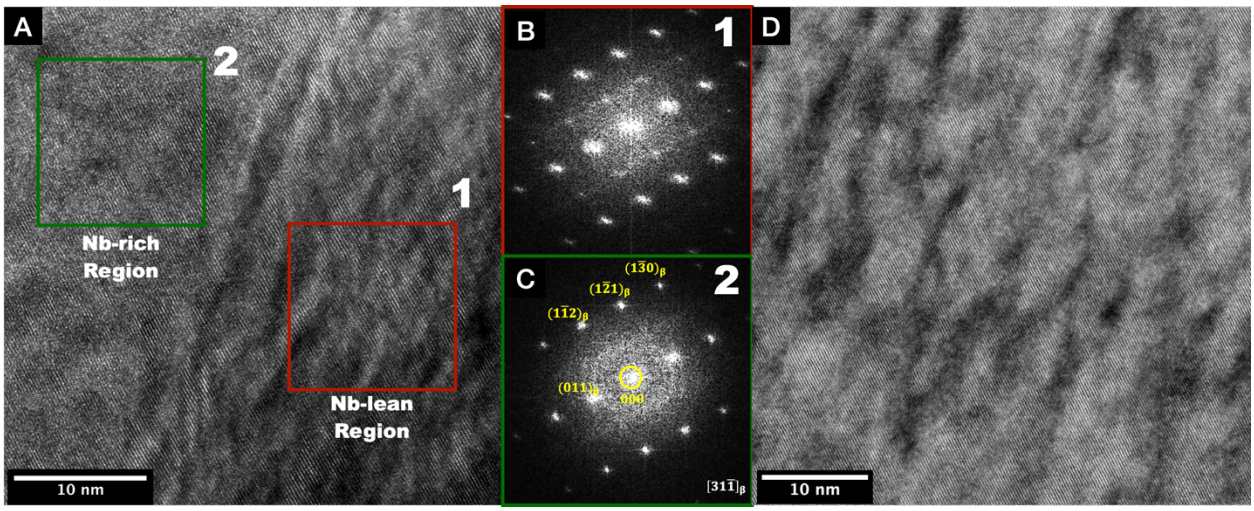

***Figure 43**: HRTEM image and STEM HAADF image on Ti25Nb-A sample at* $[31\bar{1}]_\beta$ *zone axis. A) HRTEM of an area of interest contains both Nb-rich and Nb-lean regions. A red box and a green box indicate the locations where the local FFTs are calculated in B) & C). B) FFT of Nb-lean region. The superlattice reflections can be seen in the FFT. C) FFT of Nb-rich region where no obvious superlattice reflection is observed. D) STEM HAADF image of the Nb-lean region. There are numerous darker wavy features can be observed.*

3.3.2. The microstructure of metastable AM Ti25Nb with additional remelting/reheating

Ti25Nb-B, on the other hand, has a dissimilar morphology to Ti25Nb-A, as shown in **Figure 44** A). No obvious solidification features such as cells or dendrites can be observed. Despite the appearance of a large number of elongated short plates throughout the sample, the crystal structure is surprisingly quite homogeneous, unlike Ti25Nb-A. Based on the diffraction patterns of Ti25Nb-B at various zone axes, the crystal structure of the lattice can be indexed as β phase, shown in **Figure 44** B) – D). No lattice distortion is found and the d-spacings of lattice planes are matched well with the theoretical g values. Unlike Ti25Nb-A, there are obvious signs of two types of metastable phases existing in diffraction patterns. First, the ω phase reflections appear in **Figure 44** C) & D). The signature of ω phase is the maximal intensities located at 1/3 or

2/3 position along one of the $< 112 >_\beta$ directions. Second, there are distinguishable maxima at the half position along the $< 011 >_\beta$ directions within the $[200]_\beta$ zone or the half position along the $< 112 >_\beta$ directions within the $[311]_\beta$ or $[110]_\beta$ zones. These maximal peaks represent the existence of *O'* phase which is extensively explained in the literature [15,17–19]. Consider *O'* phase, or nanodomains, is often reported in heavily deformed samples at the room temperature [17], this implies a significant amount of strains introduced during the laser melt and the subsequent solidification process.

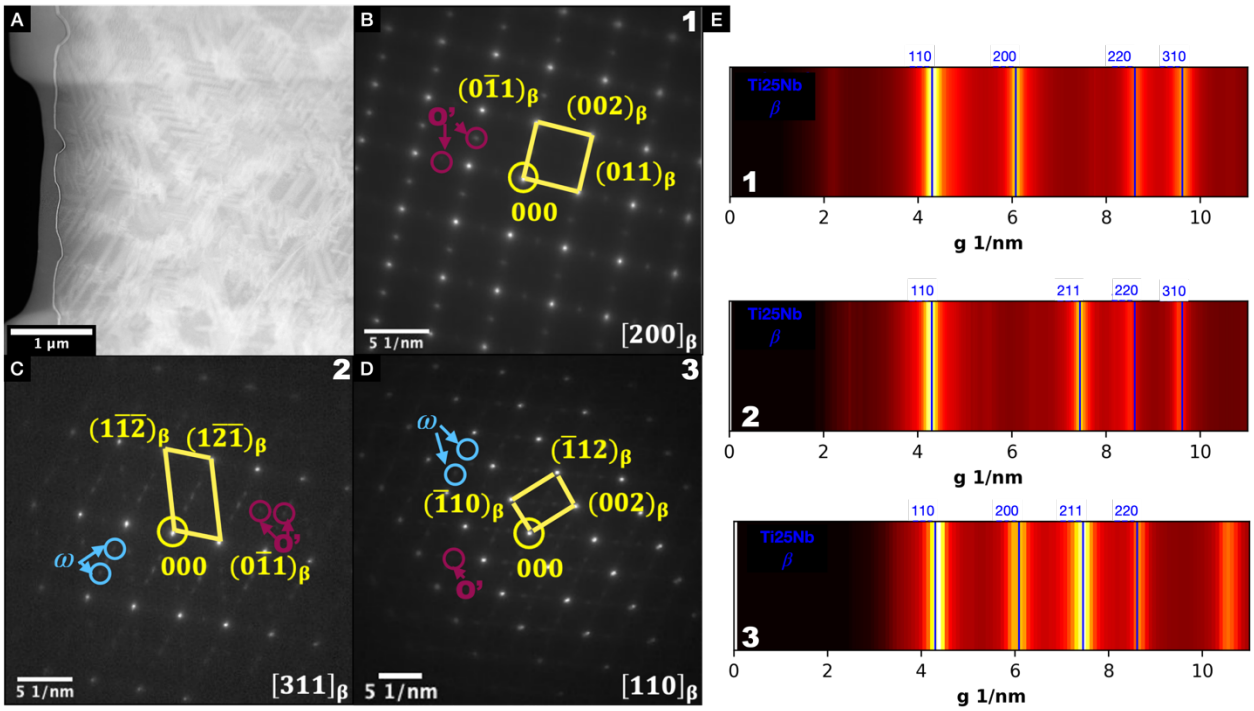

***Figure 44**: Diffraction patterns at various zone axes on Ti25Nb-B. A) STEM DF of Ti25Nb-B. B), C) & D) Diffraction patterns at $[200]_\beta$, $[311]_\beta$, and $[110]_\beta$ zone axes. In each pattern, the 000 spot is circled and the diffraction spots that originated from O' phase as well as ω phase are circled and marked with arrows in wine and blue colors. E) 1D intensity profile (in log scale) vs. g of three patterns are plotted. Within the profile plot, the lines that represent the theoretical g values of selected β planes of Ti-25Nb(at%) are presented in blue color.*

Next, TEM DF images of O' phase at both $[311]_\beta$ and $[110]_\beta$ zone axes are presented in **Figure 45**. The objective aperture was used to select the diffraction signals from O' phase to form DF images. In **Figure 45** B) and C), the DF images exhibit the morphologies of the O' phase. The bright portions in the DF images are the regions that contain O' phase diffraction signals. As it can be seen, the majority of O' phase (marked with orange ovals) in **Figure 45** B) and C) are relatively short and thin elongated plates with less than 100 nm of length and a few tenth nm of width. The growth directions of these plates are slightly different. However, even with only one diffraction peak selected, in each DF image, there is another group of plates (marked with cyan ovals) whose growth direction are about 90 degrees with respect to the prior one. The size of those plates is comparably larger. Similar morphology of the O' phase with two growth directions can be observed at $[110]_\beta$ in **Figure 45** E). Based on the observation, these short and elongated features exist throughout the sample and the distribution is also relatively uniform. Notwithstanding, certain variants seem to be preferred over the other which can be confirmed in the diffraction pattern in **Figure 45** A). Also, there exist preferred growth directions even for the same variant shown in the DF image in **Figure 45** E). The preferred variants have much stronger intensity in the diffraction patterns and a much larger number of plates in DF images.

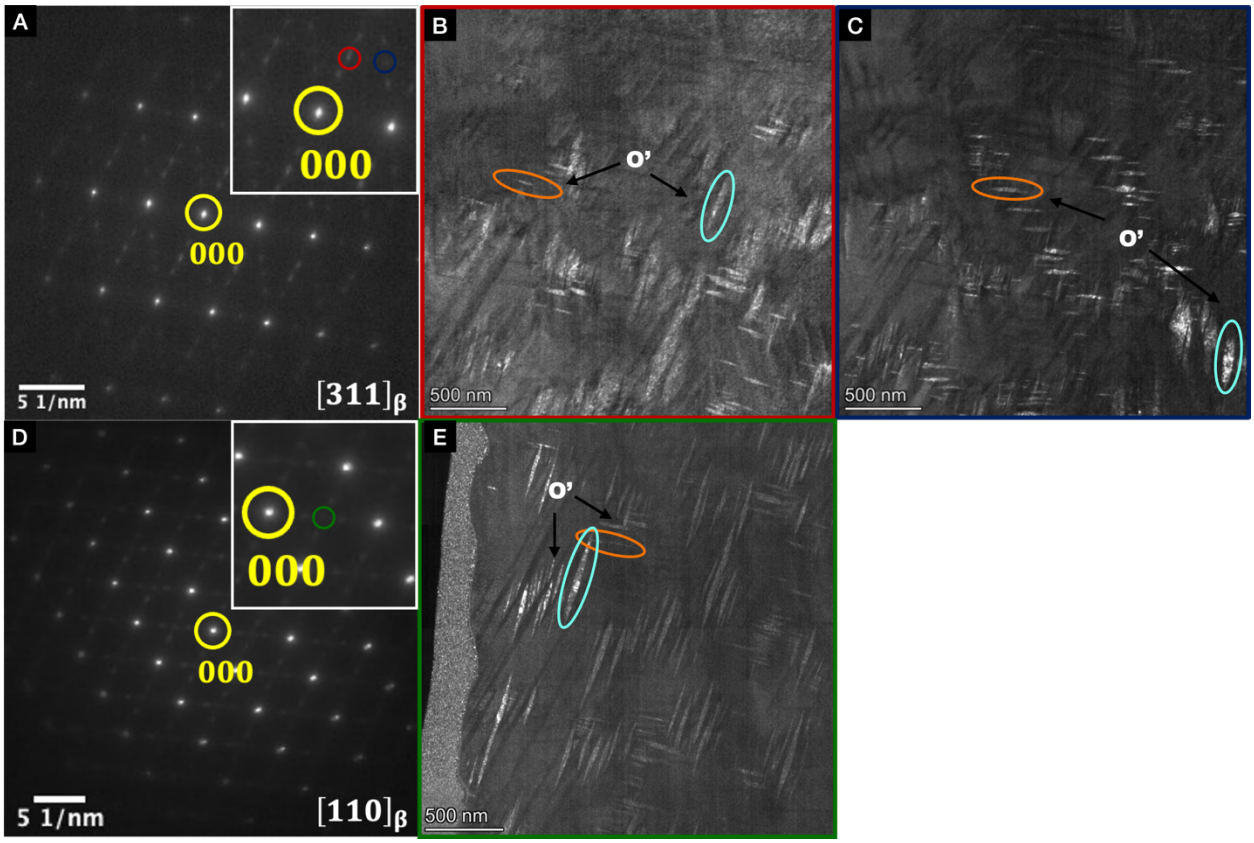

***Figure 45**: TEM DF images of O' phase on Ti25Nb-B. A) & D) Diffraction patterns of Ti25Nb-B at* $[311]_\beta$ *and* $[110]_\beta$ *zone axes. 000 spots are circled with yellow color. Then the locations of objective aperture during the DF imaging are also marked by colored circles which corresponding to the DF images in B), C, and E). Within each DF image, there are two growth directions of O' variants which are marked in orange and cyan color.*

In order to further understand the microstructure of the O' phase, HRSTEM HAADF was performed along the $[200]_\beta$ zone axis, shown in **Figure 46**. A drift correction was applied to account for the linear and nonlinear drift distortion during the probe scanning. This method was first purposed by Ophus et al.[21] using image pairs with orthogonal scan directions on the identical area to reconstruct a drift corrected STEM image. Based on the FFT of the entire frame, it can be seen the β reflections as well as the ones from V1 and V2 variants of the O' phase. By

carefully selecting the area of interest, the regions that contain the V1 or the V2 *O'* variant can be isolated shown in the zoom-in views in **Figure 46** C) and D). Based on the reflections from the FFTs, the area in **Figure 46** C) only contains β and the V1 variant while in **Figure 46** D) it contains the β and the V2 variant. The atomic arrangement in **Figure 46** C) and D) does appear slightly distorted than the area that only has β phase in **Figure 46** B). Still, no sign of lattice discontinuity which is commonly observed on incoherent phase boundary can be observed. This indicates that the O' phase is coherent with the β matrix.

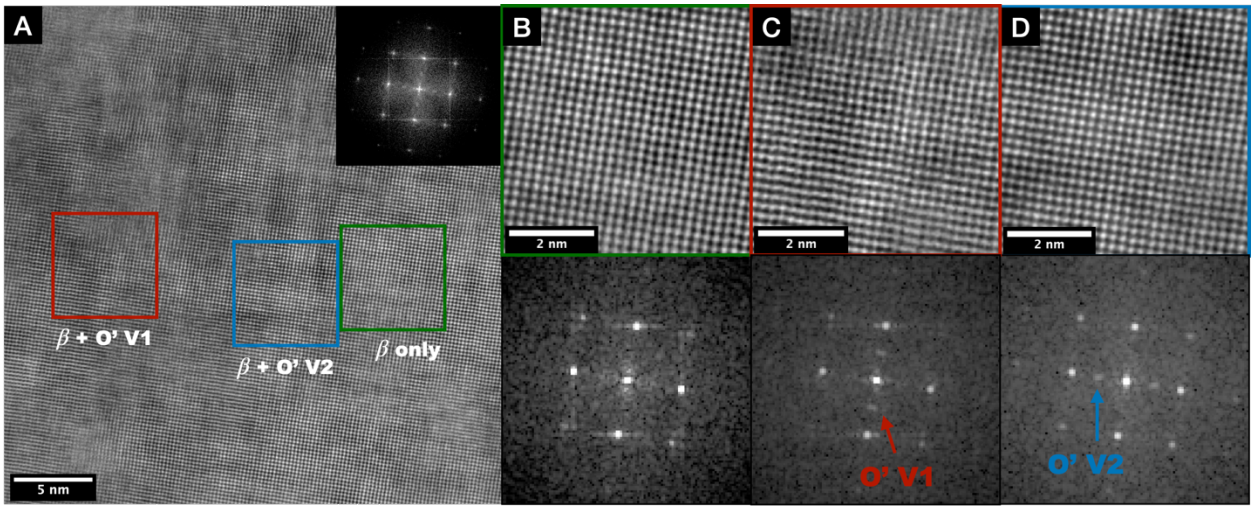

***Figure 46**: HRSTEM HAADF on Ti25Nb-B at* $[200]_\beta$ *zone axis. A) Overall view of the area of interest. The FFT of the entire frame is plotted on the top right corner. Three colored boxes with green, red and blue are marked the selected regions that contain β, β plus O' V1 variant, and β plus O' V2 variant. The corresponding zoom-in views are plotted in B), C), and D) with corresponding FFTs plotted underneath. The O' phase reflections of V1 and V2 variants are indicated by colored arrows in C) and D).*

3.4. Discussion

The microstructure of metastable β-Ti alloys is highly sensitive to both chemical composition as well as thermomechanical history [14,22]. The resultant microstructure usually

contains the metastable phases such as α'' or ω phase. Mechanical properties such as elastic modulus, strength as well as ductility are heavily correlated to the stability of the parent β phase and the composition of these metastable phases [12,23]. In AM, the situations can become further complicated. During rapid solidification, elemental partitioning and subsequent constitutional undercooling create a variety of solidification features within the melt pools [24]. These solidification features such as cells or dendrites usually have slightly different elemental compositions compared to the inter-cellular or inter-dendritic boundaries. For example, Ti is found can segregate into boundary regions during the rapid solidification in Ti-Nb [25]. This can result in non-uniform β stability inside the melt pool. Furthermore, AM might just provide certain conditions to trigger unexpected metastable phases such as O' phase due to the presence of oxygen and the extremely high cooling rate. The source of oxygen can come from the oxygen in the build chamber as well as oxygen in/on the powder or the substrate in the form of interstitial defects or oxide. The high cooling rate limits the diffusion of oxygen, which likely occupy octahedral interstitial sites in the β-Ti lattice [15]. Interstitial oxygen atoms can prompt the formation of O' phase when it experiences a biased internal strain, such as cold rolling, via lattice modulations [15,19,26]. What's more, the existence of this short distance lattice modulation suppresses the long distance martensitic transformation to the α'' phase [26], which aligns with our observation that α'' phase did not appear anywhere within the melt pools studied. Nonetheless, these two TEM samples show major differences despite being captured from the same laser processed substrate which undergoes the same laser processing condition. This implies that the laser processed metastable β-TiNb alloys are highly microstructurally heterogeneous. Yet, it is worth further discussions/clarifications on several observations in the previous section, such as whether the

orthorhombic phase is α'' phase and whether it exists preferred O' variants in such laser processed conditions.

3.4.1. Ti25Nb-A - β phase + unknown orthorhombic phase

Sample Ti25Nb-A was captured from the end of the melt pool array, therefore, it only experience one rapid melting/solidification event. Based on the observation in **Figure 41** A), the resultant microstructure consists of cellular structures and inter-cellular boundaries. In a previous study [11], we consider the larger-sized feature as the "cells" and narrower neighboring features as the "intercellular boundaries". However, according to the phase diagram as well as other studies [25], the Nb-rich regions, which are in brighter intensity, should be the "cells" since they are solidified first in the solidification process. This means the narrower features shown in **Figure 41** A), by definition, are the "cells" instead of "boundaries". It is quite unusual since most of the common AM materials such as stainless steel 316L or Inconel 718 show more distinguishable cells and the inter-cellular boundaries in terms of the noticeable size difference between these two features [1,9]. Based on the phase diagram, the potential explanation is that since the initial solidified "cells" are Nb-rich, due to elemental partitioning, it can result in insufficient Nb to stabilize the β phase in the sequential solidified "boundaries". Therefore, the lower β stability in the Nb-poor regions are susceptible to structural distortion. Yet, the exact mechanism to trigger such a solidification feature set is still unclear since other samples such as Ti25Nb-B show the majority as β phase.

It is confirmed that the Nb-rich region is β phase. However, the Nb-lean region is an orthorhombic phase. Yet, it is also not the expected orthorhombic α'' phase for multiple reasons. First, the lattice parameters of this orthorhombic structure that are calculated based on the

measurements of diffraction patterns differ greatly from the literature values, shown in **Table 3**. Despite the b and c between the measured values and the theoretical values being close, the measured lattice parameter in the a-axis is 11.3% greater than the theoretical value. This cannot be explained by the potential composition difference due to elemental segregation during the rapid solidification since the lattice parameters of the orthorhombic phase does not match the α'' phase for the composition within 12 – 26 at% of Nb the Ti-Nb binary system [14]. Below 12 at% of Nb, α'' is no longer the preferred low temperature martensite phase; while above 26 at% of Nb, the TiNb alloy is fully stabilized as β, One possibility is a simple distortion of the α'' phase, which maintains the same space group of α'' phase as *Cmcm* while increasing the lattice parameter "a" to 0.355 nm because of directional lattice distortion. As it can be seen in **Figure 47**, the g values of crystalline planes of α'' phase based on the literature do not match well with the diffraction pattern shown in **Figure 42** C). The yellow arrow marks indicate the specific unmatched diffraction peaks in the graph. On the other hand, the g values of crystalline planes of the distorted α'' phase can indeed fit well with all diffraction peaks. However, this explanation has two main problems. First, there is still no diffraction pattern from the *Cmcm* space group that can fully match the diffraction pattern of **Figure 42** C). The closest diffraction pattern which is the one at $[112]_{cmcm}$ zone axis can have the matching locations of the diffraction spots if the lattice parameters are the measured values in **Table 3**. Yet, there are superlattice reflections in **Figure 48** A) with reduced intensity while all the allowed reflections in **Figure 48** B) are fundamental reflections from the simulated diffraction pattern. Also, there exist forbidden reflections such as $(20\bar{1})_{cmcm}$ and $(\bar{2}01)_{cmcm}$ spots in the simulated diffraction pattern, shown as green spots in **Figure 48** B). The diffraction pattern of α'' at[112] zone axis with modified lattice parameters cannot match the actual pattern observed. Second, if the orthorhombic phase is assumed to be α'' ,

it should then be formed via martensitic transformation from β phase. Based on the classic invariant plane strain theory, the parent β phase and the formed structure should share a specific invariant plane. According to the calculated results in **Table 4**, the expected invariant plane of β/α'' is (-0.699,-0.506,0.506), which close to what is reported in the literature[27], while that between β and the orthorhombic phase found here is (-0.411,-0.645,0.645). This indicates that such phase transformation cannot be explained by conventional martensitic transformation.

***Table 3**: Lattice parameters comparison*

Phase	a (nm)	b (nm)	c (nm)
β (25Nb at%)	0.329	0.329	0.329
α''(25Nb at%)	0.319	0.479	0.463
Unknown phase (Measured)	0.355	0.469	0.462

*The theoretical values are calculated based on the publication [14].

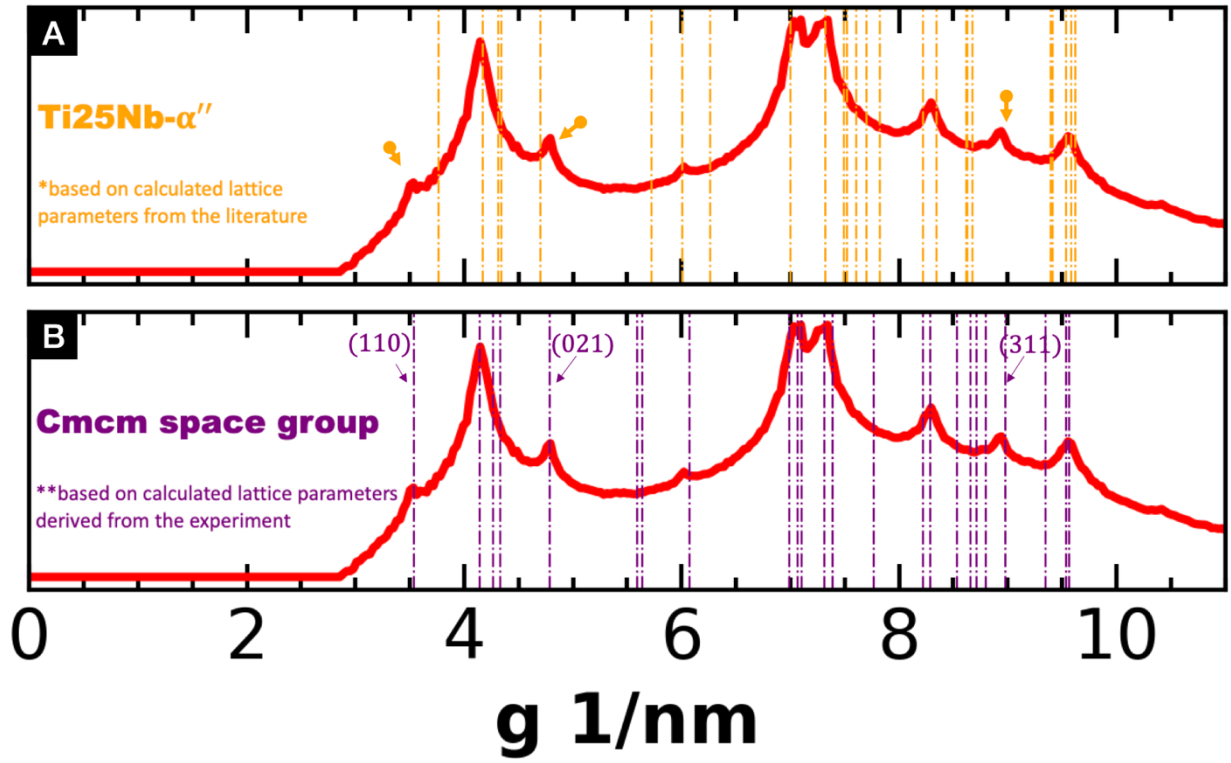

Figure 47*: 1D intensity line profile (in log scale) vs. g of the diffraction pattern in* ***Figure 42*** *C). The intensity of pixels that have the same distance to the 000 spot are summed up. In order to properly display the peaks, the intensity values near the 000 spot are set to 0 and the rest of intensity values are normalized. A) The theoretical g values of all α'' planes of Ti-25Nb(at%) are presented in orange lines. Peaks that cannot be indexed as α'' planes are marked by orange color arrows. B) If assume the orthorhombic structure which shares the same space group of α'' phase as Cmcm, then the calculated g values of all the planes in this structure are presented in purple lines.*

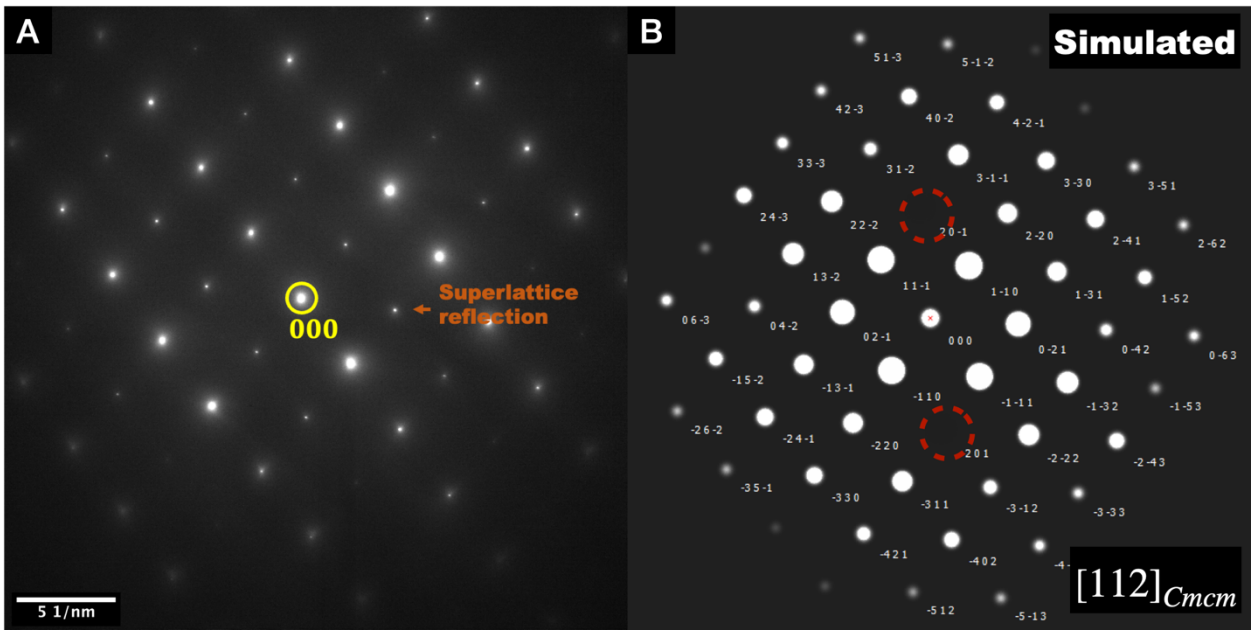

***Figure 48**: Comparison between A) the diffraction pattern in **Figure 42** C). B) Dynamic diffraction simulation of α'' phase with measured lattice parameters listed in **Table 3** using ReciPro software [28]. The size of the spots represents the strength of the diffraction intensity. The red dotted circles indicate where the diffraction reflections are forbidden.*

***Table 4**: Calculations based on the invariant plane strain theory for the martensitic transformation from $\beta \rightarrow \alpha''$ phase and from $\beta \rightarrow$ unknown orthorhombic phase assume it is under the same mechanism.*

	$\beta \rightarrow \alpha''$ (25Nb at%)	$\beta \rightarrow$ unknown phase
Bain Matrix	$\begin{bmatrix} 0.9515 & 0 & 0 \\ 0 & 1.0241 & 0.0242 \\ 0 & 0.0242 & 1.0241 \end{bmatrix}$	$\begin{bmatrix} 1.0807 & 0 & 0 \\ 0 & 1.0020 & -0.0075 \\ 0 & -0.0075 & 1.0020 \end{bmatrix}$
Habit plane	(-0.699,-0.506,0.506)	(-0.411,-0.645,0.645)
Invariant plane strain direction	$(0.733, -0.481, 0.481)^T$	$(0.440, -0.635, 0.635)^T$

Magnitude of invariant plane strain	0.09686	0.0854

In summary, the microstructure of metastable β-Ti alloys that are being laser melted once but without being reheated is consisting of β (Nb-rich) and an unidentified orthorhombic phase (Nb-lean) in lamella arrangement.

3.4.2. Ti25Nb-B - β phase + O' phase + ω phase

In contrast, Sample Ti25Nb-B has a noticeably different morphology from Ti25Nb-A. It experiences additional short reheating steps from the laser melting of the neighboring scan tracks. Instead of having long elongated cellular structures, Sample Ti25Nb-B contains numerous short plates, which are identified as of O' phase by comparing to published data, as well as ω phase inside the β grains, as it can be seen in **Figure 44** A). These O' flat plates are formed due to the lattice modulation of the β lattice in $\{011\} < 0\bar{1}1 >_{\beta}$ shuffling mode, which is demonstrated in **Figure 49**. Since the O' phase can be viewed as the α'' phase without the partial $\{211\} < \bar{1}\bar{1}1 >_{\beta}$ shear, it shares the same lattice correspondences as well as conventions as α'' [15]. There are a total six variants of O' phase in β matrix. These variants can be imaged by placing the objective aperture over the corresponding diffraction spots, as shown in **Figure 45**. One note here is that the appearance of O' phase, or nanodomains, in the laser processed metastable β-Ti alloys is unexpected. Usually, in casted or solutionized conditions, the corresponding diffraction intensities often display as diffused streaks at various β zone axes [18], indicating the minor modulation of the β lattice. In contrast, based on the diffraction patterns in **Figure 44**, the diffraction of O' phase clearly appears as discrete spots. Kim et al. demonstrated that O' phase (or nanodomains) increases

after cold rolling, displaying discrete diffraction spots in the diffraction patterns [17]. Similarly, Tahara et al. also reported β phase can transform to O' phase during the tensile loading [18] This implies that the rapid solidification can generate certain defects which has a similar effect of heavy deformation such as cold rolling to the metal. Although there is no direct measurement of dislocation density of rapid solidified β-Ti alloys, the general estimation of the dislocation density of additive manufactured metals is around $\boxed{10^{14}m^{-2}}$[9], closer to heavily strained situation.

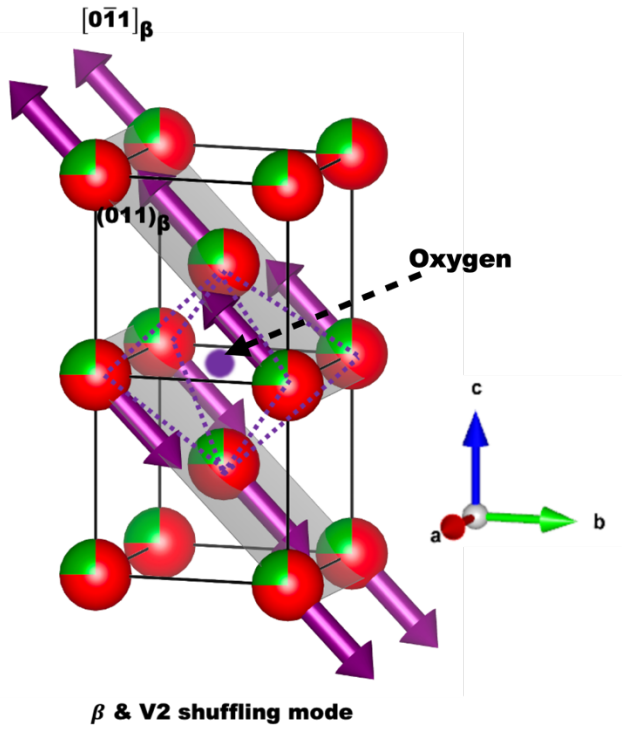

***Figure 49**: A schematic of lattice shuffling mode of V2 variant of O' phase. V2 variant, based on the convention, has a shuffle mode of* $(011)[0\bar{1}1]_\beta$*[17]. The atomic model is generated in VESTA [29].*

In this case, rapid solidification during LPBF can generate a similar variant selection effect that is observed after cold rolling as well [17]. 4D STEM is performed within the selected area of interest indicating the V1 O' variant is preferred, as shown in **Figure 50** A). The electron beam is converged to 1.5 mrad in order to form the convergent beam electron diffraction (CBED) condition

that no diffraction disk is overlapped with others. Next, 4D STEM virtual DF images of V1 and V2 O' variants can be generated as shown in **Figure 50** B) and C). The intensity of each pixel in the virtual DF image can be calculated by carefully setting filter masks that locate at the center of the diffraction disks of O' variants in the CBED patterns as shown in **Figure 50** E). If the location has either V1 or V2 variant exists, then the CBED pattern of that pixel should have corresponding diffraction disks in appearance. For example, **Figure 50** F) and G) demonstrate the CBED pattern of two pixels in **Figure 50** A) where only V1 or V2 exist. Last, the phase map of V1 and V2 is shown in **Figure 50** D). The map is generated by comparing the diffraction intensity of V1, V2, and the background signal in each pixel. If the intensity from the V1 variant is notably higher, then the pixel color is assigned as green. Similarly, the pixel color is assigned to red if the intensity of the V2 variant is outstanding. The rest of the pixels are left as background if the intensities from both variants are close to the background. As it can be seen, V1 has significantly more area than V2, which suggests V1 is favored in this sample region.

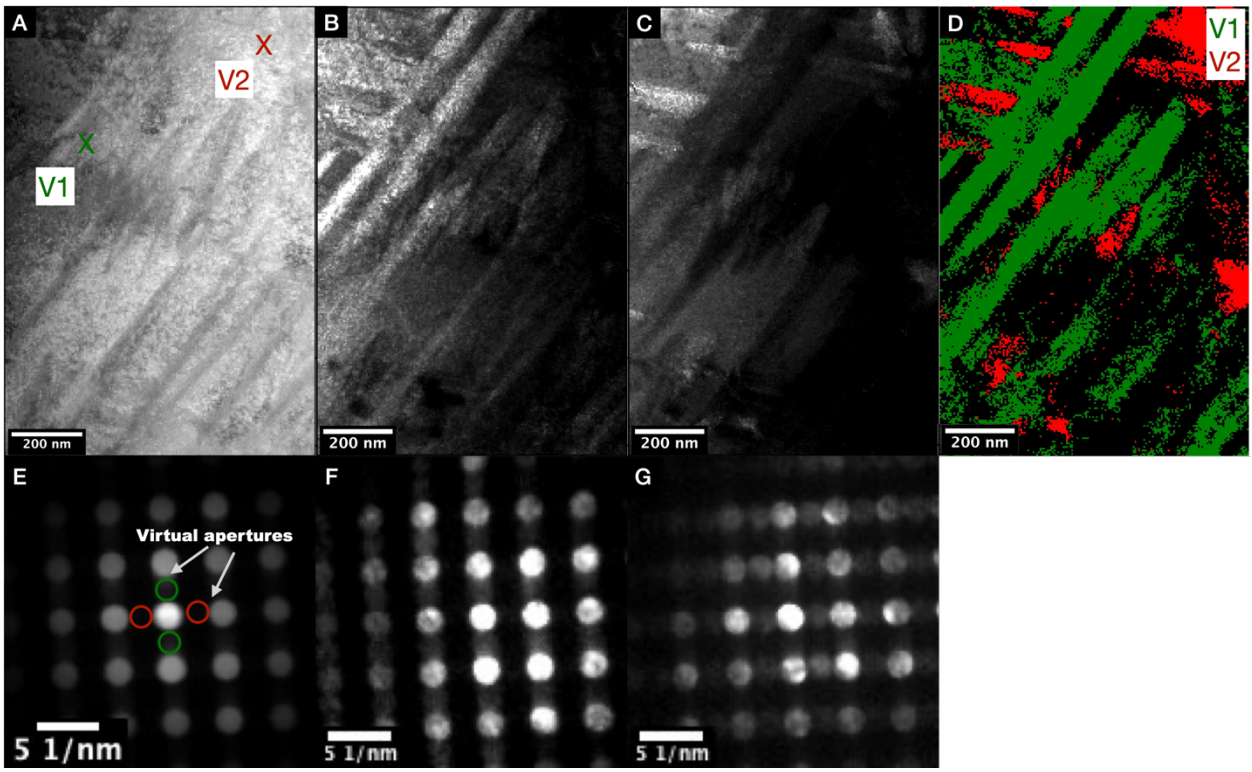

***Figure 50**: 4D STEM analysis of Ti25Nb-B at* $[200]_{\beta}$ *zone axis. The 4D STEM data is captured by Gatan 4D STEM module. Then the data is processed via a custom Python code with the implementation of HyperSpy toolbox[20]. A) The annual dark field (ADF) image of area of interest. Two locations are marked with color-coded "X" to indicate where the convergent beam electron diffraction (CBED) patterns are obtained shown in F) and G). B) and C) virtual dark field images of V1 and V2 O' phase via proper masking the diffraction signals in the reciprocal space as it shown in E). D) Phase mapping of V1 and V2 O' phase by comparing the diffraction intensities of in the masks of V1, V2, and background signal in each pixel in real space. If V1 or V2 diffraction intensity is higher than others, the pixel color is assigned as green or red respectively. However, if intensities of both V1 and V2 are close to the background, then the pixel color is assigned as black.*

The current study suggests that rapid solidification can create microstructural configurations that differ from the microstructure in metastable β-Ti alloys using conventional methods. The micro elemental segregation, as well as the thermal strain from the rapid

solidification, might greatly affect the local β stability. In an actual printed sample, it is likely that top layer might be closer to Ti25Nb-A yet the interior might be closer to Ti25Nb-B. The formation of O' phase is believed that can release internal stresses which might improve the ductility [17]. On the other hand, the existence of brittle ω phase can reduce such effect. Therefore, the mechanical tests on actual printed samples are needed to ensure the impact of O' phase on mechanical performance. Furthermore, the stability of such microstructure is yet to be tested. Since these microstructures stay at a local energy minimum, therefore, heat treatments during the larger build or from post-processing may resume it back to a more normal microstructure partially or completely. Particularly, oxygen atoms may redistribute themselves in the matrix due to the increased diffusion rate during the heat treatment. Then the short-distanced O' phase may get replaced by long-distanced α'' martensite [26].

3.5. Conclusions

In this study, we conducted rapid solidification through laser scan on a Ti-25Nb(at%) substrate. Examination through electron microscopy yielded the following conclusions:

1. A previously unknown orthorhombic phase is found in Nb-lean region of the laser-processed TiNb sample. Compared to the α'' orthorhombic phase, it has a larger "a" lattice parameter or similar c/a ratio. Also, it follows dissimilar theoretical transformation path from the parent β phase.
2. O' phase is detected in a laser-processed metastable TiNb sample. Previously, this phase has only been reported in heavily cold-worked samples, which suggests that the internal stress due to rapid solidification might favor the formation of O' phase and certain O' variants.

3. Processing history has a significant impact on the resultant microstructures in metastable TiNb alloys. Regions that experience multiple remelting/reheating passes have different microstructures compared to ones that have only been melted once.
4. Laser processing suppresses the long range α'' phase and prompt short range O' phase or distorted β phase.
5. The microstructure of laser processed TiNb is unlike other additive manufactured metals. No dislocation network or little elemental micro-segregation (a few at%) is observed in laser processed TiNb samples.

3.6. References

[1] T. DebRoy, H.L. Wei, J.S. Zuback, T. Mukherjee, J.W. Elmer, J.O. Milewski, A.M. Beese, A. Wilson-Heid, A. De, W. Zhang, Additive manufacturing of metallic components – Process, structure and properties, Prog. Mater. Sci. 92 (2018) 112–224. https://doi.org/10.1016/j.pmatsci.2017.10.001.

[2] H.L. Wei, T. Mukherjee, W. Zhang, J.S. Zuback, G.L. Knapp, A. De, T. DebRoy, Mechanistic models for additive manufacturing of metallic components, Prog. Mater. Sci. 116 (2021). https://doi.org/10.1016/j.pmatsci.2020.100703.

[3] N. Li, S. Huang, G. Zhang, R. Qin, W. Liu, H. Xiong, G. Shi, J. Blackburn, Progress in additive manufacturing on new materials: A review, J. Mater. Sci. Technol. 35 (2019) 242–269. https://doi.org/10.1016/j.jmst.2018.09.002.

[4] Y. Kok, X.P. Tan, P. Wang, M.L.S. Nai, N.H. Loh, E. Liu, S.B. Tor, Anisotropy and heterogeneity of microstructure and mechanical properties in metal additive manufacturing: A critical review, Mater. Des. 139 (2018) 565–586. https://doi.org/10.1016/j.matdes.2017.11.021.

[5] A. Hadadzadeh, B.S. Amirkhiz, A. Odeshi, M. Mohammadi, Dynamic loading of direct metal laser sintered AlSi10Mg alloy: Strengthening behavior in different building directions, Mater. Des. 159 (2018) 201–211. https://doi.org/10.1016/j.matdes.2018.08.045.

[6] T.G. Gallmeyer, S. Moorthy, B.B. Kappes, M.J. Mills, B. Amin-Ahmadi, A.P. Stebner, Knowledge of process-structure-property relationships to engineer better heat treatments for laser powder bed fusion additive manufactured Inconel 718, Addit. Manuf. 31 (2020). https://doi.org/10.1016/j.addma.2019.100977.

[7] S. Liu, Y.C. Shin, Additive manufacturing of Ti6Al4V alloy: A review, Mater. Des. 164 (2019). https://doi.org/10.1016/j.matdes.2018.107552.

[8] L. Liu, Q. Ding, Y. Zhong, J. Zou, J. Wu, Y.L. Chiu, J. Li, Z. Zhang, Q. Yu, Z. Shen, Dislocation network in additive manufactured steel breaks strength–ductility trade-off, Mater. Today. 21 (2018) 354–361. https://doi.org/10.1016/j.mattod.2017.11.004.

[9] D. Kong, C. Dong, S. Wei, X. Ni, L. Zhang, R. Li, L. Wang, C. Man, X. Li, About metastable cellular structure in additively manufactured austenitic stainless steels, Addit. Manuf. 38 (2021) 101804. https://doi.org/10.1016/j.addma.2020.101804.

[10] Y.M. Wang, T. Voisin, J.T. McKeown, J. Ye, N.P. Calta, Z. Li, Z. Zeng, Y. Zhang, W. Chen, T.T. Roehling, R.T. Ott, M.K. Santala, P.J. Depond, M.J. Matthews, A. V. Hamza, T. Zhu, Additively manufactured hierarchical stainless steels with high strength and ductility, Nat. Mater. 17 (2018) 63–70. https://doi.org/10.1038/NMAT5021.

[11] M. Long, H.J. Rack, Titanium alloys in total joint replacement--A materials science perspective., Biomaterials. 19 (1998) 1621–39. https://doi.org/10.1016/S0142-9612(97)00146-4.

[12] R. Kolli, A. Devaraj, A Review of Metastable Beta Titanium Alloys, Metals (Basel). 8 (2018) 506. https://doi.org/10.3390/met8070506.

[13] W. Lin, H. Heinrich, J. Ma, Unusual strain relaxation mechanism in metastable β Ti-Nb alloy after rapid solidification, Scr. Mater. 211 (2022) 114499. https://doi.org/https://doi.org/10.1016/j.scriptamat.2022.114499.

[14] H.Y.Y. Kim, Y. Ikehara, J.I.I. Kim, H. Hosoda, S. Miyazaki, Martensitic transformation, shape memory effect and superelasticity of Ti–Nb binary alloys, Acta Mater. 54 (2006) 2419–2429. https://doi.org/10.1016/j.actamat.2006.01.019.

[15] Q. Liang, D. Wang, Y. Zheng, S. Zhao, Y. Gao, Y. Hao, R. Yang, D. Banerjee, H.L. Fraser, Y. Wang, Shuffle-nanodomain regulated strain glass transition in Ti-24Nb-4Zr-8Sn alloy, Acta Mater. 186 (2020) 415–424. https://doi.org/https://doi.org/10.1016/j.actamat.2019.12.056.

[16] P. Castany, Y. Yang, E. Bertrand, T. Gloriant, Reversion of a Parent 310 α″ Martensitic Twinning System at the Origin of {332 } 113 ©β Twins Observed in Metastable β Titanium Alloys, Phys. Rev. Lett. 117 (2016). https://doi.org/10.1103/PhysRevLett.117.245501.

[17] H.Y. Kim, L. Wei, S. Kobayashi, M. Tahara, S. Miyazaki, Nanodomain structure and its effect on abnormal thermal expansion behavior of a Ti-23Nb-2Zr-0.7Ta-1.2O alloy, Acta Mater. 61 (2013) 4874–4886. https://doi.org/10.1016/j.actamat.2013.04.060.

[18] M. Tahara, H.Y. Kim, T. Inamura, H. Hosoda, S. Miyazaki, Lattice modulation and superelasticity in oxygen-added β-Ti alloys, Acta Mater. 59 (2011) 6208–6218. https://doi.org/10.1016/j.actamat.2011.06.015.

[19] M. Tahara, H.Y. Kim, T. Inamura, H. Hosoda, S. Miyazaki, Role of interstitial atoms in the microstructure and non-linear elastic deformation behavior of Ti-Nb alloy, J. Alloys Compd. 577 (2013) S404–S407. https://doi.org/10.1016/j.jallcom.2011.12.113.

[20] F. de la Peña, E. Prestat, V.T. Fauske, P. Burdet, J. Lähnemann, P. Jokubauskas, T. Furnival, M. Nord, T. Ostasevicius, K.E. MacArthur, D.N. Johnstone, M. Sarahan, T. Aarholt, J. Taillon, pquinn-dls, V. Migunov, A. Eljarrat, J. Caron, C. Francis, T. Nemoto, T. Poon, S. Mazzucco, actions-user, N. Tappy, N. Cautaerts, S. Somnath, T. Slater, M. Walls, F. Winkler, DENSmerijn, hyperspy/hyperspy: Release v1.7.0, (2022). https://doi.org/10.5281/ZENODO.6492919.

[21] C. Ophus, J. Ciston, C.T. Nelson, Correcting nonlinear drift distortion of scanning probe and scanning transmission electron microscopies from image pairs with orthogonal scan directions, Ultramicroscopy. 162 (2016). https://doi.org/10.1016/j.ultramic.2015.12.002.

[22] T. Inamura, J.I. Kim, H.Y. Kim, H. Hosoda, K. Wakashima, S. Miyazaki, Composition dependent crystallography of α″-martensite in Ti-Nb-based β-titanium alloy, Philos. Mag. 87 (2007). https://doi.org/10.1080/14786430601003874.

[23] S. Miyazaki, My Experience with Ti–Ni-Based and Ti-Based Shape Memory Alloys, Shape Mem. Superelasticity. 3 (2017) 279–314. https://doi.org/10.1007/s40830-017-0122-3.

[24] B. Fotovvati, S.F. Wayne, G. Lewis, E. Asadi, A Review on Melt-Pool Characteristics in Laser Welding of Metals, Adv. Mater. Sci. Eng. 2018 (2018). https://doi.org/10.1155/2018/4920718.

[25] J.D. Roehling, A. Perron, J.L. Fattebert, T. Haxhimali, G. Guss, T.T. Li, D. Bober, A.W. Stokes, A.J. Clarke, P.E.A. Turchi, M.J. Matthews, J.T. McKeown, Rapid Solidification in Bulk Ti-Nb Alloys by Single-Track Laser Melting, JOM. 70 (2018) 1589–1597. https://doi.org/10.1007/s11837-018-2920-2.

[26] M. Tahara, T. Inamura, H.Y. Kim, S. Miyazaki, H. Hosoda, Isothermal martensitic transformation behavior of Ti–Nb–O alloy, Mater. Lett. 257 (2019). https://doi.org/10.1016/j.matlet.2019.126691.

[27] Y.W. Chai, H.Y. Kim, H. Hosoda, S. Miyazaki, Self-accommodation in Ti-Nb shape memory alloys, Acta Mater. 57 (2009) 4054–4064. https://doi.org/10.1016/j.actamat.2009.04.051.

[28] Y. Seto, M. Ohtsuka, ReciPro : free and open-source multipurpose crystallographic software integrating a crystal model database and viewer, diffraction and microscopy simulators, and diffraction data analysis tools , J. Appl. Crystallogr. 55 (2022). https://doi.org/10.1107/s1600576722000139.

[29] K. Momma, F. Izumi, VESTA: A three-dimensional visualization system for electronic and structural analysis, J. Appl. Crystallogr. 41 (2008). https://doi.org/10.1107/S0021889808012016.

4. Fabricate Low Modulus High Strength Metastable Beta Ti-Nb in LPBF

4.1.Introduction

In recent years, conventional metals, such as stainless steel, Inconel, aluminum alloys, and aerospace titanium alloys, have been successfully adapted to additive manufacturing (AM). In addition to simplifying the fabrication of customized and/or geometrically complex parts, AM also unlocks unique material physics, such as hierarchical solidification microstructures [1], which are believed to significantly control material properties such as strength and ductility [2-6]. However, certain material properties, such as elastic modulus, are still difficult to control in AM. In fields such as biomedical implants, AM is considered the future manufacturing method, which can greatly benefit from fabricated parts with reduced modulus to exhibit enhanced biomechanical compatibility with human bones [7,8]. Essentially, this requires achieving an elastic modulus in the fabricated parts that closely matches that of bones to prevent bone degradation following implantation.

Metastable β-Ti alloys represent the next generation of materials for biomedical applications, particularly in the realm of orthopedics [8-10]. These alloys are engineered to exhibit high strength and low modulus in order to match the mechanical properties of human bone structure. Conventionally, alloys such as Ti-Mo-Zr-Fe (TMZF) and Ti-Nb-Ta-Zr (TNZT) can attain low modulus values around 50 GPa [8]. However, this is still considerably higher than the typical modulus value of cortical bones, which falls below 20 GPa [7,8]. AM offers new opportunities for producing biomedical implants using metastable β-Ti alloys. One method involves utilizing AM to create metallic scaffolds with a high degree of porosity, effectively reducing the stiffness of the components. The main disadvantage, however, is that these scaffolds exhibit significantly lower strength compared to fully dense parts [7,11,12]. For instance, a porous

TiNbZr alloy with 42% porosity possesses a strength of 500 MPa, while a counterpart with 74% porosity has merely one-tenth of the former's strength [11].

Another approach is to tailor the mechanical performance, including elastic modulus, of the as-printed parts by microstructure engineering. It is known that AM can control local texture and grain morphology [2,13,14]. For example, Dehoff et al. demonstrated the control of random or <100> texture along the build direction on Inconel 718 through varying scan strategies [13]. This affects the thermal gradient (G) and liquid-solid interface velocity (R) within the melt pool, leading to different solidification modes. Furthermore, the scan path also has a significant impact on texture and grain morphology development, as shown by altering hatch length/pattern as well as the sequence of the pre-designed laser vectors to locally control texture or grain morphology [15,16]. Plotkowski et al. advanced this further by using a novel scan pattern algorithm to precisely manipulate epitaxial dendrite growth and grain nucleation, forming the shape of the Mona Lisa in Inconel 718 [17]. However, there are still limitations in controlling texture and grain morphology. Most scan strategies still produce textures and morphologies that are strongly dependent on the building direction, limiting the freedom of microstructure regulation [2,18]. This means it heavily relies on the grain orientation directly beneath that layer for controlling texture. For instance, Sofinowski et al. showed the method of engineering grain orientation through strongly textured blocks along the building direction [19], yet this method cannot extend the existing type of strong texture within the same layer.

Besides texture and grain morphology, other critical aspects like phase composition and defects must be understood to control the mechanical properties of as-printed metastable β-Ti alloys. Conventionally, multiple stages of thermo-mechanical treatments are required to achieve the desired microstructure, particularly regarding phase composition. In contrast, AM greatly

simplifies these procedures. However, due to the sensitivity of these alloys to their thermo-mechanical history, understanding how rapid solidification combined with multiple remelting events affects the final microstructure of metastable β-Ti alloys remains limited. For example, in the author's previous studies on laser-processed Ti-25Nb (at%) specimens, an unknown orthorhombic metastable phase and unusual lattice distortion were observed [20]. Additionally, it has been suggested that remelting events can further influence the microstructure. At present, it is unclear whether such unique metastable states produced by AM can exhibit significantly different mechanical properties, especially in terms of elastic modulus. Moreover, AM-related solidification boundaries, such as melt pool and cellular boundaries, are considered to present similar obstacles as grain boundaries, albeit weaker. According to Kong et al., smaller intercellular spacing, or equivalently, more cellular boundaries, can increase mechanical strength [21]. This suggests that an increase in melt pool boundaries should also enhance strength. However, few published studies have provided evidence to support this claim.

In this study, metastable β titanium-niobium (Ti-Nb) alloys, specifically Ti-25Nb (at%), were produced using a laser powder bed fusion (LPBF) system. The as-printed microstructure and tensile performance of Ti-25Nb (at%) were investigated. Additionally, the study demonstrated a viable approach for achieving low modulus and high strength in metastable β alloys simultaneously through AM.

4.2. Methods

Ti-25Nb (at%) powder was produced by ECKART GmbH (Hartenstein, Germany) using gas atomization under an inert Ar environment. The printing was carried out using an SLM 125 laser powder bed fusion system (SLM Solutions Inc.). A 125mm x 125mm x 50mm cp-Ti substrate

was used. Two sets of samples were fabricated in this study with differing process parameters, the Ti25Nb-120HD samples were fabricated using 275W laser power, 800mm/s scan speed, a 120μm hatch distance, and a 50μm layer thickness. The Ti25Nb-10HD samples were fabricated using the same laser power and speed but with a dense scan pattern of 10 μm hatch distance and a 100 μm layer thickness. No scan rotation was applied between layers. The schematical comparison of the two scan strategies used for the two sample sets is depicted in **Figure 51** A). Two extra steps were incorporated during the fabrication of Ti25Nb-10HD samples set to produce fully dense parts. First, an in-situ sintering step was implemented using a 100W laser power, 800mm/s laser speed, a hatch distance of 120 μm, and a layer thickness of 50 μm. This minimizes the amount of powder that is blown away during laser scanning. Second, the laser scanning path was modified to incorporate additional waiting time to prevent extreme heat flux accumulation in any specific regions. 10mm x 50mm x 1mm rectangles of as-printed Ti25Nb-10HD are shown in **Figure 51** B). As comparison, Ti-25Nb (at%) solution treated samples (Ti25Nb as-ST) were produced by vacuum arc melting then heat treated at 900℃ for 2 hrs in an argon atmosphere follow up water quench. 3 mm thick Ti25Nb as-ST was then cold rolled by 67% to 1mm thickness (Ti25Nb 67% CR).

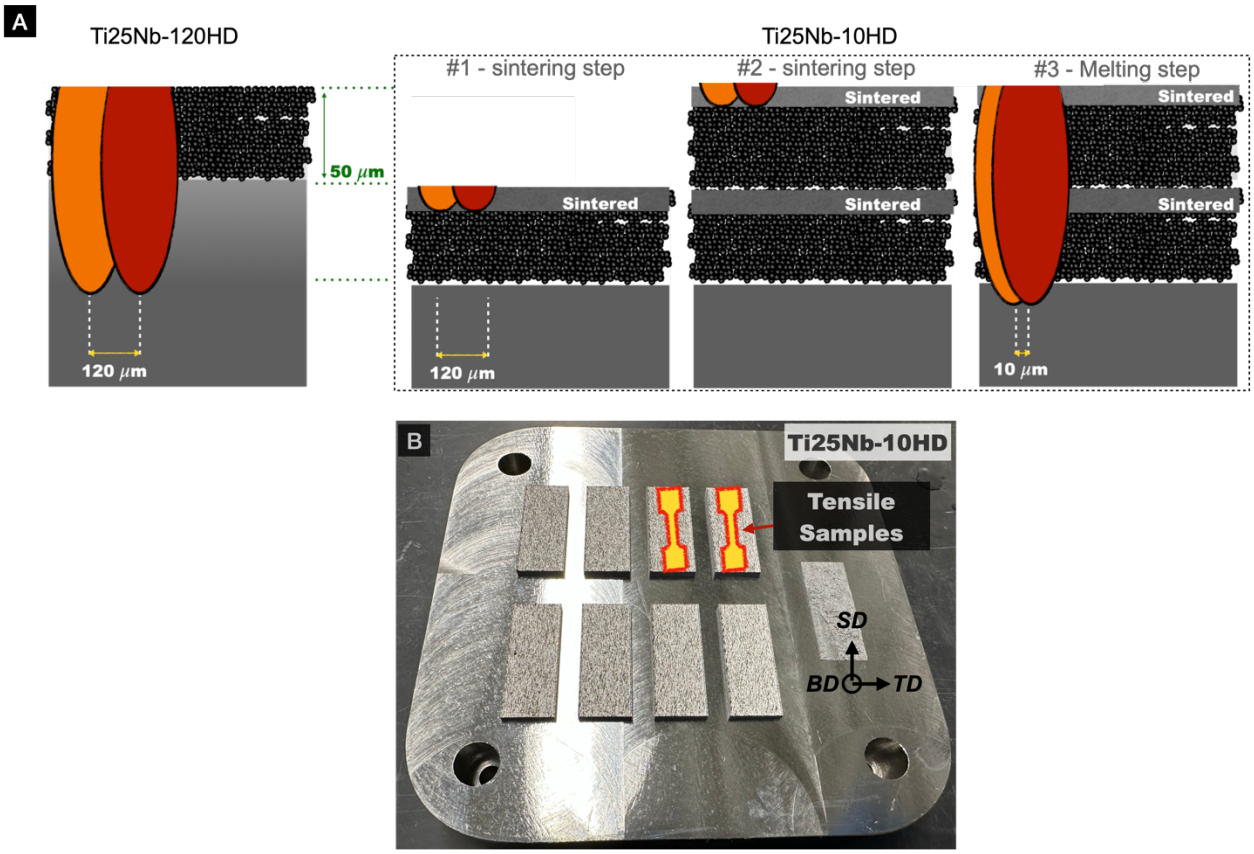

***Figure 51**: A) A schematic comparison between Ti25Nb-120HD and Ti25Nb-10HD building parameters. Ti25Nb-120HD uses a layer thickness of 50µm and a hatch distance of 120µm. On the other hand, Ti25Nb-10HD uses a layer thickness of 100µm and a hatch distance of 10µm. Additional steps are applied to achieve fully dense parts. First, an in-situ sintering step is applied every 50 µm powder layer to moderately solidify several µm deep of powder particles (#1 & #2 steps). Then, the laser scan path is altered to allow newly melted regions have enough time to cool down (#3 step). B) 10mm x 50mm x 1mm rectangles of as-printed Ti25Nb-10HD samples are on the Ti substrate. It is also indicated where tensile samples were machined from those rectangular as-printed parts.*

Next, the as-printed rectangles were removed from the substrate using a wire electrical discharge machine (W-EDM). Some of Ti25Nb-120HD and Ti25Nb-10HD samples were heat treated at 300°C or 600°C under high purity argon atmosphere for 1 hour, followed by water

quenching. Some samples were further machined to create flat dog-bone tensile samples. Tensile tests were conducted on an MTS Criterion electromechanical loading frame, with an external extensometer directly attached to the the gage section of the sample. The crystal structure and phase composition were determined using x-ray diffraction (XRD) on an Empyrean diffractometer (Malvern-Panalytica) equipped with Cu anode x-ray source (1.54Å wavelength). XRD peak fitting was carried out using a custom Python script based on LMFIT library [22]. Additional samples were sliced and mechanically polished to 0.05 μm colloidal silica. Electron backscatter diffraction (EBSD) was conducted using a Helios G4 Dual-Beam FIB-SEM (FEI Company) and scanning electron microscopy (SEM) imaging was performed on a Quanta 650 (FEI Company) system. A sample of Ti25Nb-10HD for transmission electron microscope (TEM) was machined using Helios, and TEM diffraction experiments was conducted using Themis Z (60-300 kV) TEM (FEI Company).

4.3. Results

Ti25Nb (at%) is a metastable β Ti alloy with primarily a body-centered cubic (BCC) structure at room temperature due to the presence of Nb as a β stabilizer. However, the Nb composition is not sufficient to fully stabilize the alloy as β phase, resulting in a noticeable fraction of α'' martensite phase, which has an orthorhombic structure. XRD results in **Figure 52** A) show that the as-solution treated sample (Ti25Nb as-ST) displays both β and α'' phases. Both Ti25Nb-HD120 and Ti25Nb-HD10, however, have XRD patterns reveal that α'' phase is heavily suppressed. Evidence of this can be seen in the intensity of the expected location of the α''peaks, which appear to be absent or greatly reduced. Instead, new peaks appear at the left shoulder of the β peaks, shown in **Figure 52** B) & C). This is supported by a comparison in **Figure 52** D), which

shows a shift in the d-spacings of $(110)_\beta$, $(211)_\beta$, and their shoulder peaks. This phenomenon was also observed in a previous study using transmission electron microscopy (TEM), which will be discussed in a later section. Additionally, XRD results show that a 600°C furnace heat treatment for 1 hour did not affect the overall crystal structure of the printed samples. Notably, no α'' peaks reappeared, while the β peaks remained relatively unchanged, but with slight shifts in the shoulder peaks.

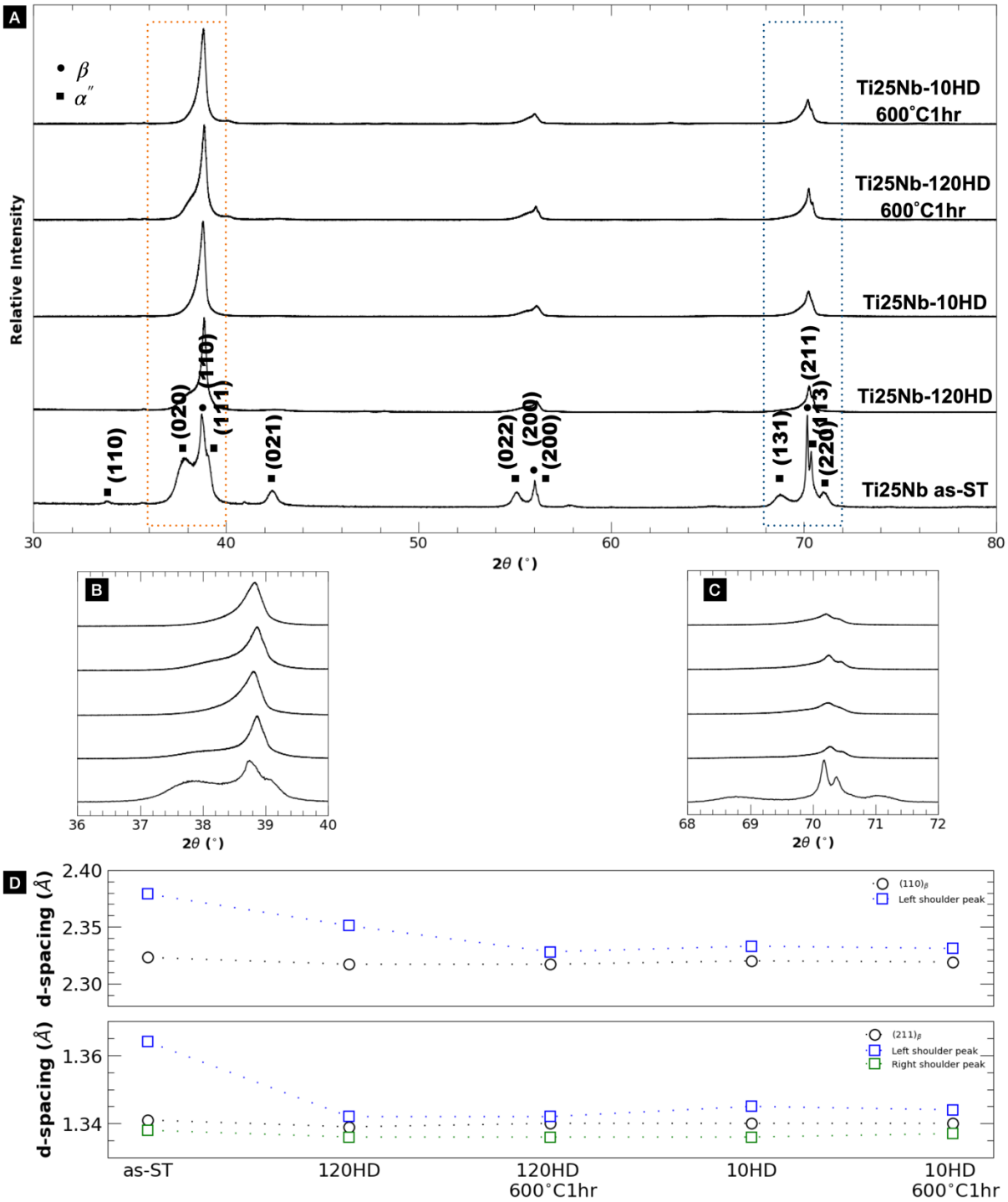

***Figure 52**: A) XRD spectra of Ti25Nb samples of as solution treated (as-ST), Ti25Nb-120HD, Ti25Nb-10HD as well as samples received 600°C 1hr furnace heat treatment. B) & C) Zoom-in view of spectra of 2θ range from 36° - 40° and 68° - 72°. D) D-spacing comparison among different sample conditions of $(110)_\beta$, $(211)_\beta$, as well as their left and/or right shoulder peaks based on the peak fitting results.*

The microstructure of Ti25Nb-120HD is similar to that of other metals created through additive manufacturing with comparable scanning patterns [23], as demonstrated in **Figure 53**. Two samples were examined using EBSD in two orientations: one in cross-sectioned view in **Figure 53** A), with the scanning direction being perpendicular with the polished surface, and the other in a top-down view in **Figure 53** B), with the building direction being perpendicular with the polished surface. Both orientation show colonies of grains which appear to be flat strips. The side of those colonies seem to be bounded by "walls", which indicate the middle lines of melt pools. The width of those colonies is roughly equal to the hatch distance (120 μm). Most of the grains are elongated along the transverse direction, but there is also a fraction of smaller grains that tend to grow along the building or scanning direction. Additionally, no strong texture is observed from the inverse pole figures of the cross-sectioned and top-down views in **Figure 53** C) & D).

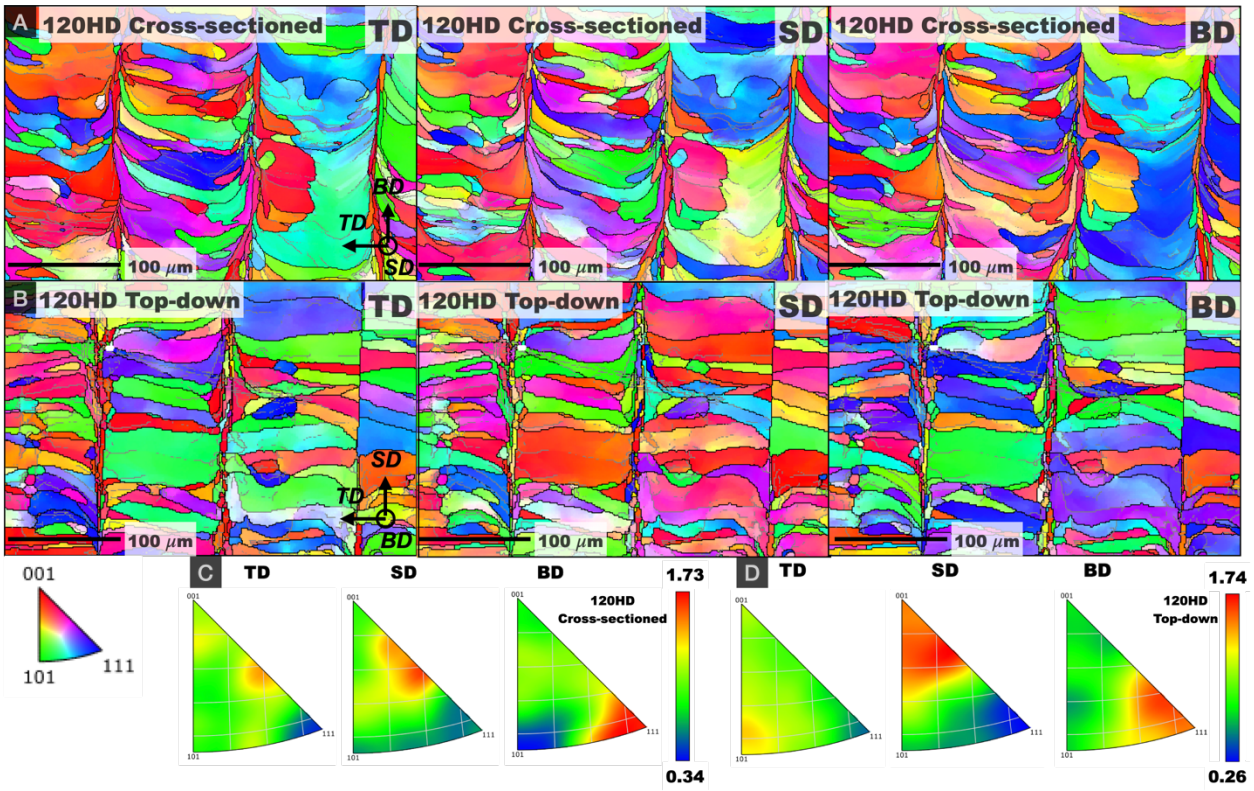

Figure 53*: EBSD orientation and inverse pole figure maps of Ti25Nb-120HD. A) EBSD orientation maps of Ti25Nb-120HD where the "cross-sectioned" surface or scanning direction (SD) faces the EBSD detector. B) EBSD orientation maps of Ti25Nb-120HD where the "topdown" surface or building direction (BD) faces the detector. C) & D) The inverse pole figure sets of A) & B).*

In contrast, the microstructure of Ti25Nb-10HD differs significantly from that of Ti25Nb-120HD, as shown in **Figure 54**. There are no signs of colonies of grains. In the cross-sectioned view in **Figure 54** A), it is possible to distinguish layers of grains due to the layer-by-layer printing process. However, it is not possible to differentiate the effect of each individual vector of laser scan. Two main groups of grains can be observed: the first group, which is larger in volume, has grain orientations of $\{101\}_\beta$ along the scanning direction and either $\{001\}_\beta$ or $\{111\}_\beta$ along the transverse direction and building direction. The second group, which is smaller in volume and narrower in shape, has grain orientations of $\{001\}_\beta$ along all three sample directions. Both groups

of grains grow along the transverse direction with curved grain boundaries. No vertically "walls", like those found in Ti25Nb-120HD, are observed. The top-down view case in **Figure 54** B) show that the grains are thin like curved shells. Additionally, there is a noticeable density of sub-grain boundaries in Ti25Nb-10HD. These sub-grain boundaries are long and meandering. Furthermore, due to the highly grouped grain orientation in Ti25Nb-10HD, it exhibits a strong $\{101\}_\beta$ texture along the scanning direction, as shown in **Figure 54** C) & D). The highest texture index is as high as 4.5 at $\{101\}_\beta$, which is significantly stronger compared to Ti25Nb-120HD.

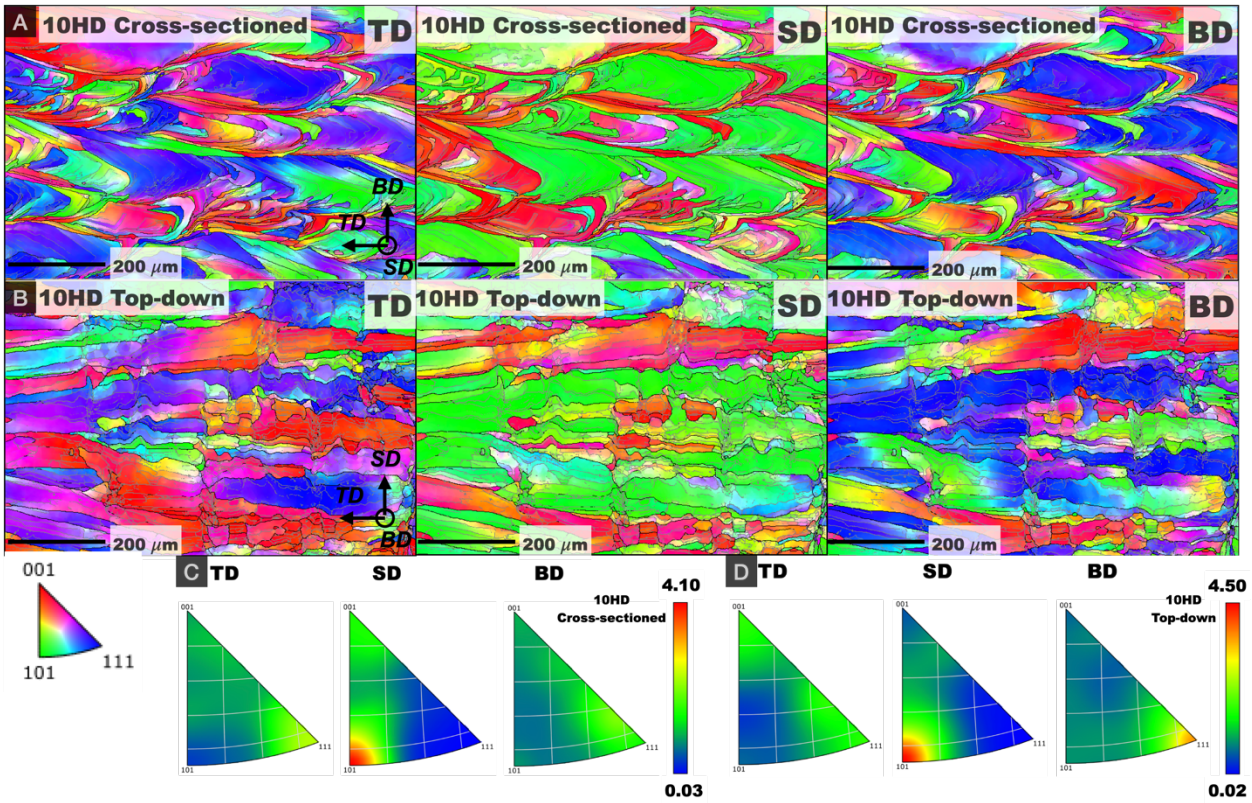

***Figure 54**: EBSD orientation and inverse pole figure maps of Ti25Nb-10HD. A) EBSD orientation maps of Ti25Nb-10HD where the "cross-sectioned" surface or scanning direction (SD) faces the EBSD detector. B) EBSD orientation maps of Ti25Nb-10HD where the "topdown" surface or building direction (BD) faces the detector. C) & D) The inverse pole figure sets of A) & B).*

The effect of hatch distance was further investigated using SEM backscatter electron (BSE) images of Ti25Nb-120HD and Ti25Nb-10HD, as shown in **Figure 55**. The top-down view of Ti25Nb-120HD (**Figure 55**A) reveals colonies of grains like those seen in the EBSD images of **Figure 53**. Additionally, the melt pool boundaries are clearly visible due to their notable Z-contrast. In the zoomed-in view of **Figure 55** B), lines of melt pool boundaries can be seen along the scanning direction. The melt pool center line can be identified with narrower grains that elongate along the scanning direction, as seen in **Figure 53**. Based on images from both **Figure 55** A) and B), the center lines of melt pools are the boundaries of the colonies and that the melt pool boundaries are the center locations of the colonies. In contrast, the Ti25Nb-10HD as shown in **Figure 55** C) & D) show no such colonies of grains. Instead, the melt pool boundaries are distributed throughout the entire frame, which can be clearly visualized in Fig 5D. The average distance between these boundaries is roughly around 10 μm. But there is also significant local variation, which is likely due to limitations in the laser control of the machine and variability in the melt pool geometry during melting. Sub-grains are grown perpendicular to the melt pool boundaries, and roughly along the transverse direction. The sub-grain boundaries are long and meandering, similar to what is observed in **Figure 54**. In short, using extremely small hatch distance can effectively remove the “walls”, and changes the direction of epitaxial solidification from bottom-to-top to side-to-side.

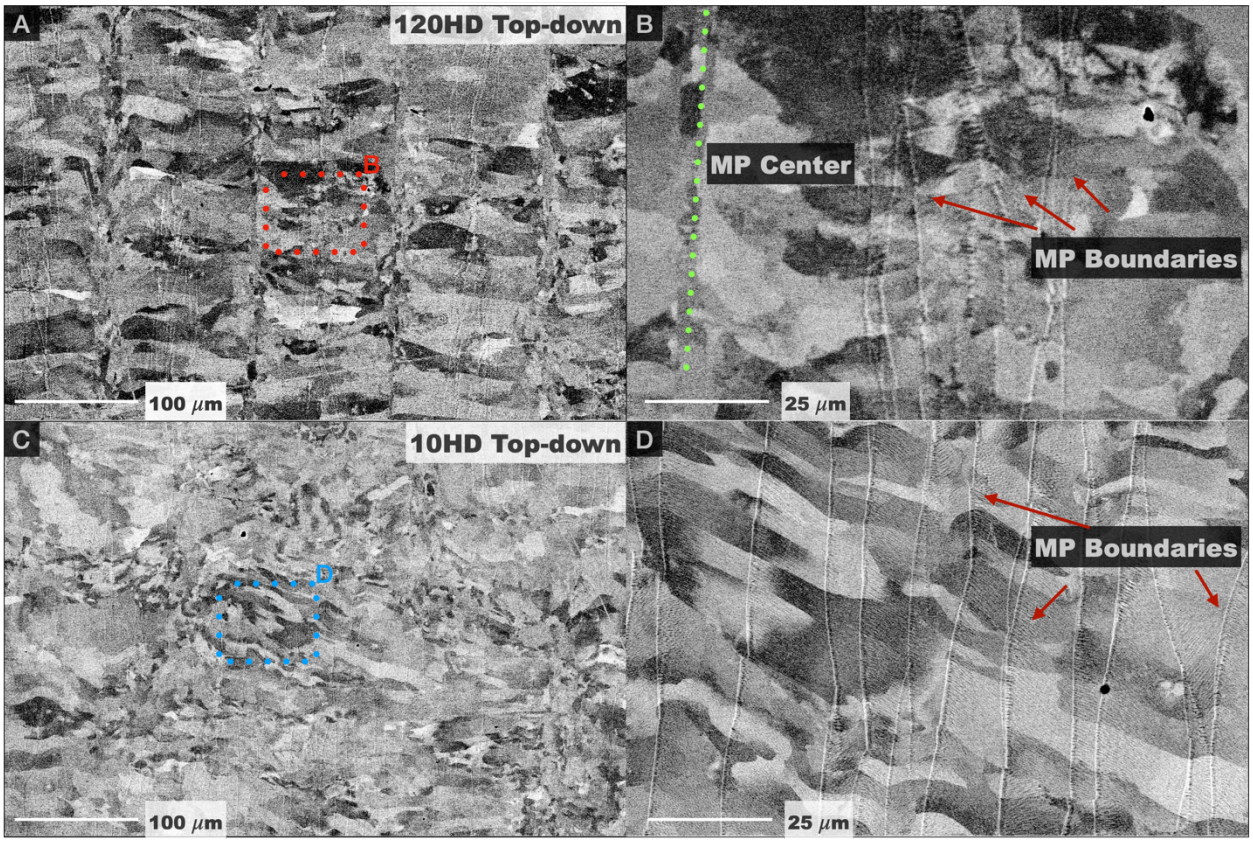

Figure 55*: SEM backscatter electron (BSE) images of Ti25Nb-120HD and Ti25Nb-10HD samples on the top-down view. A) & C) Low magnification view of Ti25Nb-120HD and Ti25Nb-10HD. The box marker in each image indicates the locations where the zoom-in views were captured. B) & D) Zoom-in views of two samples. The green dotted line indicates the location of the center of melt pools of one colony. The red arrows point to the locations of the melt pool boundaries.*

The mechanical performance of additively manufactured Ti25Nb samples are presented in **Figure 56**. The results are also summarized in **Table 5**. The Ti25Nb 67% CR sample has an elastic modulus of 47 GPa, yield strength of 664 MPa, and ultimate tensile strength of 734 MPa. However, it has a low ductility of 6.5% due to severe cold rolling. On the other hand, Ti25Nb-120HD has a higher elongation to failure of 17.0% and modulus of 67 GPa, but about 100MPa lower yield and comparable ultimate tensile strength. Lastly, Ti25Nb-10HD displays a combination of high mechanical properties with an elastic modulus of 32 GPa, even lower than β/metastable β-Ti

alloys used in biomedical applications [8], and comparable yield strength and 10% higher ultimate tensile strength compared to Ti25Nb 67% CR. Nevertheless, its elongation to failure is only slightly lower than Ti25Nb-120HD, around 14%. Compared to cold rolled sample, Ti25Nb-10HD exhibits simultaneous increase in strength and ductility, coupled with a reduction in apparent elastic modulus. This set of properties breaks both the strength-ductility and strength-stiffness tradeoffs typical for engineering materials.

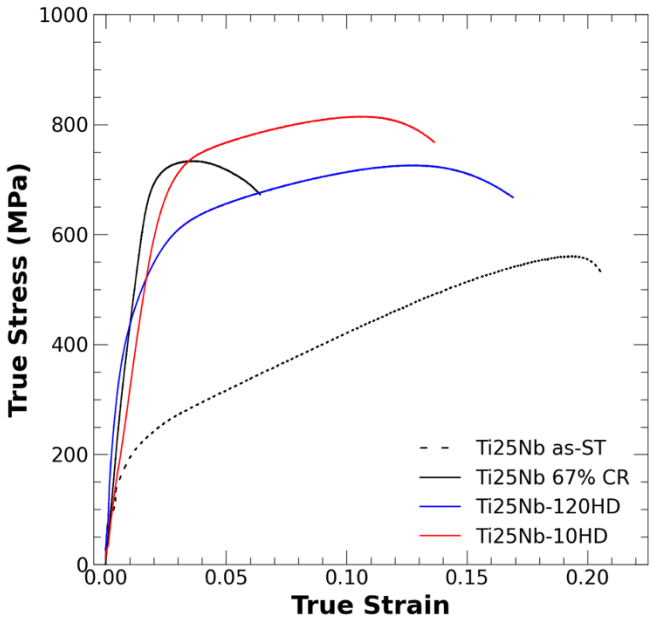

***Figure 56**: Tensile tests of as-printed Ti25Nb samples. Compare as-additive manufactured samples Ti25Nb-120HD and Ti25Nb-10HD with the as-casted Ti25Nb sample after solution-treatment and the one received 67% cold rolling.*

***Table 5**: Summary of tensile tests.*

Sample	Elastic Modulus (GPa)	Yield Strength (MPa)	UTS (MPa)	Elongation to failure (%)
Ti25Nb as-ST	70	218	510	20.1

Ti25Nb 67% CR	47	664	734	6.5
Ti25Nb-120HD	67	532	722	17.0
Ti25Nb-10HD	32	657	813	13.7
Ti25Nb-120HD 300°C 1hr	76	703	896	12.2
Ti25Nb-10HD 300°C 1hr	66	760	840	12.7
Ti25Nb-120HD 600°C 1hr	65	537	788	13.6
Ti25Nb-10HD 600°C 1hr	36	600	717	15.5

4.4. Discussions

The additive manufactured Ti-25Nb (at%) samples exhibit a distinct microstructure and mechanical performance. These outcomes are a combined effect of rapid laser heating/cooling, the choice of printing strategies (e.g., hatch distance), and the inherent metastability of this alloy system. Additionally, the Ti-25Nb (at%) microstructure after AM displayed no α'' phase, concluded from XRD results in **Figure 52**. These changes in microstructure corresponded to mechanical performance improvements, leading to enhanced strength and ductility. This was particularly evident in the Ti25Nb-10HD samples, which also demonstrated a low modulus. We further discuss each of these observations in this section.

4.4.1. The effect of extremely small hatch distance

During the initial stage of rapid solidification after laser melting, solidification near the melt pool boundaries is dominated by epitaxial solidification [3,24]. These grains usually have a high aspect ratio between their length and width, with growth direction from the boundary towards the melt pool centerline following the maximum temperature gradient. At the bottom of the melt pool halfway across its width, the direction of the maximum temperature gradient is approximately vertical in the cross-section. These vertical grains grows as a "wall", and impede epitaxial growth along the transverse direction from each side, shown in **Figure 57** A). If the hatch distance is greater than half of the width of the melt pool, the adjacent laser track does not remelt the centerline "wall", and as a result, the width of the colonies of grains is roughly the same as the width of the melt pools, bounded by melt pool centerlines, which can be seen in **Figure 53**.

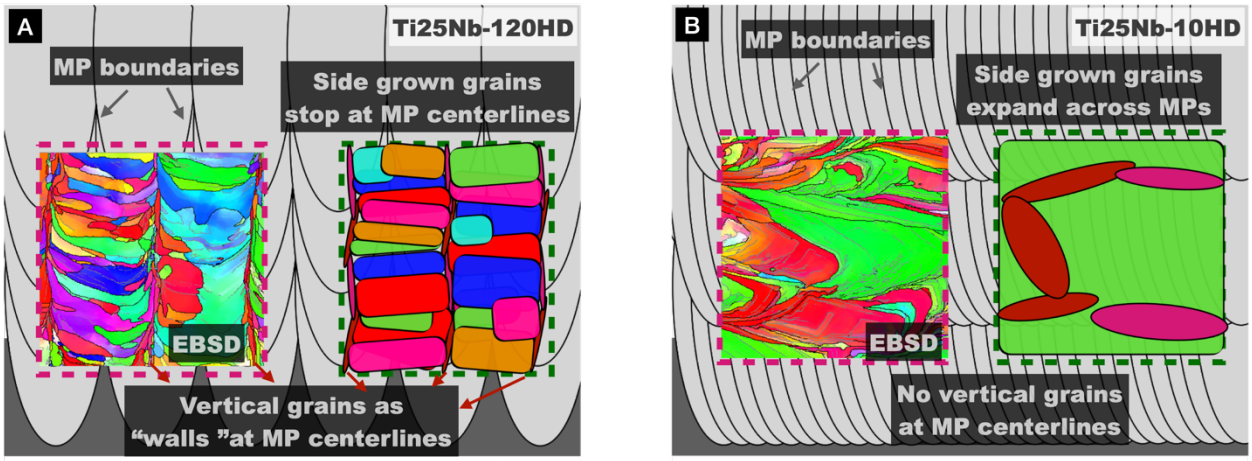

***Figure 57**: Schematical comparison of grain growth in Ti25Nb-120HD and Ti25Nb-10HD with respect to hatch distance of melt pools. EBSD images from **Figure 53** and **Figure 54** are used as references. A) In Ti25Nb-120HD cross-sectioned view, it shows that vertically grown grains form as "walls" at melt pool centerlines. These "walls" block the growth of side grown grains, therefore, forming colonies of grains. B) In the case of Ti25Nb-10HD, there is no such vertically grown grains. Side grown grains can expand across multiple melt pools.*

In contrast, when the hatch distance becomes extremely small, epitaxial growth is more likely to continue. The sequential laser scans erase more than 90% of the previous laser-melted region including the centerline "wall". As a result, the newly formed grains can continue to grow epitaxially from the previous scans along the transverse direction, as shown in **Figure 57** B), forming a side-to-side epitaxy in contrast with the bottom-to-top epitaxy usually observed in AM samples. The dominance of side-to-side epitaxial solidification can be further demonstrated in **Figure 58**. The majority of grains grow perpendicularly to the melt pool boundaries, and this trend extends beyond individual melt pool boundaries. In **Figure 58** B) and D), it is shown that cellular boundaries, which appear as dark lines in BSE images, tend to grow and follow perpendicularly to the curvature of the melt pool boundaries.

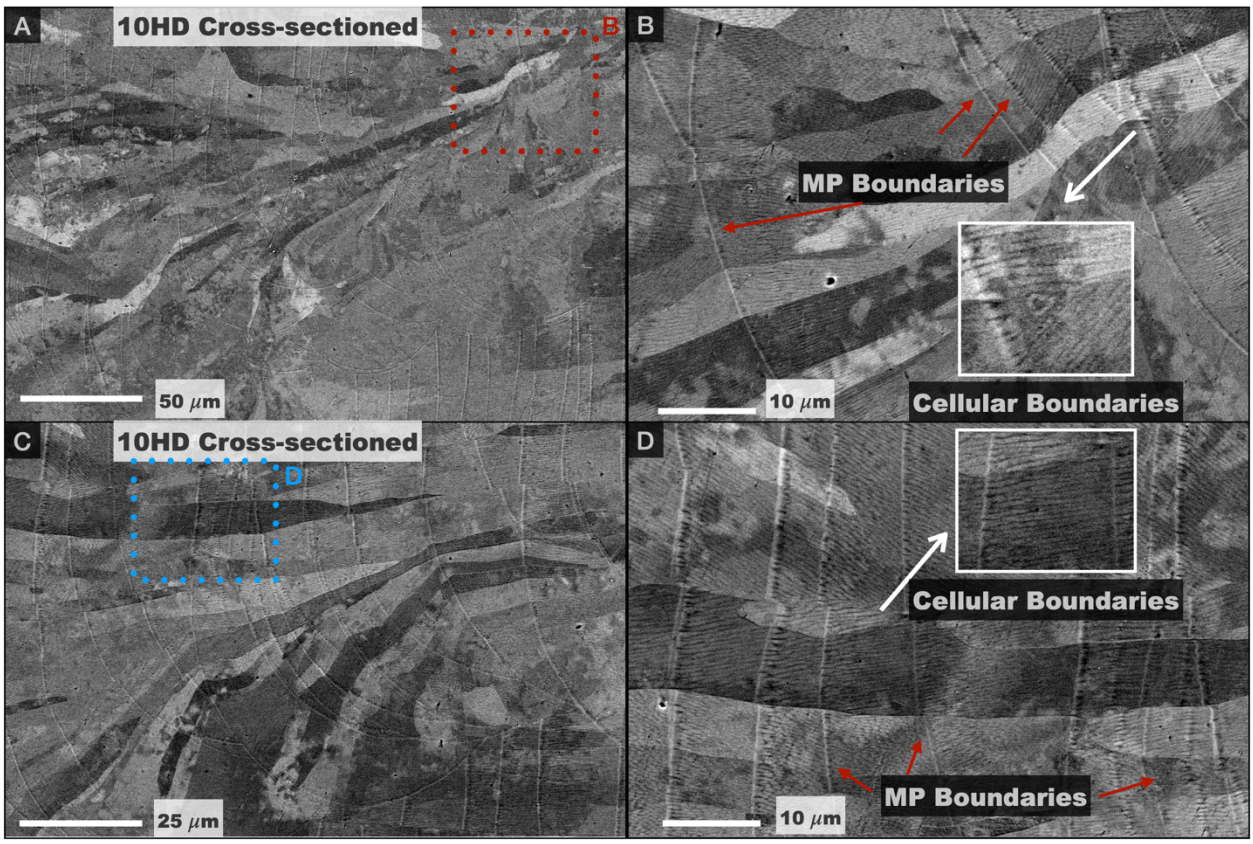

***Figure 58**: SEM BSE images of Ti25Nb-10HD on the cross-sectioned view. A) & C) Low magnification view of Ti25Nb-10HD. The box marker in each image indicates the locations where the zoom-in view was captured. B) & D) Zoom-in view of the bottom/middle of the melt pools. The red arrows point to the locations of the melt pool boundaries. Cellular boundaries, which are Ti-rich, display dark lines in the BSE images.*

However, from the actual EBSD images in **Figure 54**, it is also clear that the side-to-side epitaxy does not continue indefinitely. One scenario is that grains that form near the bottom of melt pools can grow at an angle which can out-complete the grains that grow along the transverse direction. Despite the small hatch distance, each additional laser melting scan, however, does not completely erase the bottom grains. Also, the shape and position of each melt pool can be slightly off from the designated values, causing the bottom grains to continuously grow "diagonally"

towards the next melt pool centerline, as shown in **Figure 54** A). This is further demonstrated in the BSE image in **Figure 58** A), where these grains can grow along multiple melt pools and eventually breaks the development of grains that grow along the transverse direction, as shown in **Figure 58** C). Therefore, the grain structure is a combination of grains that grow sideways, grains that grow at various diagonals, and others that are nucleated with random orientation.

Nevertheless, it seems that such enforced epitaxial growth can prompt specific grain orientations. Based on the results in **Figure 54**, it is shown that there is a strong $\{101\}_\beta$ texture along the scanning direction. Specifically, there are two main groups of grain orientations. The first group has a $\{101\}_\beta$ orientation along the scanning direction, while the second group has $\{001\}_\beta$ orientation along all three main directions. Clearly, employing an extremely small hatch distance erases the centerline orientations dominate which prompt side-to-side epitaxial growth. This unconventional approach also allows the scanning direction becomes the dominant direction in the case of Ti25Nb-10HD instead of the building direction in many other cases reported in the literature [2,19,25]. Besides, it is unusual to have a strong $\{101\}_\beta$ texture instead of a $\{001\}_\beta$ texture in a cubic system in additive manufacturing. Yet, the actual mechanism that enhance in-plane orientation development in AM is still unknown.

4.4.2. Metastable phases

XRD results show that as-printed Ti25Nb samples have a metastable phase, displaying noticeable shoulder peaks next to β peaks. This phase is not the expected α'' orthorhombic phase in metastable β-Ti alloys. Instead, the d-spacings of its crystalline planes are very close to the parental BCC phase with less than 1% deviation, as can be seen in **Figure 52** D). From the TEM diffraction patterns in **Figure 59**, diffraction patterns of Ti25Nb-10HD are not differentiable from

those in the BCC phase. However, the lattice is slightly distorted, as evidenced by the fact that the d-spacings of $(0\bar{1}1)_\beta$, $(1\bar{1}0)_\beta$ and $(\overline{10}1)_\beta$ are slightly different, showing in **Figure 59** B). Similar difference can be seen on the d-spacing of $(\bar{1}\bar{2}1)_\beta$ and $(\bar{2}\bar{1}1)_\beta$ in **Figure 59** C). These measurements match the XRD results. In our previous study [20], we concluded that such distortion is due to the formation of O' phase in these samples. Similar diffraction patterns can be found in studies of β-Ti alloys with additional introduction of oxygen interstitial or under heavy deformation [26,27]. There are multiple possible oxygen sources during the printing process, like the remaining oxygen gas in the chamber and the oxide on the surfaces of Ti25Nb (at%) particles. Since oxygen atoms tend to occupy the octahedral interstitial sites of BCC lattice, this results in slight lattice distortion [27,28]. With additional deformation, several superlattice diffraction spots can appear in the diffractions, halfway between main diffraction spots, as a result of losing symmetry. Such superlattice spots can be observed in **Figure 59** A) & C). According to Tahara et al, such short-distance lattice modulation of O' phase can effectively become barriers for long-distance martensitic phase transformation from β to α'' [29]. Therefore, it maybe the reasons why α'' martensite phase is not apparent in both Ti25Nb-120HD and Ti25Nb-10HD samples.

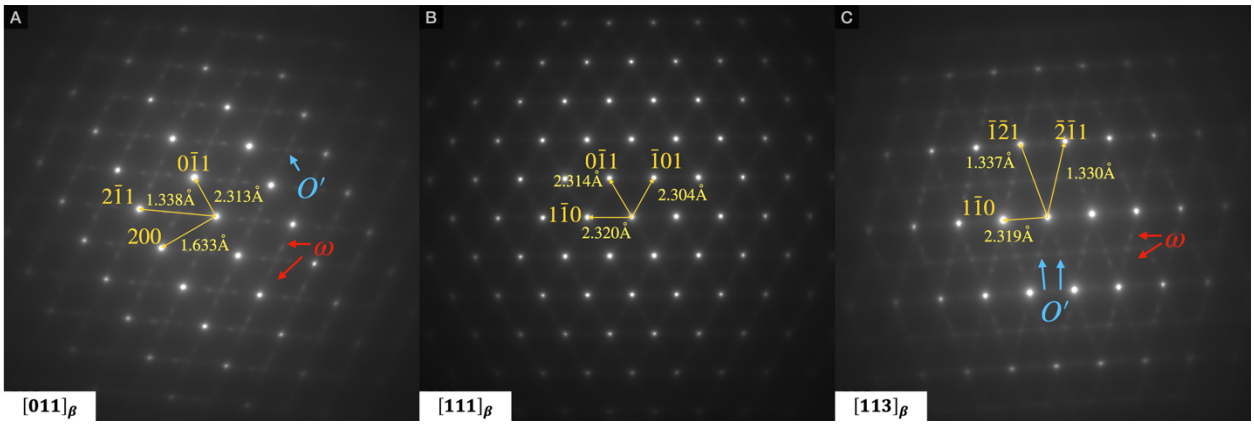

***Figure 59**: TEM diffraction patterns of Ti25Nb-10HD at various of zone axes. The patterns are indexed as the ones of BCC phase. The measured d-spacings of major planes are marked in each pattern. Diffraction spots of two metastable phases ω and O' are also identified.*

4.4.3. Mechanical properties of additive manufactured Ti-25Nb (at%)

4.4.3.1. Strengthening

Based on the summary of the tensile tests in **Table 5**, Ti25Nb-120HD has more than twice higher yield strength and 50% higher UTS compared to Ti25Nb as-ST. Similar observations of strength improvements can be also found in other AM metals in the literature as well [2]. However, in metals such as 316L stainless steel fabricated using AM, the major contribution to strength increase is believed to be from the novel dislocation network. The smaller grain size and additional boundary effect resulting from solidification features can also increase the resistance to dislocation propagation. In addition, the existence of metastable phases such ω and O', which are detected shown in **Figure 59**, should also contribute to the higher strength. Then, Ti25Nb-10HD, exhibits an even higher strength, about more than 10% UTS increase compared to Ti25Nb-120HD and Ti25Nb 67% CR which already has a greater extent of grain size refinement. This strength increase is somewhat unexpected. According to the EBSD results in **Figure 53** and **Figure 54**, the average grain size of Ti25Nb-10HD is noticeably larger than Ti25Nb-120HD. Also, based on the XRD

results in **Figure 52**, no perceptible of difference in phase compositions between Ti25Nb-120HD and Ti25Nb-10HD. Then the question is what contribute to the increase of strength in Ti25Nb-10HD. First, Ti25Nb-10HD has significantly more sub-grain boundaries than Ti25Nb-120HD which can be both saw in EBSD images in **Figure 54** and BSE images in **Figure 55**. Those boundaries are densely populated across the scanning direction. Second, Ti25Nb-10HD also has more than 10 times of the melt pool boundaries density than Ti25Nb-120HD due to the small hatch distance. According to Kong et al., those solidification boundaries in AM metals such as 316L SS can be treated as weaker boundaries that can interfere the movement of dislocations [21]. As it can be seen, the melt pool boundaries are densely populated across the transverse direction. The hypothesis is that substantially more sub-grain boundaries as well as the melt pool boundaries prevent the movement of dislocation, therefore, increase the strength. One additional note is that no dislocation network similar to the ones found in AM 316L stainless steel samples is observed in AM Ti25Nb [20].

4.4.3.2. Elongation to failure

As **Figure 60** A) shown, AM Ti25Nb samples exhibit larger elongation to failure compared to cold-rolled Ti25Nb (at%) samples. For example, Ti25Nb-120HD exhibits an elongation to failure of 17%, which is nearly three times the value of the Ti25Nb 67% CR. This is comparable to Ti25Nb as-ST, which has a 20.1% elongation to failure. Given that Ti25Nb-120HD has only slightly lower yield strength but almost equal UTS compared to Ti25Nb 67% CR, it is reasonable to assert that AM Ti25Nb samples overcome the strength-ductility trade-off often observed in conventional metallurgy. Similar improvements can be found in other AM metals such as 316L stainless steel [30]. The common belief is that the dislocation network in AM 316L stainless steel,

embedded along the cellular boundaries, contributes to the increase in elongation to failure [30,31]. However, such a dislocation network is not observed in either Ti25Nb-120HD and Ti25Nb-10HD using TEM. This suggests that a different mechanism is responsible for the increase in elongation to failure, at least in the Ti-Nb system. One hypothesis is that the microstructure in AM Ti25Nb can suppress the formation of local shear bands. Nevertheless, further studies are required to confirm this hypothesis.

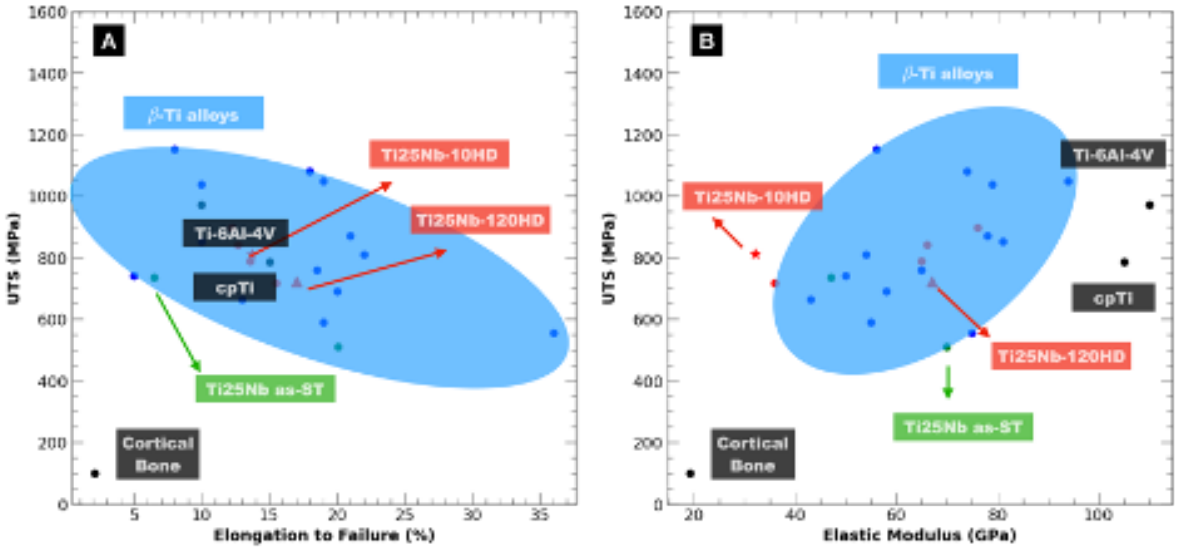

Figure 60*: Ashby charts of the current work, compared with selected biomedical structural materials in the literature. A) Ultimate tensile strength (UTS) vs. elongation to failure; B) UTS vs. elastic modulus [3,5,30,31].*

4.4.3.3. Elastic modulus

One of the main findings of this study is that Ti25Nb-10HD exhibits an ultra-low elastic modulus of 32 GPa. The likely origins of this ultra-low elastic modulus include rolling texture, dense melt pool boundaries, and the O' metastable phase. Tensile tests (**Table 5**) demonstrate that the cold-rolled Ti25Nb 67% CR sample has a lower elastic modulus of 50 GPa, compared to the typical 70 GPa of Ti25Nb as-ST. Note that $\{101\}_{\beta}$ texture is typically the rolling texture in BCC

[32]. Since Ti25Nb-10HD also possesses a similar rolling texture to Ti25Nb 67% CR along the scanning direction, it might be reasonable to assume that Ti25Nb-10HD can experience a similar modulus reduction effect. However, this factor alone is insufficient to explain the ultra-low modulus observed in Ti25Nb-10HD.

Another possibility is that Ti25Nb-10HD may undergo stress-induced phase transformation. If the stress-induced phase transformation occurs during the elastic deformation region, the apparent modulus can display a significantly lower value. For instance, the Ni-Ti shape memory alloy can exhibit an apparent modulus of 10 GPa due to the triggering of transformation from B2 to B19 [28]. Normally, Ti-25Nb exhibit stress-induced phase transformation from β to α''. However, based on the previous discussion, the formation of O' phase because of oxygen interstitials suppresses such a capability. Yet, having O' phase cannot explain why Ti25Nb-10HD has such a low modulus. Based on the XRD results, Ti25Nb-120HD contains O' phase as well. The modulus of Ti25Nb-120HD, however, is close to values of typical Ti alloys, around 70 GPa [10]. Additionally, the presence of another metastable ω phase, which is a brittle phase, should also increase the overall modulus. Therefore, one of the hypotheses is that Ti25Nb-10HD can initiate a stress-induced phase transformation from β phase to O' phase, during the elastic deformation, while Ti25Nb-120HD cannot. The dense laser scans in Ti25Nb-10HD created a microstructure with very dense melt pool boundaries. Since melt pool boundaries have a similar effect as grain boundaries, despite the weaker impact [21]. These boundaries may divide samples into numerous micro-sized “zones”. These “zones” prevent long-distance lattice shearing or modulation across multiple “zones” but may stimulate lattice motion within a “zone”. Plus, the placement of oxygen interstitial atoms may be affected by the highly directional thermal strain from laser melting. As a result, the short-distance lattice modulation from β phase to O' phase can

be initiated due to low activation energy. This further leads to a lower apparent elastic modulus in the elastic deformation. On the other hand, Ti25Nb-120HD has much separated melt pool boundaries. Therefore, more activation energy is required to start such phase transformation, resulting in an unfavorable event.

4.4.4. Effect of heat treatment

Since metastable β-Ti alloys are sensitive to thermo-mechanical treatments, it is important to investigate the effects of heat treatment on as-printed AM Ti25Nb. Two heat treatment conditions have been selected: the first involves furnace heat treatment at 600°C for 1 hour, followed by water quenching, while the second employs a furnace heat treatment of 300°C for 1 hour instead. The primary aim of the first procedure is to facilitate dislocation recovery and dissolve the ω phase [33], whereas the latter is intended to form thermal ω, which is expected to yield a higher strength, lower ductility. Due to either low temperature or short duration, neither is expected to trigger recrystallization or significant alterations to cellular solidification features and grains.

Based on the results of **Figure 52** and **Figure 61** A), the phase composition for both Ti25Nb-120HD and Ti25Nb-10HD remain relatively unchanged after heat treatment at 600°C for 1 hour. It is unusual to have O' phase remaining after a 600℃ heat treatment for 1 hour. Typically, such heat treatment should eliminate metastable phases and promote the formation of β phase and then partially converts to α'' phase for this composition. Interestingly, both Ti25Nb-120HD and Ti25Nb-10HD after heat treatment further stabilized O' phase and suppressed the formation of α'' phase. This leads us to believe that the as-printed microstructure somehow favors this O' phase over α''phase. However, the stress-strain curve does show that Ti25Nb-120HD undergoes stress-

induced martensitic phase transformation from β to α''. Yet, the tensile response of Ti25Nb-10HD after heat treatment is pretty much identical to the as-printed condition. It implies that Ti25Nb-10HD can effectively retain its as-printed microstructure. On the other hand, a 300℃ heat treatment for 1 hour increases the strength of the as-printed materials by over 100MPa, shown in **Figure 61** B). This is due to the precipitation of the brittle ω phase. Surprisingly, the elongation to failure for Ti25Nb-120HD after heat treatment at 300℃ for 1 hour reduces about 25%, but the impact on Ti25Nb-10HD is fairly minor. This further confirms that the as-printed microstructure of Ti25Nb-10HD has better thermal stability. In the meanwhile, the elastic modulus of Ti25Nb-10HD increases significantly, which suggests that ω precipitates suppress the mechanism for obtaining ultralow modulus.

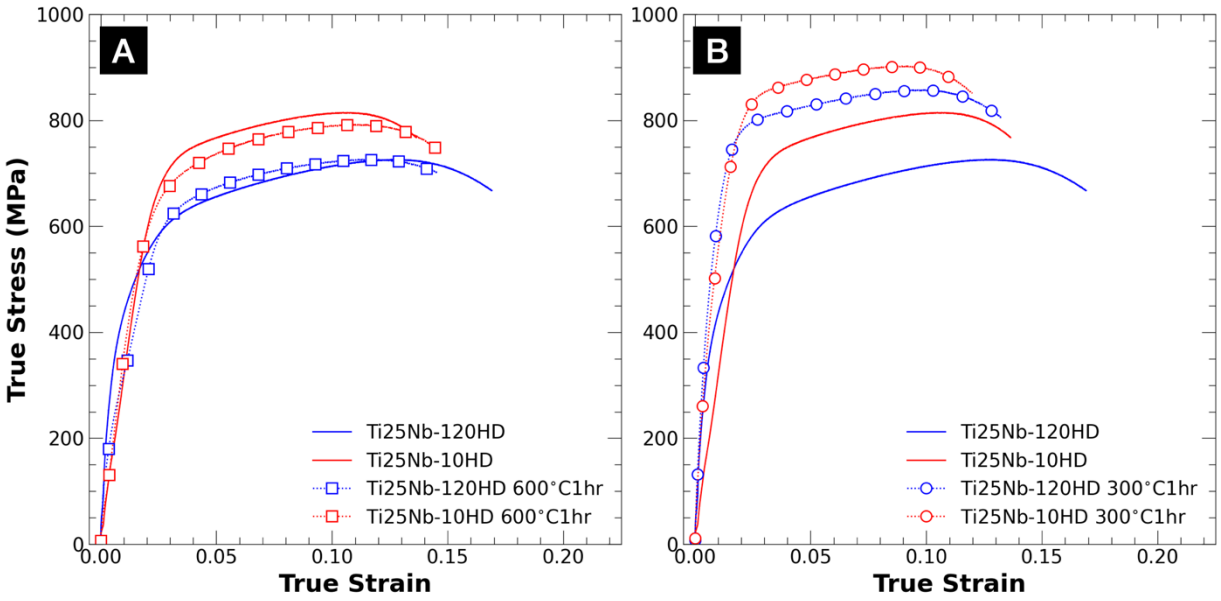

***Figure 61**: Tensile tests of various additive manufactured Ti25Nb under post heat treatments. A) Compare as-additive manufactured conditions with ones after 600°C furnace heat treatment for 1 hour. B) Compare as-additive manufactured conditions with ones after 300°C furnace heat treatment for 1 hour.*

4.5. Conclusions

In this study, we fabricated Ti-25Nb (at%) samples, Ti25Nb-120HD and Ti25Nb-10HD, using a laser powder bed fusion system with two distinct settings of hatch distance (120 μm vs. 10 μm). After evaluating their microstructure and tensile performance, here comes the following conclusions:

- A printing strategy employing an extremely small hatch distance (10 μm) can lead to Ti25Nb samples exhibiting ultralow modulus while retaining high strength and good elongation to failure.
- Ti25Nb-10HD exhibits drastically different microstructure compared to the those built with a normal hatch distance (120 μm). The in-plane epitaxy is enhanced, breaking the dependency along building direction (BD). These samples also display a strong $\{101\}_{\beta}$ texture along the scanning direction (SD), which also happens to be the rolling texture of BCC metals.
- As-printed Ti-25Nb (at%) samples have no α'' martensite phase but obtain O' phase. This implies the AM microstructure in Ti-25Nb (at%) tend to suppress long distance martensitic phase transformation but simulate short-distanced lattice modulation.

4.6. References

[1] N. Li, S. Huang, G. Zhang, R. Qin, W. Liu, H. Xiong, G. Shi, J. Blackburn, Progress in additive manufacturing on new materials: A review, J. Mater. Sci. Technol. 35 (2019) 242–269. https://doi.org/10.1016/j.jmst.2018.09.002.

[2] T. DebRoy, H.L. Wei, J.S. Zuback, T. Mukherjee, J.W. Elmer, J.O. Milewski, A.M. Beese, A. Wilson-Heid, A. De, W. Zhang, Additive manufacturing of metallic components – Process, structure and properties, Prog. Mater. Sci. 92 (2018) 112–224. https://doi.org/10.1016/j.pmatsci.2017.10.001.

[3] J.P. Oliveira, T.G. Santos, R.M. Miranda, Revisiting fundamental welding concepts to improve additive manufacturing: From theory to practice, Prog. Mater. Sci. 107 (2020) 100590. https://doi.org/10.1016/j.pmatsci.2019.100590.

[4] Z. Zhu, W. Li, Q.B. Nguyen, X. An, W. Lu, Z. Li, F.L. Ng, S.M. Ling Nai, J. Wei, Enhanced strength–ductility synergy and transformation-induced plasticity of the selective laser melting fabricated 304L stainless steel, Addit. Manuf. 35 (2020) 101300. https://doi.org/10.1016/j.addma.2020.101300.

[5] Y. Li, K. Chen, R.L. Narayan, U. Ramamurty, Y. Wang, J. Long, N. Tamura, X. Zhou, Multi-scale microstructural investigation of a laser 3D printed Ni-based superalloy, Addit. Manuf. 34 (2020) 101220. https://doi.org/10.1016/j.addma.2020.101220.

[6] P. Deng, H. Yin, M. Song, D. Li, Y. Zheng, B.C. Prorok, X. Lou, On the Thermal Stability of Dislocation Cellular Structures in Additively Manufactured Austenitic Stainless Steels: Roles of Heavy Element Segregation and Stacking Fault Energy, JOM. 72 (2020) 4232–4243. https://doi.org/10.1007/s11837-020-04427-7.

[7] X. Wang, S. Xu, S. Zhou, W. Xu, M. Leary, P. Choong, M. Qian, M. Brandt, Y.M. Xie, Topological design and additive manufacturing of porous metals for bone scaffolds and orthopaedic implants: A review, Elsevier Ltd, 2016. https://doi.org/10.1016/j.biomaterials.2016.01.012.

[8] M. Long, H.J. Rack, Titanium alloys in total joint replacement--A materials science perspective., Biomaterials. 19 (1998) 1621–39. https://doi.org/10.1016/S0142-9612(97)00146-4.

[9] R. Kolli, A. Devaraj, A Review of Metastable Beta Titanium Alloys, Metals (Basel). 8 (2018) 506. https://doi.org/10.3390/met8070506.

[10] L.-C. Zhang, L.-Y. Chen, A Review on Biomedical Titanium Alloys: Recent Progress and Prospect, Adv. Eng. Mater. 21 (2019) 1801215. https://doi.org/10.1002/ADEM.201801215.

[11] X. Wang, Y. Li, J. Xiong, P.D. Hodgson, C. Wen, Porous TiNbZr alloy scaffolds for biomedical applications, Acta Biomater. 5 (2009) 3616–3624. https://doi.org/10.1016/J.ACTBIO.2009.06.002.

[12] K. Alvarez, H. Nakajima, Metallic Scaffolds for Bone Regeneration, Materials (Basel). 2 (2009) 790–832. https://doi.org/10.3390/ma2030790.

[13] R.R. Dehoff, M. Kirka, W.J. Sames, H. Bilheux, A.S. Tremsin, L.E. Lowe, S.S. Babu, Site specific control of crystallographic grain orientation through electron beam additive manufacturing, Mater. Sci. Technol. (United Kingdom). 31 (2015) 931–938. https://doi.org/10.1179/1743284714Y.0000000734.

[14] H.L. Wei, T. Mukherjee, W. Zhang, J.S. Zuback, G.L. Knapp, A. De, T. DebRoy, Mechanistic models for additive manufacturing of metallic components, Prog. Mater. Sci. 116 (2021). https://doi.org/10.1016/j.pmatsci.2020.100703.

[15] B. Attard, S. Cruchley, C. Beetz, M. Megahed, Y.L. Chiu, M.M. Attallah, Microstructural control during laser powder fusion to create graded microstructure Ni-superalloy components, Addit. Manuf. 36 (2020). https://doi.org/10.1016/j.addma.2020.101432.

[16] N. Nadammal, S. Cabeza, T. Mishurova, T. Thiede, A. Kromm, C. Seyfert, L. Farahbod, C. Haberland, J.A. Schneider, P.D. Portella, G. Bruno, Effect of hatch length on the development of microstructure, texture and residual stresses in selective laser melted superalloy Inconel 718, Mater. Des. 134 (2017). https://doi.org/10.1016/j.matdes.2017.08.049.

[17] A. Plotkowski, J. Ferguson, B. Stump, W. Halsey, V. Paquit, C. Joslin, S.S. Babu, A. Marquez Rossy, M.M. Kirka, R.R. Dehoff, A stochastic scan strategy for grain structure control in complex geometries using electron beam powder bed fusion, Addit. Manuf. 46 (2021). https://doi.org/10.1016/j.addma.2021.102092.

[18] Y. Kok, X.P. Tan, P. Wang, M.L.S. Nai, N.H. Loh, E. Liu, S.B. Tor, Anisotropy and heterogeneity of microstructure and mechanical properties in metal additive manufacturing: A critical review, Mater. Des. 139 (2018) 565–586. https://doi.org/10.1016/j.matdes.2017.11.021.

[19] K.A. Sofinowski, S. Raman, X. Wang, B. Gaskey, M. Seita, Layer-wise engineering of grain orientation (LEGO) in laser powder bed fusion of stainless steel 316L, Addit. Manuf. 38 (2021). https://doi.org/10.1016/j.addma.2020.101809.

[20] W. Lin, H. Heinrich, J. Ma, Unusual strain relaxation mechanism in metastable β Ti-Nb alloy after rapid solidification, Scr. Mater. 211 (2022) 114499. https://doi.org/https://doi.org/10.1016/j.scriptamat.2022.114499.

[21] D. Kong, C. Dong, S. Wei, X. Ni, L. Zhang, R. Li, L. Wang, C. Man, X. Li, About metastable cellular structure in additively manufactured austenitic stainless steels, Addit. Manuf. 38 (2021) 101804. https://doi.org/10.1016/j.addma.2020.101804.

[22] M. Newville, T. Stensitzki, D.B. Allen, A. Ingargiola, LMFIT: Non-Linear Least-Square Minimization and Curve-Fitting for Python, (2014). https://doi.org/10.5281/ZENODO.11813.

[23] K. Hagihara, T. Nakano, Control of Anisotropic Crystallographic Texture in Powder Bed Fusion Additive Manufacturing of Metals and Ceramics—A Review, JOM. 74 (2022) 1760–1773. https://doi.org/10.1007/s11837-021-04966-7.

[24] B. Fotovvati, S.F. Wayne, G. Lewis, E. Asadi, A Review on Melt-Pool Characteristics in Laser Welding of Metals, Adv. Mater. Sci. Eng. 2018 (2018). https://doi.org/10.1155/2018/4920718.

[25] P. Fernandez-Zelaia, M.M. Kirka, S.N. Dryepondt, M.N. Gussev, Crystallographic texture control in electron beam additive manufacturing via conductive manipulation, Mater. Des. 195 (2020) 109010. https://doi.org/https://doi.org/10.1016/j.matdes.2020.109010.

[26] M. Tahara, H.Y. Kim, T. Inamura, H. Hosoda, S. Miyazaki, Role of interstitial atoms in the microstructure and non-linear elastic deformation behavior of Ti-Nb alloy, J. Alloys Compd. 577 (2013) S404–S407. https://doi.org/10.1016/j.jallcom.2011.12.113.

[27] J.M. Oh, J.H. Kang, S. Lee, S.D. Kim, N. Kang, C.H. Park, Origin of superproperties of Ti-23Nb-1Ta-2Hf-O alloy, Mater. Lett. 233 (2018) 162–165. https://doi.org/10.1016/j.matlet.2018.08.151.

[28] S. Miyazaki, My Experience with Ti–Ni-Based and Ti-Based Shape Memory Alloys, Shape Mem. Superelasticity. 3 (2017) 279–314. https://doi.org/10.1007/s40830-017-0122-3.

[29] M. Tahara, T. Kanaya, H.Y. Kim, T. Inamura, H. Hosoda, S. Miyazaki, Heating-induced martensitic transformation and time-dependent shape memory behavior of Ti–Nb–O alloy, Acta Mater. 80 (2014) 317–326. https://doi.org/https://doi.org/10.1016/j.actamat.2014.07.012.

[30] L. Liu, Q. Ding, Y. Zhong, J. Zou, J. Wu, Y.L. Chiu, J. Li, Z. Zhang, Q. Yu, Z. Shen, Dislocation network in additive manufactured steel breaks strength–ductility trade-off, Mater. Today. 21 (2018) 354–361. https://doi.org/10.1016/j.mattod.2017.11.004.

[31] Y.M. Wang, T. Voisin, J.T. McKeown, J. Ye, N.P. Calta, Z. Li, Z. Zeng, Y. Zhang, W. Chen, T.T. Roehling, R.T. Ott, M.K. Santala, P.J. Depond, M.J. Matthews, A. V. Hamza, T. Zhu, Additively manufactured hierarchical stainless steels with high strength and ductility, Nat. Mater. 17 (2018) 63–70. https://doi.org/10.1038/NMAT5021.

[32] A. Gupta, R. Khatirkar, J. Singh, A review of microstructure and texture evolution during plastic deformation and heat treatment of β-Ti alloys, J. Alloys Compd. 899 (2022) 163242. https://doi.org/https://doi.org/10.1016/j.jallcom.2021.163242.

[33] H.Y.Y. Kim, Y. Ikehara, J.I.I. Kim, H. Hosoda, S. Miyazaki, Martensitic transformation, shape memory effect and superelasticity of Ti–Nb binary alloys, Acta Mater. 54 (2006) 2419–2429. https://doi.org/10.1016/j.actamat.2006.01.019.

[34] V. Amigó-Borrás, J. Lario-Femenía, A. Amigó-Mata, Á. Vicente-Escuder, Titanium, Titanium Alloys and Composites, in: F.G.B.T.-E. of M.M. and A. Caballero (Ed.), Elsevier, Oxford, 2022: pp. 179–199. https://doi.org/https://doi.org/10.1016/B978-0-12-819726-4.00044-2.

[35] S. Bahl, S. Suwas, K. Chatterjee, Comprehensive review on alloy design, processing, and performance of β Titanium alloys as biomedical materials, Https://Doi.Org/10.1080/09506608.2020.1735829. 66 (2020) 114–139. https://doi.org/10.1080/09506608.2020.1735829.

5. Conclusions & Recommendations for Future Work

Achieving an ultralow modulus while maintaining high strength in metallurgy is a challenging task. This dissertation presents reliable methods using both conventional metallurgical approach (Chapter 2) and modern additive manufacturing (AM) approach (Chapters 3 & 4). Both methods successfully fabricated Ti-25Nb (at%) materials with elastic moduli around 30 GPa or below while maintaining strengths above 700-800 MPa. Notably, the current research pioneers the study of AM metastable β Ti alloys, offering valuable insights into both microstructure and printing strategies for these alloys. The findings from this dissertation could potentially encourage the development and adaptation of metastable β Ti alloys for orthopedic implant applications, as well as inspire innovative ideas for using AM to control microstructure and tailor material properties of metastable β Ti alloys or their metallic systems.

5.1. Key conclusions

- Ultralow modulus in Ti-25Nb (at%) can be achieved via implementing cold rolling, followed by short-during, low temperature aging and water quench. Samples were examined using in-situ synchrotron loading experiments which unequivocally demonstrate the role of stress-induced α'' martensitic phase transformation in lowering the apparent elastic modulus of Ti-Nb.
- Similar ultralow modulus in Ti-25Nb (at%) can be obtained via LPBF, with the implementation of an extremely small hatch distance. AM Ti-25Nb samples also exhibit high strength and good elongation to failure, breaking the conventional strength-ductility tradeoffs.
- Laser-processed Ti-25Nb (at%) exhibits a significantly different microstructure compared to conventionally processed materials. Regions that experience multiple

remelting/reheating passes have different microstructures compared to ones that have only been melted once. An unknown orthorhombic phase is observed in the Nb-lean regions. Also, it is found that the long-distance martensitic phase transformation from β to α'' is suppressed yet the short-distance lattice modulation is simulated, favoring the formation of O' phase and certain O' variants.

- The implementation of an extremely small hatch distance in LPBF can effectively enhance in-plane epitaxial grain growth. Grains in these AM Ti-25Nb (at%) samples tend to continuously grow along the transverse direction (TD) across multiple melt pools without being halted at centerlines of melt pools. These samples also display a strong $\{101\}_{\beta}$ texture along the scanning direction (SD), which also happens to be the rolling texture of BCC metals.
- It suggests that there are multiple feasible microstructures in Ti-25Nb (at%) that can reduce the initial apparent elastic modulus. Chapter 2 demonstrates that a small amount of ω is essential for reducing the initial stress of SIMT, as well as the apparent elastic modulus. However, Chapter 4 demonstrates that certain AM microstructures without ω can still achieve similar modulus reduction. The actual required microstructural components for achieving a low modulus remain unclear.

5.2. Recommendations for future work

- The remaining question from this dissertation is to confirm whether the modulus reduction phenomenon originates from SIMT, for samples fabricated conventionally or via AM. The key confirmation is to verify that the formation of the martensite phase can begin at low external stress in those ultralow modulus samples. It is still recommended to conduct in-

situ mechanical tests either under synchrotron X-ray diffraction or TEM electron diffraction.

- Similarly, the role of omega in the modulus reduction phenomenon requires further investigation. A good starting point is to initiate S/TEM analysis on the Ti-Nb samples before and after short-duration low-temperature aging. Understanding the essential microstructural components after aging that trigger modulus reduction is crucial. If resources permit, an in-situ heating/cooling diffraction experiment inside the S/TEM is also recommended.
- More in-depth S/TEM work on laser-processed Ti-Nb samples is also recommended. Several critical pieces of information are still missing. For instance, the identity of the unknown orthorhombic phase remains unclear. Careful SAED or CBED experiments are required to reveal the actual lattice structure. Additionally, the AM defects, such as dislocation networks, are not discernible in the current TEM studies. Extra effort is needed to confirm the situation and further investigate the actual mechanism for ductility improvement.
- In the last chapter, an extremely small hatch distance is applied. The major downside is the significant increase in building time. However, it may be possible to speed up the build by further increasing the layer thickness from 100 μm to 200 μm or more. This could potentially enhance the epitaxial growth along the transverse direction as well.